A Study of Iron Based Alloys by Positron Annihilation Spectroscopy

Khaled Mohamed Mostafa

Promotoren: prof. dr. ir. Y. Houbaert, prof. dr. D. Segers
Proefschrift ingediend tot het behalen van de graad van
Doctor in de Ingenieurswetenschappen: Materiaalkunde

Vakgroep Toegepaste Materiaalwetenschappen
Voorzitter: prof. dr. ir. J. Degrieck
Faculteit Ingenieurswetenschappen
Academiejaar 2008 - 2009

ISBN 978-90-8578-286-5
NUR 926, 971
Wettelijk depot: D/2009/10.500/44

Toelating tot bruikleen

Gent, Mei 2009

Khaled M Mostafa	prof.dr.ir. Y. Houbaert	Prof.dr. D. Segers
Auteur	Promotor	Promotor

Acknowledgements

My path to doctorate in materials science has been neither easy nor straightforward, but underway I have met many interesting people and gained a lot of scientific and life experience. Those years would have been much more difficult without the assistance of those who gave their support in different ways.

Without Professor Houbaert, I could not be able to continue my research. First, he guided me more to the field of metallurgy. Thanks for the technical discussions, for your help to finish my thesis in a timely matter. I have learned from you how to keep our promises. Professor D. Segers, who accepted me to start the PhD in his group, his warm welcoming, and his support with his wide experience in the field of positrons. Dr. J. De Bardmaaker, I want to say, you are such a wonderful person I am proud to know. Thanks for your support, all the experience that you gave to me and guiding me everywhere. Thanks of being the closest friend. I wish you and your wonderful family always the best.

I'd like to thank Professor Charles Dauwe for his help and the valuable discussions. Many thanks to prof Robert Vandenberghe and Prof Eddy de Grave for giving me the opportunity to do such work in the Mossbauer Lab., and for their unlimited help.

Thanks to all the professors and the stuff of the materials science department. prof.dr. Jurgen Schneider, Prof.dr. Prof.dr. Jan Penning for being taking care of everybody. Thanks to prof dr.ir. Leo Kestens dr.ir. Roumen dr.ir. Petrov and dr.ir. Kim Verbeken. I have to thank dr.ir. Pablo Calvillo for the nice work we did together and I am proud of your friendship and dr.ir.Lucia Fernandez.

Other people I want to thank are: my other committee members, Voorzitter: Prof. Daniël De Zutter, Prof. Christophe Leys, Prof. Jan Van Humbeeck for the very interesting questions, dr. Steven Van Peteghem for his deep technical discussion and dr.ir. Kim Verbeken for guiding me and for his very important remarks.

Carlos Palacio, thanks for your support and of being always close to me most of the time. I wish you success with your kind wife (Alexandra) in your future life. Special thanks to N. Laforest who is really a good friend before being a colleague. Special thanks to Bartel Van Waeyenberge, Abdurazak M. Alakrmi, and Valdirene De Resende for being always around. I would like to express my gratitude to all my other colleagues of the NUMAT: Dr Toon Van Alboom, Arne Vansteenkiste, and Caroline Van Cromphaut. Thanks to all the members stuff of the department of subatomic and radiation physics. Thanks to all my colleagues in Department of Materials science and engineering (Gent University). I am especially grateful to Nele Van Caenegem for the work cooperation and her support.

I would like to thank the team of the administrative and technical staff in Department of Subatomic and Radiation Physics: Philippe Van Auwegem (you are the best), Roland De Smet, Patrick Sennesael, George Wiewauters, Christophe Schuerens, Bart Vancauteren, Daniella Lootens, Linda Schepens, Brigitte Verschelden and Rudi Verspille (thanks a lot for your kind help). Many thanks to the administrative and technical staff in Department of materials Science and Engineering: Ilse Vercruysse, Roger Van Hecke, Peter Mast, Marnix Van Dorpe, Dennis van den Oudenhoven, Sarah Steenbeke, Christiana Sonck, Michel Moors, Alex De Groote, Aline De Bondt, and Jordy Van Vlierberghe.

Thanks to all my close friends in Belgium from the different countries.

Thanks to my extended family for their sincere encouragement, especially to my parents who I wish to see them as soon as possible. Huge thanks is to my wife Fatma for being incredibly understanding, supportive, and most of all, patient.

Khaled

Summary

Plastic deformation of metals and alloys produces different changes in the density and distribution of lattice defects inside the materials. Many techniques can be used to study the deformation processes and their effects in iron based alloys. The positron annihilation technique is well known to be a highly sensitive method for open volume defects (such as vacancies, vacancy clusters, dislocations,..). The defect structure after plastic deformation of metallic samples can be investigated with the positron annihilation technique. The high sensitivity of positrons to defects stems from two facts: their attraction to atomic-size defects and their long diffusion length, which is about a few hundred nanometres in most materials. The positron annihilation lifetime spectroscopy (PALS) can quantify the type of the open volume defect as well as the defect concentration and is based on the precise measurement of the lifetime of a positron in a solid. The concentration can be deduced from the fraction of positrons that annihilates in a trapped state. The defect size is directly related to the value of the positron lifetime: the larger the defect, the lower the local electron density and consequently the longer the positron lifetime will be.

The general aim of the present research is to show that the use of the non-destructive Positron Annihilation Spectroscopy (PAS) technique, together with X-ray diffraction (XRD), optical microscopy (OM) and some additional techniques is meaningful for the investigation of the different kinds of defects formed during the cold and warm deformation of metals and alloys in general and in iron-based materials in particular.

In deformed metals, positrons are captured by dislocations and vacancies. In polycrystalline samples, the deformation becomes more complex due to the various interactions between dislocations and grain boundaries. Furthermore, the interaction of dislocations during the deformation can lead to the formation of jogs and point defects.

In the present work, three iron-based materials have been studied: first, iron is studied by PAS as a base material. The results for the positron mean lifetime

after isochronal annealing reveal that the traps for positrons in the deformed iron are mainly dislocations. Less pure iron is much more resistant to recrystallization. The interstitial elements in a very low concentration have a profound effect on recovery processes. In particular, interstitial elements are associated with retardation of recovery

The second iron-based material to be studied is FeMnSiCrNi, a shape memory alloy. The FeMnSiCrNi(C) alloys have a one way shape memory effect. For this reason, the phase transformation, the effect of the degree of plastic deformation and the isochronal annealing of these alloys was investigated. During deformation, the austenite transforms to stress-induced ε–martensite. During heating above a critical temperature the reverse transformation $\varepsilon \rightarrow \gamma$ occurs and the material recovers its original shape. Samples deformed from 2 to 20% (tensile deformation) were investigated. The positron annihilation parameters show a sudden increase in the defect concentration between 4 and 6% deformation. For deformations higher than 10 percent the concentration of defects seems to saturate.

The variations of the nature and the concentration of defects are studied as a function of the isochronal annealing temperature. Using the positron annihilation techniques, the effect of isochronal annealing on the deformation-induced defects and phase transition in FeMnSiCrNiC is studied. A set of deformed FeMnSiCrNiC samples (2- 20% tensile deformation) were annealed isochronally (15 minutes) starting from room temperature up to 500°C in steps of 100°C. The 2% deformed sample has almost no ε-phase after annealing at 500°C. In the case of the 20% deformed sample, the value of the S parameter is higher than the one for the defect-free sample. This means that the 20% deformed samples still have defects after annealing at 500°C. The XRD and the OM show that deformation of 2% and 20% result in the stress-induced transformation of austenite to ε martensite. The ε martensite appears as thin parallel lines with dark contrast inside the austenite grains. Increasing stress induces the appearance of large ε domains. At the same time, zones of thin parallel ε plates containing α' martensite appear. During annealing at high temperatures, the reverse ε-

martensite to austenite phase transformation occurs. The 2% deformed sample has almost no ε phase after annealing at 500°C. If the deformation is small (less than 4%), the reverse movement of the Shockley partials is not impeded because only primary ε variants move through the parent austenite under the influence of stress. The microstructure of the 20% deformed samples still contains ε martensite.

The influence of the addition of carbon to the FeMnSiCrNi base material was studied at room temperature by different techniques. The concentration of dislocations in both deformed samples (FeMnSiCrNi and FeMnSiCrNiC) is calculated. The concentration values for both samples indicate that the alloy without carbon has more dislocations than the one with carbon.

The third iron-based material to be studied is FeSi electrical steel. Alloying iron with silicon improves its magnetic performance by reducing the effect of magnetostriction, noise and energy losses, while the electrical resistivity increases. These properties are also influenced by the grain size and crystallographic texture. Despite of the magnetic improvement of electrical steels their workability is extremely reduced by solid solution hardening and by the appearance of ordered structures.

Several problems arise from increasing the silicon content up to 6.5 wt.%. For this reason it is too hard to do a cold deformation for high silicon steel. Steels with high amounts of silicon are used in electrical applications. The different kinds of defects formed when the FeSi samples are deformed at high temperature (1000°C) and room temperature are investigated in this work. A comparison of the defect concentration for the samples deformed at high temperature and the ones deformed at room temperature is also one of the subjects to be investigated.

The data of the positron annihilation techniques show that the deformation temperature affects the concentration and the type of defects formed in the alloys through the deformation process. Mono-vacancies are the main defects formed when the alloys are deformed at high temperatures. In the case of the alloys deformed at room temperature, dislocations and vacancy clusters are formed. For

the high temperature deformed samples, the positron annihilation lifetime in defects (τ_2) and the S parameter decrease with increasing Si-content in the alloy. For the samples deformed at room temperature, there is a saturation trapping for positrons in defects. There are two lifetime components present: the first one is around 150 ps, which is related to the positron annihilation in dislocations, the second component is around 250 ps. This lifetime value is an indicator for the existence of vacancy clusters.

In general we have tried to classify the different kinds of defects in different iron based alloys and to have data for the positron annihilation parameters.

Samenvatting

Plastische vervorming van metalen en legeringen veroorzaakt veranderingen in de dichtheid en de distributie van roosterstoringen of -defecten in het inwendige van het materiaal. Voor het bestuderen van de onderliggende processen tijdens het vervormen van op ijzer gebaseerde legeringen worden verschillende technieken aangewend. Het is bekend dat de positronannihilatietechniek een zeer gevoelige methode is om open volume defecten (zoals vacatures, vacature-clusters, dislocaties,...) te bestuderen. Daarom kan de defectstructuur, bekomen na plastische vervorming, bestudeerd worden met deze positronannihilatietechniek. De hoge gevoeligheid van het positron voor het detecteren van open volume defecten is te wijten aan twee feiten: de aantrekking van het positron door defecten op atomaire schaal en de grote diffusielengte van het positron, die een paar honderd nanometer bedraagt in de gebruikelijke metalen. Met positronannihilatie-levensduurmetingen (PALS) kan zowel de grootte als de concentratie van de open volume defecten bepaald worden. Deze methode is gebaseerd op de precieze meting van de positronlevensduur in een vaste stof. De bepaling van de concentratie van defecten kan afgeleid worden uit de fractie van positronen die annihileren in de elektronenwolk van een defect. De positronlevensduur is evenredig met de grootte van het defect: hoe groter het defect, hoe kleiner de elektronenconcentratie in het defect, met als gevolg dat de positronlevensduur langer wordt.

De algemene doelstelling van voorliggend onderzoekswerk is de inzet van een niet-destructieve positronannihilatietechniek (PAS), samen met X-stralen diffractie (XRD), optische microscopie (OM) en enkele complementaire technieken voor de studie van de verschillende soorten defecten die door plastische vervorming in metalen en legeringen gevormd worden.

In plastisch vervormde, monokristallijne metalen worden positronen voornamelijk ingevangen door dislocaties en vacatures. In vervormde polykristallijne materialen wordt het deformatieproces ingewikkelder ten gevolge van verschillende interacties tussen dislocaties en korrelgrenzen. Ook de

interactie tussen dislocaties tijdens het vervormingsproces kan leiden tot de vorming van jogs en puntdefecten (vacatures en interstitiële atomen).

In een eerste fase van het onderzoek wordt het basismateriaal zuiver ijzer bestudeerd met PAS. Uitgaande van metingen van de positron gemiddelde levensduur tijdens isochrone gloeiproeven kan aangetoond worden dat de invangcentra voor positronen in vervormd zuiver ijzer hoofdzakelijk dislocaties zijn. De evolutie van de concentratie aan roosterfouten tijdens de gloeiproeven (herstel en ev. rekristallisatie) kan met PAS gevolgd worden. Bij minder zuiver ijzer verlopen de rekristallisatie-fenomenen na plastische vervorming trager: interstitiële onzuiverheden, die in lage concentratie aanwezig zijn, hebben een grote invloed op het herstelgedrag. In het bijzonder verklaart de aanwezigheid van interstitiële onzuiverheden de vertraging van het herstelfenomeen bij verhoogde temperaturen.

De vormgeheugenlegering FeMnSiCrNi is het belangrijkste materiaal dat in dit onderzoek bestudeerd wordt. Deze legeringen vertonen een één-weg vormgeheugen effect (one-way shape memory effect). De optredende fasentransformaties en het effect van de vervormingsgraad werden bij deze legeringen bestudeerd tijdens isochroon gloeien. Tijdens de plastische vervorming transformeert austeniet in spanningsgeïnduceerde ε-martensiet. Wanneer deze legering terug opgewarmd wordt tot boven een kritische temperatuur treedt de inverse transformatie $\varepsilon \rightarrow \gamma$ op en neemt het materiaal zijn oorspronkelijke vorm terug op. De onderzochte monsters hadden een plastische verlenging ondergaan tussen 2 en 20%. Tussen 4 en 6% vervorming tonen de metingen van de positronparameters een plotse toename van de defecten-concentratie. Bij vervormingen boven de 10% lijkt er een verzadiging van de defecten-concentratie op te treden.

Ook de verandering van het type defect en de evolutie van de concentratie aan verschillende defecten werd in functie van de gloeitemperatuur bestudeerd. Het effect van het isochrone gloeien op de door vervorming geïnduceerde defecten en op de transformaties in FeMnSiCrNiC werd bestudeerd door gebruik te

maken van de positronannihilatietechniek. Daartoe werden vervormde FeMnSiCrNiC monsters (2 - 20% verlenging) isochroon gegloeid (15 minuten) op temperaturen van kamertemperatuur tot 500°C in stappen van 100°C. Het monster dat vervormd werd tot 2% bevat, na gloeien bij 500°C, vrijwel geen ε-fase meer. Voor het monster dat vervormd werd tot 20% is na gloeien op 500°C de S-parameter hoger dan deze gemeten in het defectvrije (referentie-)monster. Dit betekent dat er in het 20% vervormde monster, na gloeien bij 500°C, nog steeds defecten aanwezig zijn. XRD en OM waarnemingen tonen aan dat vervormingen van 2% en 20% een spanningsgeïnduceerde transformatie van austeniet naar ε-martensiet induceren. De ε-martensiet wordt waargenomen als dunne parallelle lijnen met een donker contrast binnen de austenietkorrels. Wanneer de spanning toeneemt ontstaan er grotere ε-domeinen. Tegelijkertijd ontstaan er zones waar dunne parallelle ε-platen aanwezig zijn, die ook α'-martensiet bevatten. Bij gloeien op verhoogde temperatuur doet zich de inverse transformatie van ε-martensiet naar austeniet voor. In het 2% vervormde monster is er na gloeien op 500°C vrijwel geen ε-fase meer aanwezig. Voor vervormingen kleiner dan 4% wordt de beweging van Shockley partiële dislocaties niet gehinderd omdat er enkel primaire ε-varianten doorheen de austeniet bewegen onder invloed van de spanning. In de microstructuur van het 20% vervormde monster is er nog steeds ε-martensiet aanwezig.

Er werden proeven uitgevoerd om de invloed van koolstoftoevoegingen aan het FeMnSiCrNi basismateriaal te bestuderen. Deze experimenten werden met verschillende meettechnieken op kamertemperatuur uitgevoerd. De dislocatieconcentratie werd berekend in de legeringen FeMnSiCrNi en FeMnSiCrNiC. Uit de berekeningen volgt dat er in de legering zonder koolstof meer dislocaties aanwezig zijn dan in de legering met koolstof.
Een derde materiaal op ijzerbasis dat eveneens bestudeerd werd is elektrisch staal (FeSi-staal) met Si-toevoegingen die tot 6,5 m.-% kunnen oplopen. Het toevoegen van Si aan Fe zorgt ervoor dat de magnetische eigenschappen van het materiaal beter worden: reductie van de magnetostrictie en de ruis en een vermindering van het energieverlies bij gebruik, via een verhoging van de elektrische resistiviteit. De magnetische eigenschappen worden ook beïnvloed

door de korrelgrootte en door de kristallografische textuur. Alhoewel de magnetische eigenschappen van elektrisch staal verbeterd zijn, vertoont het materiaal tegelijkertijd een groot nadeel door een drastische vermindering van de plastische vervormbaarheid, bvb. bij het walsen tot dunne plaat.

Talrijke problemen ontstaan wanneer het silicium gehalte stijgt tot 6,5 m.-% (waarde voor minimale magnetostrictie). Staal met een hoog Si-gehalte is te hard om nog een koudvervorming te kunnen ondergaan, hun bewerkbaarheid is sterk gereduceerd. In voorliggend onderzoek worden de defecten bestudeerd in FeSi-monsters die warm- (1000°C) en koudvervormd (kamertemperatuur) werden. Eén van de centrale doelstellingen van het werk is het vergelijken van de defectconcentratie in de monsters die vervormd werden bij hoge temperatuur en bij kamertemperatuur.

Resultaten van de positronannihilatieproeven tonen aan dat de temperatuur waarbij de monsters vervormd worden bepalend is voor zowel de concentratie als het type defect dat in de legeringen door de plastische vervorming geïnduceerd wordt. Mono-vacaturen zijn de defecten die in hoofdzaak aanwezig zijn wanneer de legering bij hoge temperatuur vervormd wordt. Wanneer de legering echter bij kamertemperatuur vervormd wordt, dan worden dislocaties en vacatureclusters gevormd. Voor de legeringen die vervormd worden bij hoge temperatuur stijgt zowel de positron levensduur (τ_2) als de S-parameter wanneer het siliciumgehalte in de legering toeneemt. Voor de legeringen vervormd bij kamertemperatuur treedt er saturatie-invang op. Er zijn twee levensduurcomponenten aanwezig: de eerste heeft een waarde rond 150 ps en wordt toegeschreven aan positronen die annihileren uit een ingevangen toestand in dislocaties, de tweede component heeft een waarde rond 250 ps en suggereert de aanwezigheid van vacatureclusters.
Als algemeen besluit kan gesteld worden dat er aangetoond werd dat het mogelijk is op basis van PAS verschillende types defecten te herkennen en te classificeren die in verschillende op ijzer gebaseerde legeringen optreden en specifieke waarden te bekomen voor de verschillende positronparameters die deze roosterfouten typeren.

List of abbreviations and symbols

Abbreviations

ACAR	angular correlation of annihilation radiation
at.%	atomic percent
bcc	body centered cubic
bct	body centered tetragonal
CR	cold rolling
DBAR	Doppler broadening
EBSD	electron backscatter diffraction
fcc	face centered cubic
FWHM	full with at halve maximum
HCP	hexagonal close packed
HPGe	Hyper pure Germanium
HR	hot rolling
IQ	image quality
ND	normal direction
OM	optical microscopy
PALS	positron annihilation lifetime spectroscopy
PAS	positron annihilation spectroscopy
RT	room temperature
S,W	annihilation lineshape parameters
SEM	scanning electron microscopy
SMAs	shape memory alloys
SME	shape memory effect
TEM	Transmission electron microscopy
TD	transverse direction
VEPFIT	variable energy positron FIT
ULC	ultra-low carbon
wt.%	weight percent
WQ	water quench
XRD	X-ray diffraction

Roman symbols

A_s	Austenite start temperature
A_f	Austenite finish temperature
c	speed of light
D_+	positron diffusion coefficient
e^+	positron
e^-	electron
L_+	positron diffusion length
M_d	highest temperature at which martensite can be formed
M_s	martensite start temperature
M_f	martensite finish temperature
P_s	positronium
T_N	Néel Temperature

Greek Symbols

α	ferrite
α'	α' martensite
ε	ε martensite
γ	austenite
κ	positron trapping rate
λ	annihilation rate
ρ	density
τ	positron annihilation lifetime

Table of contents

Chapter 1
Introduction

1.1 General introduction

The material research is of the utmost importance, since the design and construction of new products often requires materials of high quality. This means that there is a demand for detailed knowledge of, e.g., the atomic structure, the crystal lattice defects, the concentration of defects, and interface effects of the used materials. Therefore, analysis techniques that yield qualitative or quantitative information are not only desirable, but also necessary.

Positron physics is concerned with the interaction of positrons with matter. From the discovery of the positron seventy five years ago, positron physics has developed into an important technique for providing unique information on a wide variety of problems in condensed-matter physics. Positron annihilation lifetime spectroscopy (PALS), Doppler broadening of annihilation radiation (DBAR) and the slow positron beam were the main positron techniques used. DBAR measurements were done in-situ with a tensile machine. The positron techniques are used to identify the kind of defects and also to calculate the concentration of defects (vacancies or dislocations). The phase transitions can also be identified. The optical microscopy (OM) and the X ray diffraction (XRD) are used to see the phase transition and correlate their results with the ones of the positron techniques.

1.2 Iron based alloys

Different kinds of iron based alloys are developed according to what properties or applications they are intended for. In the present work of this thesis, the FeMnSiCrNi(C) shape memory alloys have been studied. Iron as the base

material has also been investigated. The effect of the deformation of FeSi at high and low temperature has been studied.

1.2.1 FeMnSiCrNi(C) Shape memory alloys (SMAs)

Shape memory alloys (SMAs) are one of these kinds of materials, which are characterized by a shape memory effect and which may show effects of super-elasticity, which ordinary metals and alloys do not have. SMAs are materials that have the ability to return to some or all previously defined shape or size when subjected to the appropriate thermo-mechanical procedure [1]. More than 20 alloys have been reported to show substantial shape memory effects. Only NiTi based alloys have been used for major technological applications [2]. The NiTi alloys have an excellent shape memory behavior and are corrosion resistant but the cost of these alloys is very high. Copper based shape memory alloys also have some minor applications. These alloys are less expensive but their low corrosion resistance reduces the number of applications [3].

It has been found that Fe-based alloys such as FePt, FePd, FeNi, FeAlC and FeMnSi could exhibit a shape memory effect (SME) but under certain conditions. The determining factors influencing the transformation are the extent of pre-strain, the deformation temperature, the degree of thermo-mechanical training and the annealing temperature. Some of these Fe-based SMAs are expensive such as FePt and FePd, so that, they are only used in the academic research. Other materials have incomplete SME. The very low M_s of FeNiCoTi (below 200 K) is the main disadvantage for this alloy being widely used.

Ferrous shape memory alloys based on the FeMn alloy system have received much attention since the eighties of the last century and there are definite signals from the shape memory materials research community that they may become a new class of one-way SMAs of great technical importance due to their cost-effectiveness [4, 5]. The shape memory effect in FeMnSi alloys was first reported by Sato et al. [6]. They found that a single crystal of a Fe-30wt.%Mn-1wt.%Si alloy exhibited a complete shape memory effect when deformed in the

<414> direction. Sato et al. [7] succeeded in developing polycrystalline FeMnSi shape memory alloys. Murakami et al. [8] developed the polycrystalline FeMnSi shape memory alloys and reported the nearly complete shape recovery for alloys with a composition of 28% Mn and 6 wt.% Si. Moriya et al. [9] and Otsuka et al. [4] developed FeCrNiMnSi and FeCrNiMnSiCo shape memory alloys, which show excellent corrosion resistance. Tsuzaki et al. [10] have found that adding 0.3 wt.% carbon to the Fe–17%Mn–6%Si alloy improves the SME of this alloy. Thermo-mechanical treatments are necessary to obtain a good shape memory effect [11, 12]. The best thermo-mechanical treatment consists of a recrystallization, a deformation at room temperature and a final annealing.

One-way shape memory alloys have been used in various applications. Joining pipes is one of the most important applications of the FeMnSi based SMAs (see Figure 1.1) [13]. The alloys are also used for heavy duty joint components for railway constructions [13- 15].

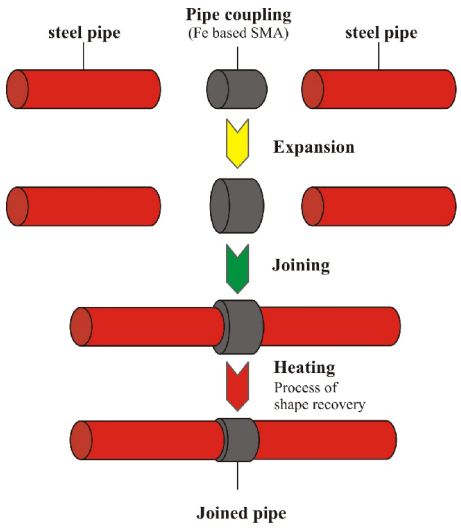

Figure 1.1 A schematic drawing of pipe joints (two pipes and a shape memory alloy [13])

1.2.2 FeSi Electrical Steel

The importance of FeSi alloys in electrical industry arises from their excellent electrical and magnetic properties, which are optimal when the Si content reaches 6.5 wt.%. At this concentration the electrical resistance is increased, the eddy current loss is reduced and the magnetostriction is almost zero. This concurrence of properties makes Si steel the most suitable material for the construction of electrical devices like transformers and motors. However, by increasing the Si concentration, the alloy becomes very brittle and therefore difficult to be cold rolled into the required thin sheets. This embrittlement is mainly due to ordering phenomena [16]. Surface diffusion techniques for the enrichment on Si and/or Al have shown its beneficial effect on magnetic properties like power losses and magnetostriction.

Among these techniques hot dipping in a hypereutectic AlSi bath is a promising alternative under development at Ghent University (Belgium). This procedure modifies the alloy composition through the deposition of a Si–Al rich layer on top of a substrate with a lower Si-content and a subsequent diffusion annealing of Si and Al in the steel matrix until the desired content is obtained [17].

1.3 Positron annihilation spectroscopy (PAS)

The positron is the antiparticle of the electron. This was first predicted by Dirac in 1930 [18]. In the special relativity theory, the relationship between the energy E and the linear momentum p of the free particle with rest mass m is

$$E^2 = p^2 c^2 + m^2 c^4 \qquad (1.1)$$

where, c is the velocity of light. The solution of this equation is $E = \pm c\sqrt{p^2 + m^2c^2}$. His theory contained a solution with a negative energy in addition to the positive energy solution that corresponds to the electron. Dirac then argued that, if there was a negative energy state, the electron with positive energy could decay into the negative energy state with the emission of $\boldsymbol{2mc^2}$

radiation. He concluded that an electron with negative energy moves in an external field as thought it carries a positive charge. He had predicted the annihilation of an electron-positron pair. However, the only positively charged particle known at that time was a proton, and he assumed that the particle was a proton, even though the difference in the mass of an electron and a proton was puzzling.

The first experimental discovery of a positron came in 1932 when Anderson was measuring traces of cosmic rays in cloud chambers [19, 20]. Positron was thus the first antiparticle in physics. Anderson believed the pair production theory of Dirac only when he saw the positron and electron tracks, which are always present in his cloud chamber. This new particle penetrated a 6 mm lead plate and made a path much longer than that expected for a proton (see Figure 1.2). Anderson concluded that the particle should to be less massive than a proton and most likely has the mass of an electron. He called this new particle "the positive electron" or "positron". In 1936 Anderson was honoured with the Nobel Prize for his discovery of positrons.

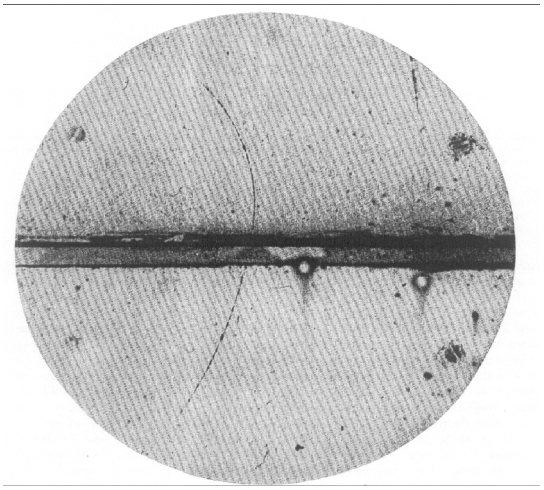

Figure 1.2 A 63 million volt positron passing through a 6mm lead plate and emerging as 23 million volt positron (Anderson [19])

In 1934 Thibaud [21] observed the annihilation of positrons with electrons. The bound state of a positron and electron was predicted classically by Mohorovicic [22] and quantum mechanically by Ruark [23] in 1945. In 1949 DuMond [24] discovered that the 511 keV annihilation gamma-ray line was broadened and could attribute this to the momentum of the annihilating electron. This was the birth of the development of the Doppler Broadening of annihilation Radiation (DBAR) spectroscopy. In 1950 Deutsh discovered the positronium atom [25].

In 1952 Bell and Graham performed positron lifetime measurements in liquids and solids [26]. They were the first to use a timed beam set-up for fast positrons. During the 1960's electronics improved to the point where PALS was able to probe positron lifetimes in metals (typically a few hundred picoseconds). By the end of the 1960's it was realized that the positron annihilation parameters are sensitive to the lattice imperfections. Positrons can be trapped in crystal defects which, means that the wave function of a positron is localized at the defect site until annihilation. The sensitivity of positron annihilation spectroscopy (PAS) to the defects in deformed materials was first realized by Dekhtyar et al. 1964 [27], Berko and Erskine 1967 [28], and MacKenzie et al. 1967(29). The first observation of trapping of positrons in dislocations in metals and alloys was by Dekhtyar et al. [27]. Berko and Erskine [28] studied the angular correlation of deformed and annealed Al and concluded that the positron would be localized on the dilatational side of a (edge) dislocation. MacKenzie [29] showed this behavior for thermal vacancies in metals. Arponen et al. [30] assumed that the positron lifetime observed in deformed metal is due to dislocation line. Doyama and Cotterill [31] listed the lifetimes for annihilation in the bulk and dislocations for a number of metals. They measured the positron annihilation at dislocation loops in Al to be 250 ± 30 ps. This value is in agreement with the value of the deformed Al measured by Hautojarvi *et* al in 1970 [32], which is 229 ps.

The positron annihilation technique has been applied to the study of various phase transitions in condensed matter (Fukushima and Doyama 1979) [33]. Some measurements of positron annihilation have been made for martensitic transformations in metals and alloys (Troev et al., 1977 [34], Tanigawa et al.

1976 [35] and Hauytojarvi et al. 1979 [36]). Dislocations produced during the transformation must be considered when martensitic transformation is studied by positron annihilation [33, 36]. D. Segers, J. Van Humbeeck and I. Hurtado studied different types of shape memory alloys [37-39]. Their most interesting work is described in reference [39] where they studied the defect accumulation during martenstic transformation in FeMnSi shape memory alloys. They determined the phase transition temperatures of the shape memory alloys using the positron annihilation spectroscopy.

A number of studies have been published in which the annihilation characteristics of trapped positrons in cold rolled metals are described in terms of dislocations [40, 41]. U. Holzwarth et al. [42] carried out the positron lifetime measurements at room temperature before and after isochronal annealing of cylindrical, machined fatigued specimens and of round slabs of austenitic stainless steel AISI316L deformed in compression. Annealing experiments are evaluated in terms of vacancy migration with vacancy sinks at grain boundaries and dislocations.

Techniques for defect analysis There are many methods for detection of open volume defects. Transmission electron microscopy (TEM), scanning tunnelling microscopy (STM), atomic force microscopy (AFM) and optical microscopy (OM) are the most common used techniques. Neutron scattering and X-ray scattering are also used in defect spectroscopes. Each of these techniques has specific regions of high sensitivity and resolution. Howell et al. [43] compared the capabilities of these techniques and positron annihilation lifetime spectroscopy. Figure 1.3 shows the comparison of these techniques with PALS. Each method is displayed by its ability to resolve or detect defects of some size at some sample depth. PALS is effective in providing size information at any sample depth for defect sizes below the effective resolution of other generally applied techniques.

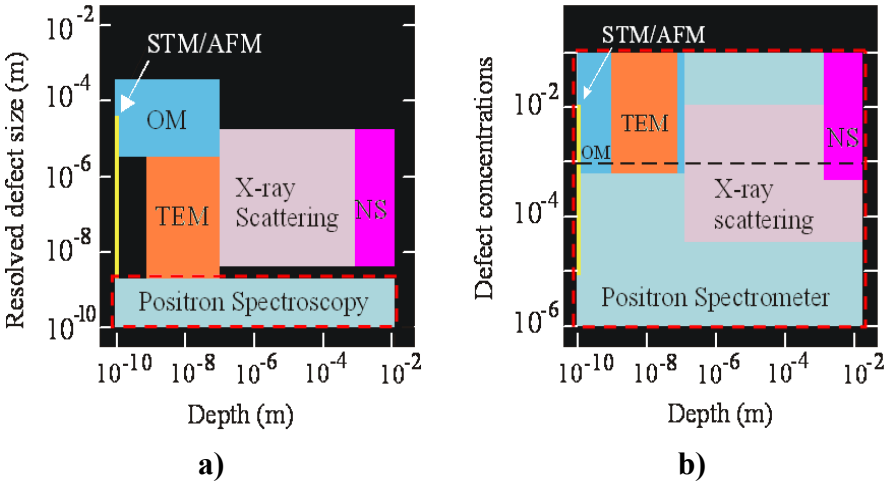

Figure 1.3 Comparison of positron annihilation spectroscopy to other techniques (according to Reference [43])

1.4 Aim of the work

The general aim of this doctoral thesis is to try to use the non-destructive Positron Annihilation Spectroscopy (PAS) technique together with X-ray diffraction (XRD), optical microscopy (OM) and other techniques to investigate the different kinds of defects formed during the deformation of iron based alloys. The FeMnSiCrNi shape memory alloy is the main material to be studied. The phase transformation, the effect of order of deformation and the annealing of these alloys has to be investigated. The goal also included the calculation of the defect concentration in these materials. The effect of increasing the Si content in the FeSi has to be studied. The different kinds of defects formed when the FeSi samples are deformed at high and room temperature has to be investigated.

1.5 Scope of this thesis

The thesis consists of 9 chapters and can in principle be divided into three main parts. The first part contains three chapters, where general aspects are described.

The second part contains 5 chapters with experimental results. Part 3 contains the last chapter where general conclusions of this work are summarized.
The structure of this thesis is as follows. The present chapter gives an overview of the materials used in this study and also the history of the positron physics.

A literature study about the materials used is presented in chapter 2. This chapter proceeds with discussing the principles of the positron annihilation spectroscopy. In chapter 3, the used experimental methods are described. The effect of annealing of deformed iron was studied in chapter 4. The recovery temperature range was detected using the positron annihilation measurements. The impurities affect the recovery temperature for the deformed iron. In chapter 5 a study of defects induced in FeSi, which is deformed at high temperature and low (room) temperature was done by positron annihilation spectroscopy (PAS). The effect of the Si content is also studied. The influence of adding C to the FeMnSiCrNi alloy is investigated in chapter 6. In chapter 7, the martensitic transformation and defects induced by the deformation (tensile strain) of a FeMnSiCrNiC alloy is described. Samples deformed from 2 to 20% will be used in this study to have an idea about the kind of defects formed and the phase transition takes place with increasing the tensile deformation. The effect of annealing of the FeMnSiCrNiC alloy is presented in chapter 8. The general conclusions of all the chapters and the future work as a consequence of the results of this thesis are included in chapter 9.

1.6 References

[1] D. P. Dunne, (2000) “Functional Memory, Metals”, Materials Forum: Materials and, processes of the 21st Century, Vol.24, The Institute of Materials Engineering Australasia Ltd, Australia.

[2] S. Kajiwara, Materials Science and Engineering A, 273–275, (1999) p.67.

[3] T. Maki, “Shape Memory materials”, editors, K. Otsuka, C. M. Wayman Cambridge University press, (1998) p.117.

[4] H. Otsuka, H. Yamada, T. Maruyama, H. Tanahashi, S. Matsuda, and M. Murakami, Trans ISIJ, 30(1990) p.674

[5] J. Van Humbeeck, G. Ghosh, L. Delaey, D. Segers., M. Dorikens and L. Dorikens-Vanpraet., conference of positron annihilation (1989) p.395

[6] A. Sato, E. Chishima, K. Soma, T. Mori, Acta Metallurgica, 30, (1982) p.1177.

[7] A. Sato, E. Chishima, K. Soma and T. Mori, Acta Metallurgica 34, (1986) p.287

[8] M. Murakami, H. Otsuka, H.G. Suzuki and S. Matsuda, Proceeding of the International Conference on Martensitic transformations (ICOMAT-86), Japan Inst. Met., (1986) p.985

[9] Y. Moriya, T. Sampei and I. Kozasu, Annual Meeting at Yokohama, Conf. Abstr, JIM, (1989) p.222

[10] K. Tsuzaki, Y. Natsume, Y. Kurokawa, T. Maki. Scripta Metall Mater 27, (1992) p. 471.

[11] J. H. Yang, H. Chen, C.M. Wayman, Metall. Trans.A 23, (1992) p.1431.

[12] T. Moriya, H. Kimura, S. Ishizaki, S. Hashizume, S. Suzuki, H. Suzuki, T. Sampei, J. Phys.(Paris) IV C4-1(1991) p.433.

[13] M. Wada, K. Natira, H. Naoi, T. Maruyama, Properties of pipe joints made of ferrous shape memory alloy, p.375.

[14] Y. Kameoka, T. Kasuya. J. Jpn. Soc. Civil Eng. 4**,** (1995) p.36.

[15] A. Sato, H. Kubo and T. Maruyama, J. Mater., Trans.47, (2006) p.571.

[16] D. Ruiz, et al., J. Appl. Phys. 93, (2003) p.7112.

[17] T. Ros, et al., J. Appl. Phys.91- 10, (2002) p.7857.

[18] P. A. M. Dirac A theory of electrons and protons. Proc. Roy. Soc. Lond. A, 126:360-365, (1930) p.360.

[19] C. D. Anderson. Phys. Rev., 43, (1933) p.491.

[20] C.D. Anderson. J. Science, 76, (1932) p.238.

[21] J. Thibaud. Positive electrons: Focusing of beams, measurements of charge-to-mass ratio, study of absorption and conversion into light. Phys. Rev., 45, (1934) p.781.

[22] S. Mohorivicic. Möglichkeit neuer Elemente und ihre Bedeutung für die Astrophysik. Aston. Nachr., 253, (1934) p.93.

[23] J. M. Ruark. Positronium. Phys. Rev., 68, (1945) p.278.

[24] M. W. Dumond, D. A. Lind and B.B. Watson "Precision measurement of the wavelength and spectral profile of the annihilation radiation from ^{64}Cu with the two- meter focusing curved crystal spectrometer" Phys. Rev. 75, (1949) p.1226.

[25] M. Deutsch "Evidence for the formation of positronium in gases" Phys. Rev., 82, (1951) p.455.

[26] R. E. Bell and R.L. Graham "Time distribution of positron annihilation in liquids and solids" Phys. Rev., 90, (1953) p.644.

[27] I. Ya G. Dekhtyar, D. A. Levine, and V. S. Mikhalenov, Dokl. Akad. Nauk SSSR156, (1964) p.795.

[28] S. Berko and J. C. Erskine, Phys. Rev. Lett.19, (1967) p.307.

[29] I. K. MacKenzie, T. L. Khoo, A. B. McDonald, and B. T. A. McKee, Phys. Rev. Lett.19, (1967) p.946.

[30] J. Arponen, P. Hautojarvi, R. Nieminen, and E. Pajanne, J. Phys. F 3, (1973) p.2092.

[31] M. Doyama and R. M. J. Cotterill, in *proceeding of the 5th international Conference on Positron Annihilation, Japan, 1979*, Edited By R. R; Hasiguti and K. Fujiwara (Japan Institute of metals, Sendai, (1979) p.89.

[32] P. Hautojirvi, A. Tamminen and P. Jauho, Phys. Rev. Lett., 24, (1970) p. 459.

[33] H. Fukushima and M. Doyma, J. Phys. F: Metal Phys.6, (1976) p.677.

[34] T. d. Troev, K. Hinode, S. Tanigawa and M. Doyama Appl. Phys.13, (1977) p.105.

[35] S. Tangigawa, K. Hinode, T. Yamauchi, Doyama, New Aspects of maternsitic transformation, Tokyo, Japan Inst. Metals, (1976)123-8.

[36] P. Hautojarvi, T. Judin, A.Vehanen, J. Yli-Kauppia, V. S. Mikhalenkov, Proc. 5th Int. Conf. on Positron Annihilation 1979.

[37] I. Hurtado, D. Segers, J. Van Humbeeck, L. Dorikens-Vanpraet and C. Dauwe, Scripta Metallurgica et Materiali, 33-5, (1995) p.741

[38] D. Segers, J. Van Humbeeck, L. Delaey, M. Dorikens and L. Dorikens, 'The study of defects in some CuZnAl alloys' in positron annihilation (world scientific, Singapore, 1985) p.880.

[39] J. Van Humbeeck, G. Gosh, L. Delaey and D. Segers, M. Dorikens, L. Dorikens-Vanpreat, proceeding of the ICPA-8, Gent-Belgium (1989) p.395.

[40] P. Hautojarvi, A. Vehanen, and V. S. Mikhalenkov, Appl. Phys. 11 191, (1976) p. 191.

[41] Y. K. Park, J. T. Waber, M. Meshii, Jr., C. L. Snead and C. G. Park, Phys. Rev. B 34, (1986) p.823.

[42] U. Holzwarth, A. Barbieri, S. Hansen- Ilzhöfer, P. Schaaff, M. Haaks, Appl. Phys. A-73, (2001) p.467.

[43] R. H. Howell, Thomas E. Cowan, Jay Hartley, Philip Sterne and Ben Brown. J. Applied surface science, 116, (1997) p.7.

Chapter 2
Literature study

The purpose of this chapter is to give an introductory overview on some general aspects of iron based alloys (FeSi electrical steel and FeMnSiCrNi shape memory alloys), their properties and applications.

2.1 FeSi electrical steel

2.1.1 Definition of steel

Steel is a hard, strong alloy of iron and carbon, usually containing between 0.02 and 1.5 wt.% carbon, often with other constituents such as manganese, chromium, nickel, silicon, molybdenum, tungsten, cobalt, or copper depending on the desired alloy properties. Steel is widely used as a structural material.

2.1.2 Electrical steels

Electrical steels are special flat steel products, which are soft magnetic materials, produced as thin steel sheets in the range of 0.15 to 1 mm thickness. The amount of production is about 1% of the worldwide steel production [1]. The addition of silicon increases the electrical resistivity of the steel, which decreases the induced eddy currents and thus reduces the core loss. Si-steel is the soft magnetic material, which is most in demand. It represents about 80% of the total production of soft magnetic materials. At a silicon content of approximately 6.5 wt.%, the magnetic permeability increases to a maximum value and magnetostriction falls to zero. At the other side when the silicon content exceeds the workability is dramatically reduced, making it extremely difficult to produce thin silicon steel sheets by the traditional hot-cold rolling process.

The concentration levels of carbon, sulfur, oxygen and nitrogen must be kept low in the alloying process as these elements are responsible for the presence of carbides, sulfides, oxides and nitrides in the alloy. These compounds increase hysteresis losses.

2.1.3 Types of electrical steel

There are many types of electrical steels such as lamination steels, non-oriented and grain-oriented electrical steels.

The lamination steels are alloyed with 0.2 to 0.8 wt.% Mn and 0.03 to 0.15% P for resistivity. Carbon is added up to 0.08%. They are used for the alternating current applications in which magnetic properties are not very critical [2].

The grain-oriented electrical steels reveal a high anisotropy of the magnetic properties. They have superior magnetic properties in the rolling direction. They are developed to provide a low core loss and high permeability, which are obtained through a combination of a well-defined chemical composition, rolling and heat treatment. For that reason the grain-oriented electrical steels are basically used in magnetic cores of transformers, where the magnetic flux is mainly following one direction. Grain oriented steels are expensive compared to the non-oriented steels.

Non-oriented steels are widely used as the magnetic core material in a variety of electrical machinery and devices, particularly in motors where low core loss and high magnetic permeability in all directions of the strip are desired. Magnetic properties of non-oriented electrical steels are improved by the control of the chemistry, the grain size and the texture. The electrical steels, which are used in rotating electrical machines or in transformers, have to be processed in order to satisfy the industry requirements concerning magnetic and mechanical properties. This means that they have to have low power losses, a high permeability and a good cutting behavior [3].

We have to mention that, the FeSi steel used in the present work is non-oriented electrical steel.

2.1.4 Magnetic properties

There are many properties that affect the final product of the electrical steel. The most important properties are:

2.1.4.1 Magnetic Permeability

The permeability μ is the degree of magnetization of a material that responds linearly to an applied magnetic field. It is a constant of proportionality that exists between magnetic induction *B* and magnetic field intensity *H*. It is determined as follows:

$$\mu = B/H \qquad (2.1)$$

2.1.4.2 Magnetostriction

It is a property of ferromagnetic and also ferrimagnetic materials that causes them to change their dimensions in the presence of a magnetic field. Ferromagnetic materials have a structure divided into domains, each of which is a region of uniform magnetic polarization. When a magnetic field is applied to the material, the boundaries between the domains shift and the domains rotate. Both of these effects cause a change in the material's dimensions [4]. The materials exhibiting a large magnetostriction can be used for various sensor applications, because it influences the shape of the loop. Even though the magnetostriction of the FeSi alloys is small (below 10 ppm), it is responsible for the acoustic noise in transformers.

2.1.4.3 Core loss

In transformers or inductors, some of the power that would ideally be transferred through the device is lost in the core, resulting in heat. There are many reasons for such losses:

1. Hysteresis loss The larger the area of the hysteresis loop, the more loss per cycle. Hysteresis loss is a heat loss caused by the magnetic properties of the armature. When an armature core is in a magnetic field, the magnetic particles of the core tend to line up with the magnetic field. When the armature core is rotating, its magnetic field keeps changing direction. The continuous movement of the magnetic particles, as they try to align themselves with the magnetic field, produces molecular friction. This molecular friction produces heat. Hysteresis loops are obtained by applying a cyclic magnetic field H to the specimen and by recording the magnetic induction B along the field direction. It can take a variety of different forms. The method of determining the hysteresis loop depends on the type of magnetic material. Soft magnetic materials need a high resolution at low fields, while hard magnetic materials need sufficiently high external fields.

2. Eddy current loss

The induction of eddy currents within the core causes a resistive loss. The higher the resistance of the core material the lower the loss will be. Lamination of the core material can reduce the eddy current loss.

3. Movement of magnetic domains

As the magnetic field changes, some magnetic domains grow while others shrink, thus the walls of the domains can be said to move. This movement absorbs energy.

Soft magnetic materials These materials are easily magnetized, where a low coercive field is a prime requirement. The main application of these materials is the cores of rotating electrical machines and transformers. The parameter, often used as a figure of merit for soft magnetic materials, is the relative permeability (μ_r), which is a measure of how readily the material responds to the applied magnetic field. The other main parameters of interest are the coercivity and saturation magnetization, which are characterized by the hysteresis loop. The loop should exhibit a small area, which is proportional to the losses.

Hard magnetic materials These materials are stable and are a permanent source of magnetic field, insensitive to external actions. They are characterized by a broad hysteresis loop. Hysteresis loops may take many different shapes. There are two important quantities, which are the remanent magnetization (remanence, M_r and coercive field H_c).

Remanence It is the natural quantity expressing the fact that the ferromagnetic material can be spontaneously magnetized even in the absence of external actions.

Coercive field This is the field needed to bring magnetization from the remanent value to zero. It measures the order of magnitude of the fields that must be applied to a material in order to inverse its magnetization. Materials can be classified according to the values taken by these parameters. It is common to subdivide materials into soft and hard magnetic materials [5].

2.1.5 Chemical composition

To have different applications for the iron alloys, small amounts of selected elements should be added to modify its properties. An example for that is the addition of Si or Al that produce a significant increase in the resistivity. The details of the iron-rich side of the FeSi phase diagram shown in Figure 2.1 indicate that silicon is soluble in α-Fe up to about 4 wt.%. Beyond that limit, the brittle intermetallic Fe_3Si (with a B_2 or DO_3) phase may also be present.

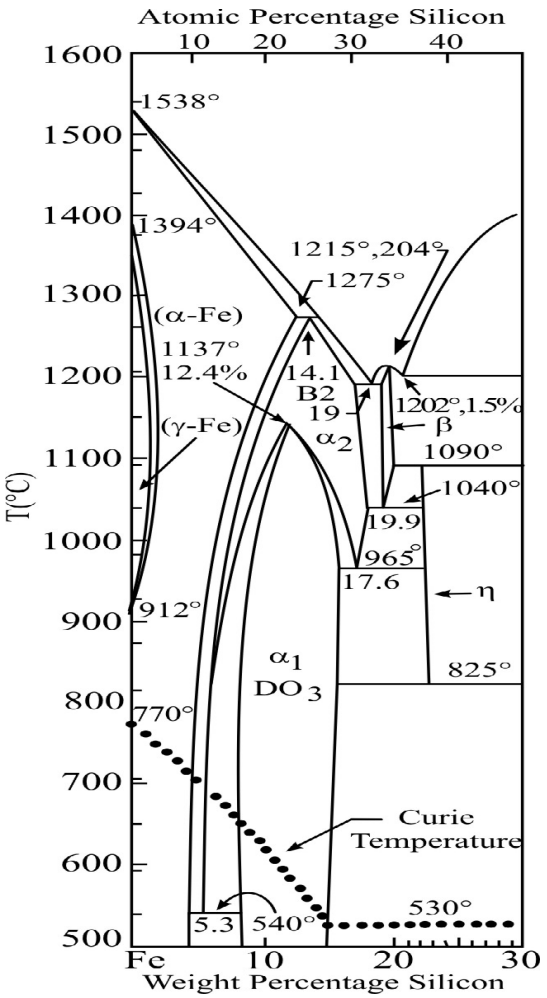

Figure 2.1 Fe-Si phase diagram

The addition of Si to iron causes changes in a number of physical properties (Figure 2.2). It is known that Si not only increases the electrical resistivity but also significantly reduces the magnetic anisotropy and has little effect on magnetostriction up to 4 wt.%.

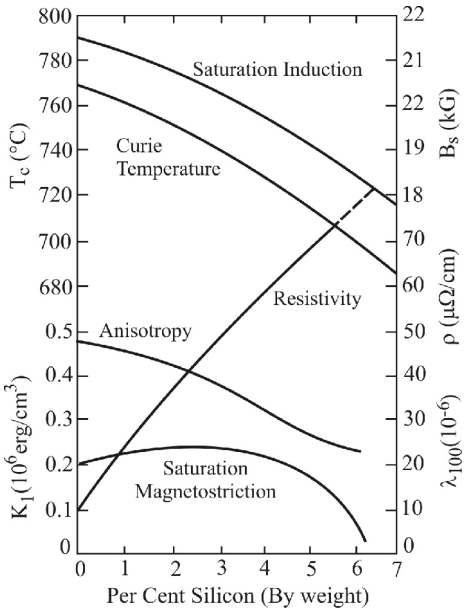

Figure 2.2 Variation of physical properties of iron with Si content [6]

The addition of Si to iron produces significant effects in lowering the core loss. Figure 2.3 shows a monotonic decrease in the core loss of low carbon steel with increasing Si content (increasing resistivity) and lower core loss for thinner gauge sheet [6].

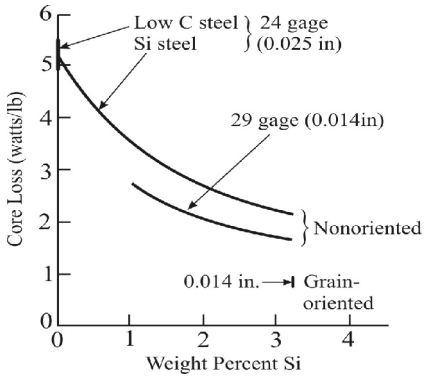

Figure 2.3 Core loss at 60 Hz and 15 kG for low-carbon and silicon steels.

2.2 FeMnSi Shape memory alloys

Shape memory alloys are a unique class of metal alloys that can recover apparent permanent strains when they are heated above a certain temperature. The shape memory alloys have two stable phases - the high–temperature phase, called austenite, and the low–temperature phase, called martensite. There are different kinds of SMAs, and this study is concerned about the FeMnSi systems.

FeMnSi based shape memory alloys have been widely studied in recent years. It has been found that the efficiency of the shape memory FeMnSi based alloys is affected by many factors such as pre-strain [7, 8] deformation temperature [9, 10], annealing treatment [11, 12] and thermo-mechanical training [9, 11-14]. All of these effects are highly correlated with $\gamma \leftrightarrow \varepsilon$ transformation, which governs the shape memory effect in FeMnSi based shape memory alloys.

2.2.1 Shape memory effect (SME)

The SME is a unique property of certain alloys exhibiting martensitic transformations. If the alloy is deformed in the low temperature phase, it recovers to its original shape by the reverse transformation upon heating above a critical temperature called the reverse transformation temperature (see Figure 2.4). This effect was first found by Chang and Read in an AuCd alloy [15]. SMAs could also have the super-elasticity (SE) property at a higher temperature, which is associated with a large nonlinear recoverable strain upon loading and unloading.

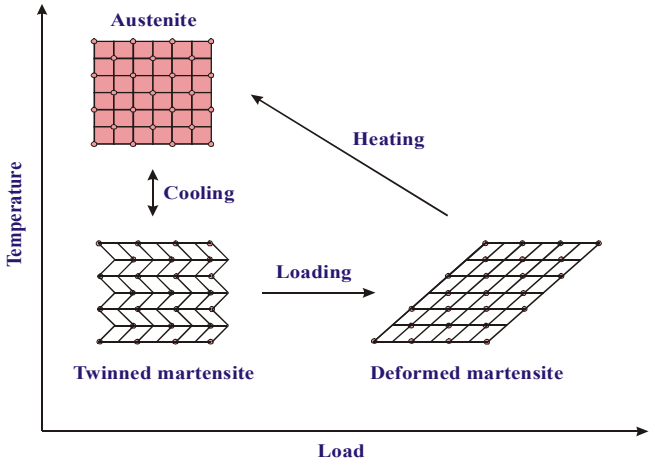

Figure 2.4 Microscopic Diagram of the Shape Memory Effect

2.2.1.1 One- way shape memory effect

The one-way shape memory effect refers to the memorization of one shape, i.e. the original 'hot shape', which is recovered on reheating a deformed sample. The only restriction is that the deformation may not exceed a certain strain limit (up to 8%) [16]**;** as long as the total strain does not induce permanent plastic flow (see Figure 2.4). The deformation may be of any type (e.g. tension, compression, bending or more complex combinations).

During the one–way shape memory effect internal structural changes take place. When a load is applied to the self–accommodated martensite, the structure becomes deformed through variant rearrangement, resulting in a net macroscopic shape change. When the alloy is unloaded this deformed structure remains, resulting in an apparent permanent strain. If the alloy is now reheated to a temperature above the martensitic transformation range, the original parent phase microstructure and macroscopic geometry is restored. This is possible because no matter what the post–deformation distribution of martensite variants are, there is only one reversion pathway to the parent phase for each variant [17]. If the alloy is cooled again under the martensitic finish temperature, a self–accommodated martensite microstructure is formed and the original shape before deformation is retained. Thus a one–way shape memory is achieved.

2.2.1.2 Two- way shape memory

In the one-way shape memory effect there is only one shape remembered by the alloy. That is the parent phase shape (so-called hot shape). The two-way shape memory effect is the effect that the material remembers two different shapes: one at the low temperature, and one at the high temperature. This can be achieved without the application of an external force (intrinsic two way effect). The two-way shape memory effect is only obtained after a specific thermo-mechanical treatment, called training.

2.2.1.3 Pseudo-elasticity or the super-elastic effect

It is possible to induce a phase transformation by applying a pure mechanical load isothermally at a temperature above austenite finish temperature. The result

of this load application is fully detwinned martensite and very large strains are observed. The martensite formed in this way is known as stress–induced martensite and is only stable under the application of stress. On unloading, the reduction in stress and surrounding elastic forces generated during the transformation cause the martensite to return back to the original parent phase. This effect is known as pseudo-elastic or super-elastic effect [17]. Reversible strains up to 8% of the initial length can be obtained, compared to 0.2% elastic strain of a common metallic material. Figure 2.5 shows the mechanical behavior of such super-elastic material, and compares it with a conventional metallic alloy.

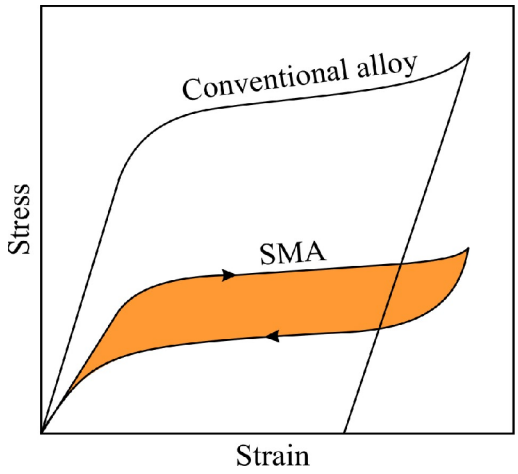

Figure 2.5 Comparison of the stress–strain curves of conventional and super-elastic alloys [17].

Since both SME and SE are related to the martensitic transformation (MT), so we should define the MT process here.

2.2.2 Martensitic transformation (MT)

MT is diffusion less phase transformation in solids, in which atoms move cooperatively, and often by a shear- like mechanism. Usually the parent phase (the high temperature phase) is cubic, and the martensite phase at lower temperatures has a lower symmetry (see Figure 2.6) [18, 19].

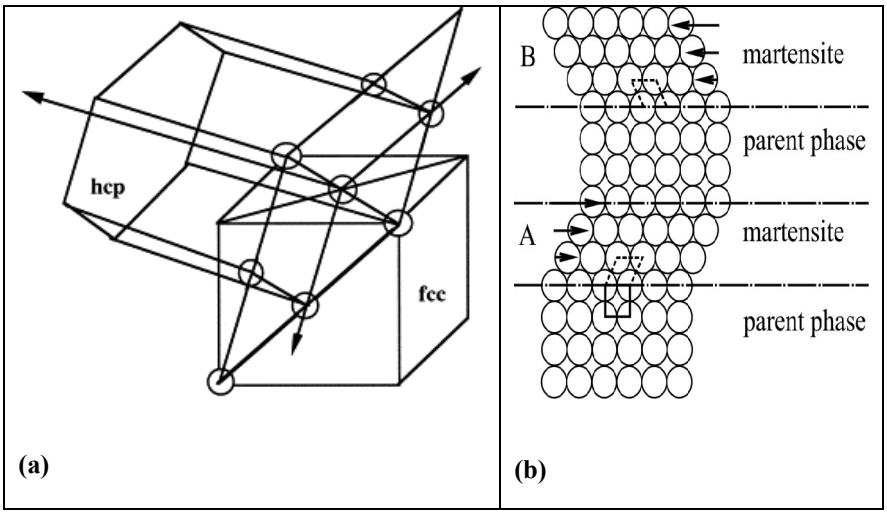

Figure 2.6 (a, b) Schematic representation of the relation between the parent phase and the martensite phase [16- 17]

When the temperature is lowered below the critical value (martensite start temperature M_s), the MT starts by a shear-like mechanism. Figure 2.6 shows the crystallographic structure after the transformation. The martensite in region A and in region B, have the same crystallographic structure, but the orientations are different. These are called the corresponding variants of the martensite. Since the martensite has a lower symmetry, many variants can be formed from the same parent phase. If the temperature is raised, the martensite becomes unstable and the reverse transformation occurs. If the transformation is crystallographically reversible, the martensite reverts to the parent phase with the original orientation. The phase transformation can be determined by measuring some physical properties such as the change in the electrical resistivity with temperature (see Figure 2.7), or by measuring the positron annihilation lifetime and the S parameter (will be described in more detail in the next chapters).

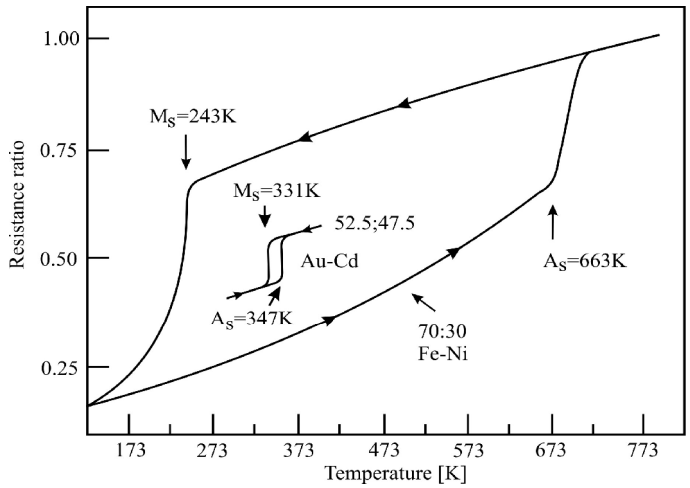

Figure 2.7 Electrical resistance changes during cooling and heating FeNi and AuCd alloys, illustrating the hysteresis of the martensitic transformation on cooling, and the reverse transformation on heating, for non-thermoelastic and thermoelastic transformations respectively [18].

2.2.3 Morphology and substructure of ferrous martensite

In Ferrous alloys, a FCC austenite (γ) is transferred to three kinds of martensites with different crystal structures depending on alloying elements and compositions:

1) $\gamma \rightarrow \alpha'$ (BCC or BCT) martensite

2) $\gamma \rightarrow \varepsilon$ (HCP) martensite

3) $\gamma \rightarrow$FCT martensite

Table 2.1 Some Fe- based SMAs and their martensite structure

Alloy	Composition	Martensite
FePt	25 at% Pt	α' (BCC, BCT)
FeNiCoTi	23% Ni-10%Co-10%Ti	α' (BCC, BCT)
	33% Ni-10%Co-4%Ti	α' (BCC, BCT)
	31% Ni-10% Co-3%Ti	α' (BCC, BCT)
FeNiC	31%Ni-0.4%C	α' (BCC, BCT)
FeNiNb	31%Ni- 7%Nb	α' (BCC, BCT)
FeMnSi	30%Mn-1%Si	ε (HCP)
	(28 - 33)%Mn-(4-6)%Si	ε (HCP)
FeMnSiC	17%Mn-6%Si-0.3%C	ε (HCP)
FeMnSiCrNi	(8-20)%Mn-(5-6)%Si	ε (HCP)
	-(8-13)%Cr-(5-6)%Ni	
FePd	30at%Pd	FCT
FePt	25at%Pt	FCT

The most popular ferrous martensite is α' formed in FeC and FeNi alloys. The ε martensite is formed only in ferrous alloys with low stacking fault energy such as FeCrNi and Fe alloys with a high content of Mn. A shape memory effect has been observed in each of the three types of ferrous martensites. The ferrous shape memory alloys are listed in Table 2.1 [20]. The martensite morphology of all these alloys is a thin plate type with a planar interface.

2.2.4 Thermodynamic aspects

The martensitic phase transformation temperatures are:

M_s (martensite start temperature),

M_f (martensite finish temperature),

A_s **(**reverse transformation start temperature)

A_f (reverse transformation finish temperature). It is the temperature above which the martensite becomes completely unstable.

Since the martensitic transformations are not associated with a compositional change, the Gibbs free energy curves of both parent and martensite phases as a function of temperature may be represented as schematically shown in Figure 2.8, where T_0 represents the thermodynamic equilibrium temperature between the two phases. The driving force for diffusion less transformation is the difference in free energy between the martensite and the parent phase (austensite). ΔT_S is the super-cooling required for nucleation of a martensitic transformation.

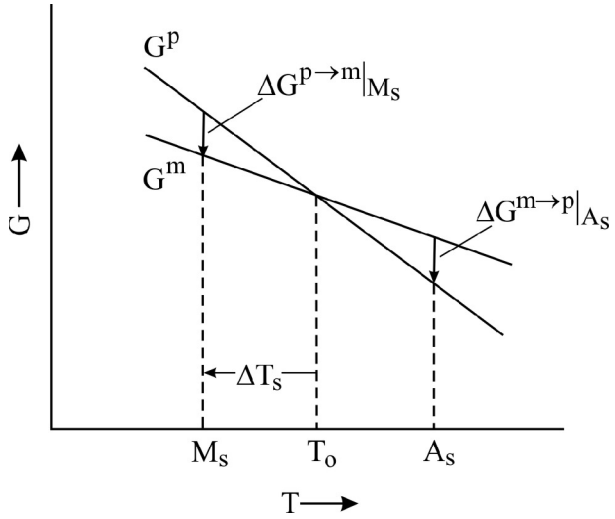

Figure 2.8 Schematic representation of free energy curves for both parent and martensitic phases, and their relation to the M_s and A_s temperatures.

The distinction between the thermal martensite, stress induced and strain induced martensite

Thermal martensite is formed by cooling below the martensitic start temperature M_s. As the stress level increases, pre-existing nuclei can be activated at a higher temperature (see Figure 2.9): (stress induced martensite). When the stress reaches the yield strength of the parent austenite, at the M_s^{σ} temperature, plastic deformation further assists the transformation by creating additional nuclei.

M_s^{σ} occurs where the stresses needed to originate the stress induced transformation exceed the yield stress of the austenite; therefore the strain induced transformation is activated at new sites produced by plastic deformation. Below M_s^{σ}, the yielding is initiated by transformation, and above M_s^{σ}, the yielding is initiated by slip or dislocation glide. Finally a temperature, M_d, is reached when the insufficient driving force exists for any nuclei to be created and consequently the transformation does not occur at temperatures above M_d.

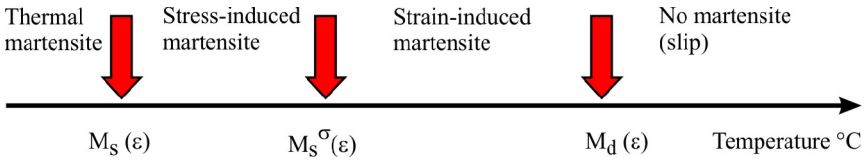

Figure 2.9 The characteristic temperatures for the martensic transformation [20].

2.2.5 Conditions for shape memory and super-elastic characteristic

The shape memory effect (SME) and the super-elasticity (SE) are closely related phenomena. The relation between them is shown in Figure 2.10. Both can be observed in the same specimen depending upon the test temperature as long as the critical stress for slip is high enough. SME occurs below A_s, followed by heating above A_f, while SE occurs above A_s, where martensites are completely unstable in the absence of stress. In the temperature regime between A_s and A_f, both occur partially. The essential conditions for the realization of SME and SE are the crystallographic reversibility of the martensitic transformation and the avoidance of slip during deformation.

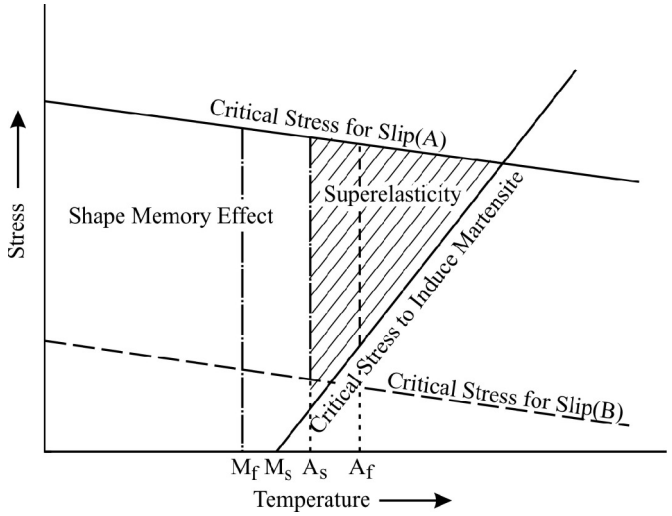

Figure 2.10 Schematic diagram representing the region of shape memory effect and super-elasticity in temperature-stress coordinates

2.2.6 Shape memory effect (SME) associated in FeMnSi alloys

2.2.6.1 FeMnSi shape memory alloys

It was found that the shape memory effect of FeMnSi alloys is remarkably increased by introducing of a slight deformation (2.5%) and annealing at about 873 K [21]. This kind of treatment is called 'training'. After 5 cycles of training, a perfect shape memory effect is achieved. This treatment suppresses slip deformation through introducing dislocations (which raise the strength of the austenite matrix) and generates martensite at lower stress through introducing stacking faults in austenite (which act as nucleation sites for ε martensite).

2.2.6.2 General features of γ→ ε martensitic transformation and ε→γ reverse transformation

The γ → ε martensite transformation is produced by the motion of a/6<112> Shockley partial dislocations on every second (111) austenite plane. The stress-induced ε band consists of a single variant. The thermally induced or spontaneous transformation of ε martensite is known to be generally self-accommodating. The stress- induced ε transformation is generally accompanied

by the selective motion of a single type of Shockley partial dislocation being most favorable to the direction of the applied stress. Therefore, the stress-induced ε band consists of a single variant. The ε → γ reverse transformation occurs by the motion of Shockley partial dislocations with three kinds of equivalent shear directions in a similar way to the γ→ ε forward transformation. This reversible movement of transformation dislocation in FeMnSi alloys has been confirmed by surface relief observation of ε martensite upon heating above A_f temperature. The surface relief of the ε martensite in these alloys almost completely disappears with the reverse transformation [18].

2.2.7 The effect of alloying elements

● **Mn** affects phase and magnetic transformation temperatures. The M_s temperature decreases as the Mn content increases (Figure 2.11), while the Néel temperature (T_N) increases. At certain Mn content, T_N becomes equal to M_S. For higher Mn content, where T_N lies above M_s, no ε martensite forms spontaneously because of the stabilization of austenite due to anti-ferromagnetic ordering. If T_N lies above M_s, even the stress induced transformation does not take place and no SME is observed. If T_N is lower than M_S, the austenite is not stabilized. For Mn contents from 28 to 34 wt.%, the M_s temperature lies above the room temperature, which allows the existence of thermally induced martensite which suppresses the stress assisted formation of martensite and leads to the degradation of the SME.

● **Si** lowers the stacking fault energy of the austenite. In addition, Si is a solid solution hardening element, which increases the yield stress of the parent austenite phase and prevents the permanent deformation by slip.

● **Co** also lowers the stacking fault energy of austenite. FeMnCo alloys [22] only exhibit a small shape memory effect comparable to FeMn binary alloys. This is very likely due to the fact that Co does not sufficiently strengthen the austenite matrix.

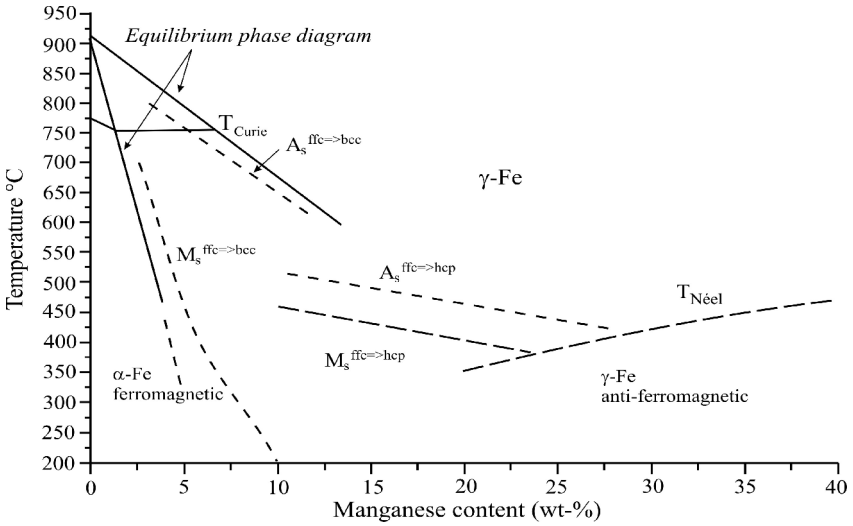

Figure 2.11 Thermodynamic equilibrium as a function of the Mn content in the FeMn alloy [14]

● **Ni** lowers the M_S temperature. Ni is a γ stabilizer, which suppresses the formation of ferrite and the σ phase precipitation [23]. The presence of the inter-metallic σ phase reduces the fracture toughness of the alloy. Otsuka et al. [21] found evidence for the presence of the σ phase in a Fe–25 wt.%Mn– 6 wt.%Si–9 wt.%Cr alloy which had an initial shape recovery of more than 60% after a 2.5% strain deformation, but which broke when the deformation and heating cycles were repeated.

● **Cr** is added to improve the corrosion resistance. The yield stress of the austenite increases by adding Cr. An increasing Cr content lowers the M_S temperature. Cr also lowers the stacking fault energy.

● **the interstitial impurities C and N** readily strengthen the parent austenite phase, they may also form carbides and nitrides. The presence of precipitates can cause the SME to occur incompletely by suppressing the mobility of the austenite/martensite interface [24, 25].

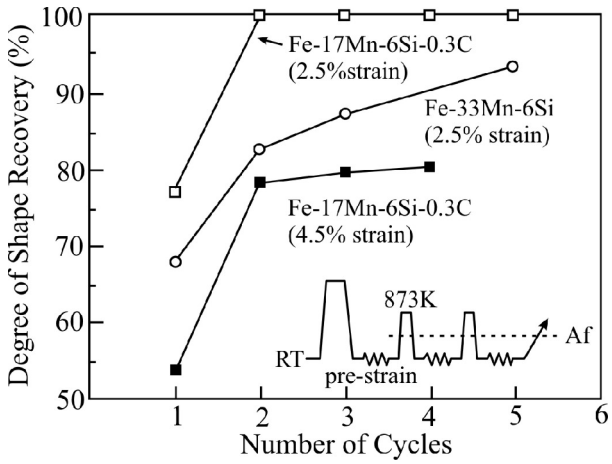

Figure 2.12 Change in the degree of shape recovery with increase in the training cycles in some FeMnSi alloys

Interstitials also influence the stacking fault energy; whereas C increases the stacking fault energy, N decreases it. C and N are also known to influence the ordering of the substitutional elements. The nitrogen atoms favor short range ordering. In contrast, C atoms have a tendency to cluster [26]. Tsuzaki et al. [27] have found that the shape memory effect is improved by the addition of C as shown in Figure 2.12. The effect of carbon is investigated in more details in chapter 6. The phase transformation temperatures, the magnetic transformation temperature and the recovered strain as a function of composition are listed in Table 2. 2.

Table 2.2 Composition dependence of phase and magnetic transformation temperatures and recovered strain

Specimen	Composition (wt.%)				Recovered strain (%)	Transformation températures (K)		
	Mn	Si	Cr	Ni		M_s	A_s	T_N
14Mn-6Si-9Cr-5Ni	13.6	6	9.2	4.8	0.97	-	400	-
l5Mn-6Si-9Cr-5Ni	14.7	6	9.2	4.9	1.11	-	389	-
16Mn-6Si-9Cr-5Ni	15.7	5.9	9.2	4.9	1.55	-	394	-
11Mn5Si-12Cr-7Ni	11.2	4.7	11.6	6.7	1.35	266	369	-
l3Mn-5Si-12Cr-7Ni	13.0	4.7	11.4	6.8	1.64	243	367	-
l6Mn-5Si-12Cr-5Ni	16.0	5.0	11.6	4.9	1.45	267	382	169

2.2.8 Applications of shape memory alloys

Shape memory alloys have a wide range of applications in different fields. NASA uses them in the space industry. They are used in many biomedical applications. Table 2.3 summarizes the applications of the One-Way SME, the Two-Way SME and the Super-elastic shape memory alloys.

Table 2.3 The applications of the One-Way SME, the Two-Way SME and the Super-elastic shape memory alloys.

Super-elastic Devices:	One Way SME:	Two Way SME:
Medical Guide wires	Pipe Coupling	Electrical Connectors
Medical Guide pins	Vibration Dampers	Coffee pot thermostats
Surgical Localization-Hooks	Bendable Surgical	Water temperature controller
Eyeglass Frames		Green house window actuator
Cellular Telephone-Antennas		Satellite Release Bolts
		Aero-space Actuators

Some other applications:

Broken bones can be mended with shape memory alloys. The alloy plate has a memory transfer temperature that is close to body temperature, and is attached to both ends of the broken bone. From body heat, the plate wants to contract and retain its original shape, therefore exerting a compression force on the broken bone at the place of fracture. After the bone has healed, the plate continues exerting the compressive force, and aids in strengthening during rehabilitation.

Dental wires: used for braces and dental arch wires, shape memory alloys maintain their shape since they are at a constant temperature, and because of the super elasticity of the shape memory alloys, the wires retain their original shape after stress has been applied and removed.

Golf Clubs: A new line of golf putters and wedges has been developed using shape memory alloys are inserted into the golf clubs.

2.3 References

[1] O. Fischer and J. Schneider. J. Magnetism and Magnetic Materials, 254 - 255, (2003) p.302.

[2] P. R. Calvillo, Deformation Analysis of High Si-Steel during Torsion and Compression Testing, Ph.D thesis, Ghent University, Ghent (2007).

[3] P. Baudouin, Y. Houbaert. J. Magnetism and Magnetic Materials, 260-2, (2003) p.19.

[4] E. Harry Burke, Handbook of magnetic phenomena, Van Nostrand Reinhold Company Inc, US (1986).

[5] G. Bertotti, Hysteresis in Magnetism, Academic Press, Inc. USA, (1998)

[6] Robert C. O'Handley, Modern Magnetic Materials: Principles *and Applications* (John Wiley & Sons, New York, 2000).

[7] J. S. Robinson and P. G. McCormick. Scripta Metall. 23, (1989) p.1975.

[8] J. S. Robinson and P.G. McCormick, J. Mater. Sci. Forum56– 58, (1990) p.649.

[9] H. Inagaki. *Z. Metall.* 83 (1992) p.90.

[10] A. Sato, E. Chishima, T. Mori. *Acta Metall.* 32, (1984) p.539.

[11] Z.Nishiyama, Martensitic Transformation, Academic Press, (1978) p.306.

[12] G. Ghosh, Y. Vandereken, J. Van Humbeeck, M. Chandraekaran, L. Delaey and W. Van Moorleghem. *Proc. MRS Int. Meet. Adv. Mater.*9, (1989) p.457.

[13] H. Otsuka, M. Murakami, S. Matsuda. *Proc. MRS Int. Meet. Adv. Mater.*9, (1989) p.451.

[14] D. Dunne and H. Li. J. Phys. (France) IV 5 (1995) p.C8– 415.

[15] L. C. Chang, T. A. Read. Trans. AIME, 189, (1951) p. 47.

[16] J. Van Hambeeck Advanced engineering Materials 3, No11, (2001) p.837.

[17] K. Worden, W. A. Bullough, J. Haywood, Smart technologies, World Scientific, (2003) p.109.

[18] K. Otsuka,C. M. Wayman, Shape memory materials, Cambridge University press (1998).

[19] Huijun Li, Druce Dunne, and Noel Kennon, Materials Science and Engineering A, 273-275, (1999) p.517.

[20] N. Van Caenegem, Recovery as a result of the martensitic transformation in FeMnSi-based shape memory, Ph.D thesis, Ghent University, Ghent (2007-2008).

[21] H. Otsuka, H. Yamada, T. Maruyama, H. Tanahashi, S. Matsuda and M. Murakami: ISIJ Int., 30, (1990) p.674.

[22] L. M. Kaputkina and V. G. Prokoshkina: J. Phys. IV Fr., 112, (2003) p.263.

[23] Q. Gu: Doctoral dissertation, Katholieke Universiteit Leuven, Belgium (1994).

[24] D. Dulieu and J. Nutting: Iron Steel Inst., 86, (1964) p.82.

[25] S. Miyazaki and K. Otsuka: ISIJ Int., 29- 5, (1989) p.353.

[26] V. G. Gavriljuk and H. Berns: High Nitrogen Steels, Springer-Verlag, Berlin and Heidelberg, (1999) p.14.

[27] K. Tsuzaki, Y. Natsume, Y. Kurokawa, T. Maki, Scr. Metal.27, (1992) p.471.

[28] P. Hautojarvi, L. Pollanen, A. Vehanen, J. Yli-Kauppila, J. Nucl. Mater.114, (1983) p.250

[29] A. Vehanen, P. Hautojarvi, J. Johansson, J. Yli-Kauppila, P. Moser, Phys. Rev. B 25, (1982) p.762

[30] E. A. Kummerle, K. Badura, B. Sepiol, H. Mehrer, and H. E. Schaefer, Phys. Rev. B 52, (1995) p.6947.

Chapter 3

Positron annihilation spectroscopy (PAS)

Introduction

The first application of positron annihilation to the study of solid states was in the 1942 [1]. The antimatter equivalent of the electron, the positron, turns out to be an extremely sensitive probe for studying both structural and electronic properties of the solid lattice. In addition, the source intensities, typically required for most useful experiments are sufficiently low that probe-induced radiation damage is negligibly small. Tremendous advances in positron/solid-state research were made; not only in the understanding of some of the fundamental aspects of positron-solid interactions but also in the development of new techniques and applications [2]. Positron annihilation is quite sensitive to lattice defects and is becoming a common technique used in the study of lattice defects and phase transition.

In the present chapter we will briefly discuss some of the fundamental aspects of positron annihilation spectroscopy, the most common experimental techniques, and at the end we will talk about the experimental techniques that have been used in our study.

3.1 Annihilation of positrons in solids

When a positron approaches a solid surface it may be scattered back or may penetrate the sample. In the latter case, the positron rapidly loses its high kinetic energy, i.e. it thermalizes and diffuses into the sample. The kinetic energy of the positron is decreased to kT, where T is the temperature of the material and k is

Boltzmann's constant = 1.38×10^{-23} J/K. The positron diffuses with this energy until it annihilates with an electron, which is relatively far from the nucleus (conduction electron). As a result of this annihilation, two gamma rays are emitted in most cases, each with an energy of 511 keV by the Einstein relation $E = mc^2$, where c is the velocity of light and m is the rest mass of an electron or positron. It is these γ-rays that are detected in the positron annihilation spectroscopy, and it is by means of these that one can probe the electronic and atomic environment from which the positron annihilates. The positron may be localized during its diffusion by traps, such as lattice defects, and then annihilates from a localized state.

3.1.1 Annihilation rate

The electromagnetic interaction between electrons and positrons leads to the creation of gamma photons. The number of photons involved indicates the type of annihilation, such as two-gamma or three-gamma annihilation. The emission of two gamma photons has almost 100% probability in dense materials.

$$e^+ + e^- \rightarrow 2\gamma \qquad (3.1)$$

The annihilation probability per unit time (the annihilation rate λ) can be obtained from the non-relativisitic limit of the 2γ annihilation cross section derived by Dirac [3].

$$\lambda = \pi r_0^2 c n_e \qquad (3.2)$$

Where, r_0 is the classical radius of electron or positron which is $r_0 = e^2/m_0c^2 = 2.8\times10^{-15}$ m, c is the velocity of light and n_e is the electron density at the site of the positron.

The equation above shows that λ is independent of the positron velocity. The electron density can be calculated if the annihilation rate λ, which is the inverse of the lifetime τ is known.

3.1.2 Linear momentum contribution

If the positron-electron pair is at rest at the instant of annihilation, then the 2γ photons are emitted in exactly opposite directions. The kinetic energy of the annihilation pair is typically a few electron volts. In their center of mass frame the photon energy is $m_o c^2$ = 511 keV and the photons are moving strictly into opposite directions. Because of the nonzero linear momentum of the electron – positron pair, the pair the photons deviate from co-linearity in the laboratory frame. From Figure 3.1 the deviation angle θ is given as:

$$\theta = P_T / m_0 c \qquad (3.3)$$

P_T is the linear momentum component of the electron – positron pair transverse to the photon emission direction. 180°- θ is the angle between the two photons in the laboratory frame. The value of the linear momentum of the electrons in metals, based on the free electron model is of the order of 1.5×10^{-24} kg.m/s. In the laboratory frame the centre of mass is not at rest. Moreover the angle between the photons deviates from 180° if the positron-electron linear momentum is not along the line of emission of the two photons. This is shown in Figure 3.1.

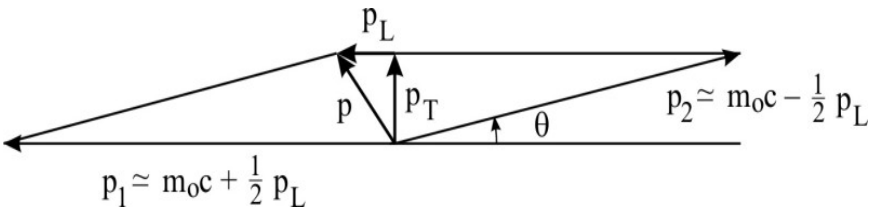

Figure 3.1 The vector diagram of the linear momentum conversation in the 2γ-annihilation process. P is the momentum of the annihilation pair, subscripts L and T refer to longitudinal and transverse components, respectively.

3.1.3 Positronium

Positronium is a hydrogen-like atom composed of an electron and a positron, which is formed as a positron is slowed down in matter (typically an insulator) and captured by an electron. Two forms are known: para-positronium (p-Ps) and ortho-positronium (o-Ps). Para-positronium the singlet $^1S_0$ state, in which the spins of the positron and electron are oppositely directed (antiparallel spins), decays by annihilation into two photons, with a mean life of about one-tenth of a nanosecond (or 10^{-10} second). Ortho-positronium the triplet $^3S_0$ state, in which the spins are in the same direction (parallel spin), annihilates into three photons with a mean life of about 100 nanoseconds (10^{-7} second).

The existence of positronium was predicted by Mohorovicic in 1934 [4]. The name "positronium" was introduced by A. E. Ruark in 1945 [5]. It was discovered by M. Deutsch in 1951 The Schrödinger equation for positronium is identical to that for hydrogen, where the reduced mass of the hydrogen atom is replaced by one half of the electron mass (Akhiezer and Berestetskii (1965)) [6]. The energy difference between these spin states (hyperfine splitting) is 8.4×10^{-4} eV.

3.1.3.1 Formation of positronium

The electron density in matter must be sufficiently low in order to allow the formation of positronium. In metals, it is hard to talk about positronium. The high density of free electrons there will prevent the positron to bind with a single electron and forming a positronium [7].

There are several models for positronium formation, which were reviewed in a monograph by Mogensen (1995) [8]. In the Ore- gap model (1949) [9], positronium is formed during slowing down of positrons at energies E_+ in the "Ore gap", E_{ion}- 6.8 eV < E_+< E_{ion}. E_{ion} is the ionization energy of molecules or atoms in the crystal, i.e. the energy necessary to release the electron for the Ps formation. This model can only be applied for solids.

There is another model which is called the bubble model of the Ps states in liquids was introduced by Ferrell (1958) [10]. The most accepted model nowadays is the "spur model" by Mogensen (1974) [11]. Positronium is formed mainly by the reaction between the positron and an excess electron in the spur. The positron spur is the terminal track of the positron, formed when it loses the last part of its kinetic energy.

The blob model for Ps formation was introduced by Byakov and Stephanov [12]. They concentrated on calculating the intensity of the long lifetime component, particularly its dependency on an applied electrical field, but they ignored the details of the sub nanosecond behavior of positrons and the age-dependent formation of Ps [13].

3.1.3.2 Positronium molecules

With a more intense positron source, D. B. Cassidy and A. P; Mills [14] expected an increase of the Ps density to the point where many thousands of atoms interact and can undergo a phase transition to form a Bose–Einstein condensate. The interactions between Ps atoms have been studied by implanting intense positron pulses into a thin film of porous silica.

3.2 Conventional Experimental work

3.2.1 Positron sources

Positrons emitted during nuclear decay can be used in laboratories. Common sources are listed in Table 3.1. The stopping profiles of β^+- particles in solids decrease exponentially with increasing penetration depth z, $P(z) \sim exp(-z/z_0)$, where the typical mean penetration depths z_0 are of the order of 10-100 μm. Thus positrons from radioactive sources probe volume properties of matter.

Table 3.1 Positron sources commonly used

Nuclei	Half-life	β^+-decay (%)	Energy emitted (Max.) Mev
^{22}Na	2.62 y	91	0.545
^{55}Co	18.2 h	81	1.5
^{57}Ni	36.0 h	46	0.85
^{58}Co	71.3 d	15	0.475
^{64}Cu	12.80 h	19	0.656
^{90}Nb	14.6 h	54	1.5

From the table above, it is clear that ^{22}Na is the most convenient source because of its long half-life (2.62 year) and its high β^+ decay efficiency of 90.4 % (Figure 3.2). Positrons can be obtained from the β^+ -decay of radioactive isotopes, e.g. from ^{22}Na according to the decay reaction

$$^{22}Na \rightarrow {}^{22}Ne + \beta^+ + \nu_e + \gamma. \qquad (3.4)$$

The ^{22}Na isotope has other advantages. The very important one is the appearance of a 1.27 - MeV γ- quantum almost simultaneously with the positron, which enables positron lifetime measurement by a start–stop coincidence γ-spectrometer. Since the biological half-life for sodium is only a few days, the accidental contamination of laboratory personnel is less harmful. Moreover, the manufacture of laboratory sources is simple, due to the easy handling of different sodium salts in aqueous solution, such as sodium chloride or sodium acetate. Besides, a reasonable price makes this isotope the most common used source material in positron research. A simplified decay scheme is shown in Figure 3.2.

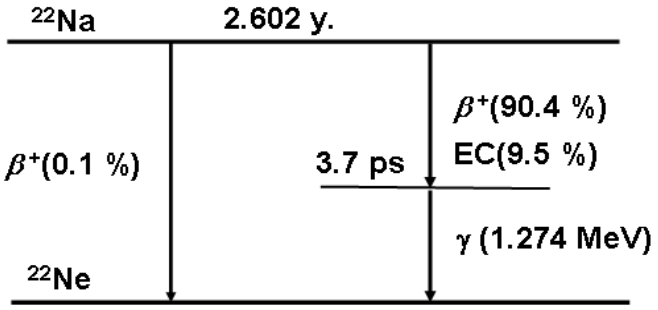

Figure 3.2 Decay scheme of the radioactive isotope ^{22}Na. 90.4 % of the isotope decays by emission of a positron and an electron neutrino to the excited state of ^{22}Ne. The ground state is reached after 3.7 ps by emission of a γ- quantum of 1.274 MeV. Competitive processes with lower probabilities are electron capture (EC) and direct transition to the Ne ground state.

3.2.1.1 The preparation of a source

The sources are prepared by evaporating a solution of a ^{22}Na salt on a thin metal or polymer foil e.g. Al, Ni and Kapton. Sources of weak activity (8×10^5 Bq which is 20 μCi) are used for conventional positron lifetime and Doppler-broadening measurements.

The positron beam and angular correlation techniques require much stronger sources. Source capsules of about 4 GBq (100 mCi) are required [15].
Another possibility for strong positron sources is to generate positrons by pair production [16]. In this case, an electron beam is stopped in an absorber of high atomic number creating bremsstrahlung γ-rays. Provided that the energy of the primary electron beam is high enough, the generation probability of electron–positron pairs is sufficiently high.

The source should be surrounded by two identical samples in order to ensure the almost complete annihilation of positrons in the specimen volume (Sandwich arrangement). When a positron is produced in the ^{22}Na source a 'start' signal (a

1274 keV photon) is generated that is detected in a scintillator-photomultiplier combination. When the positron annihilates a 'stop' signal (511 keV) is produced that is also detected with a nuclear scintillator detector. Energy selection is done in the constant fraction differential discriminators. Both signals are used in a time to amplitude convertor that generates a signal proportional to the lifetime of the positron. This signal is further processed by a multichannel analyzer.

3.2.1.2 Source correction

A small fraction of the positrons annihilates in the source. It is about 2 to 15% depending on the foil thickness and the atomic number of the sample, which determines the backscattering and, thus, the multiple passing of positrons through the source. In the positron lifetime spectra analysis, this fraction must be determined and subtracted [17].

3.2.2 Sample features

The samples should be flat and larger than the source. For the room temperature measurements, the sample size is almost unlimited but should not be less than the size of the source. In order to ensure that 99.99% of the positrons will stop and annihilate in the sample, a certain sample thickness is required. The positron implantation profiles have been studied by Brandt and Paulin [18].

The implantation profile of high-energy positrons emitted from a radioactive source into a solid can be described by an equation which states that the positron intensity I (z) decays as:

$$I(z) = I_0 \, e^{-\alpha_+ z} \qquad (3.5)$$

where, α_+ is the absorption coefficient.

They found out that the absorption coefficient is in a wide varity of materials given by:

$$\alpha_+ = R_+^{-1} = (16 \pm 1)\ \frac{[\mathrm{d\ g\ cm^{-3}}]}{\mathrm{E}_{\max}^{1.43}[MeV]}\ [\mathrm{cm^{-1}}] \qquad (3.6)$$

where, d is the sample mass density and E_{max} the maximum kinetic energy of emitted positrons. This approximation can be used for the determination of the minimal thickness of the samples. This is shown in Figure 3. 3.

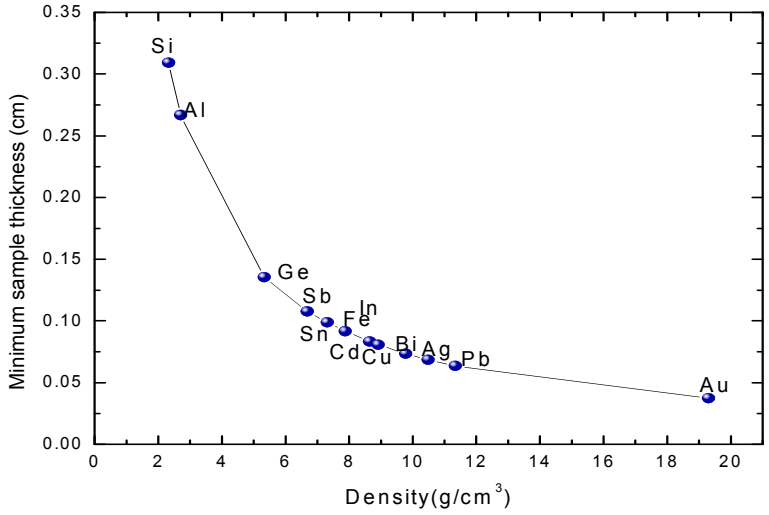

Figure 3.3 The relation between the mass density of the material used in positron annihilation lifetime measurements and the minimum thickness required from that material to stop 99% of positrons

In the case of temperature-dependent measurements, the samples should fit into the cryostats. Maximum size is therefore about 10 x 10 mm. If the samples are thinner, one can make a stack of several samples, or putting a reference sample with a known value of annihilation lifetime behind the sample under investigation.

3.2.3 Experimental techniques

There are different techniques of PAS:

1. Angular Correlation of Annihilation Radiation (ACAR).
2. Positron Annihilation Lifetime Spectroscopy (PALS).
3. Doppler Broadening of Annihilation Line (DBAR).
4. Age-Momentum Correlation (AMOC).
5. Positron Beams System (PBS).

The principles of the different positron techniques are illustrated in Figure 3.4. They are classified into two main groups which are distinguished by the sensitivity of positrons to the electron density (PALS) and to the electron linear momentum distribution in the material (DBAR and ACAR).

In this Ph. D study, three positron techniques were used:

1 PALS
2 Slow positron beam of Ghent University
3 In-situ measurements of the DBAR at the same time of the tensile test.

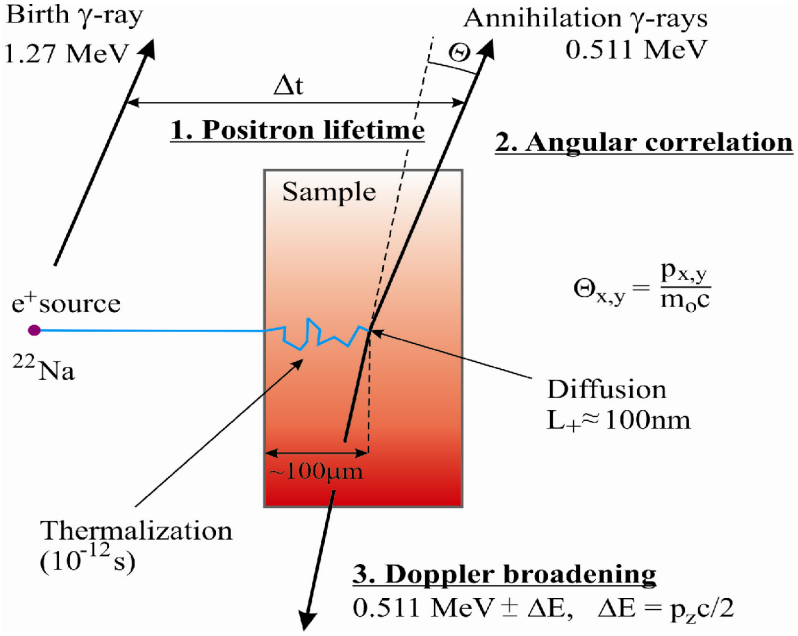

Figure 3.4 Scheme of different positron experiments

3.2.3.1 Positron Annihilation Lifetime Spectroscopy (PALS)

When energetic positrons are injected into a condensed medium they first slow down to thermal energies in a very short time of the order of 1ps. The positron is injected into the sample almost simultaneously with the emission of γ- ray of 1274 keV. Ages of individual positrons, can be measured as time differences between the emission of the birth γ- quantum and one of the annihilation photons. The mean implantation range varying between 10 to 1000 μm, which means that, the positrons reaches the bulk of the sample. After living in a thermal equilibrium, the positron annihilates with an electron from the surrounding medium mainly into two 511 keV gamma quanta. The average lifetime of positrons is characteristic of each material and varies from 100 to 500 ps [19].

The lifetime of positrons annihilated in metals or alloys is determined by the average density of electrons at the annihilation site. A reliable method is to measure the slope of the logarithm of the number of counts as a function of time

(the slope method). By this method, a few components of the lifetime of positrons can be differentiated. A typical system for measuring the lifetime of positrons is represented in Figure 3.5. ^{22}Na is the most commonly used positron source. The ^{22}Na nucleus emits a positron with a maximum energy of 0.544 MeV, and the nucleus transmutes to ^{22}Ne*(the excited state). The excited ^{22}Ne* emits a gamma ray (1.28 MeV) after a few picoseconds and changes to the ground state ^{22}Ne, therefore the birth time of positron is set to be the time when the 1.28 MeV gamma ray is detected. The time for the positron to annihilate is the time when the 0.511 MeV gamma rays are detected. The time interval between the 1.28 MeV pulse and the 0.511 MeV pulse is the age of the positron. The time interval is converted to a voltage pulse by charging a condenser with a constant current by a time to amplitude converter (TAC). This pulse is transferred to the multichannel analyzer for digitizing the time interval and storage. The pulse is only transferred by opening the linear gate when the two pulses detected by the detectors are within a certain time interval.

The positron annihilation rate is proportional to the electron density. When a positron gets trapped into an open volume defect, it sees a lower electron density than in a free or delocalized Bloch-like state. The positron annihilation lifetime in the bulk material is shorter than the one for trapped positrons in defects. Thus positron lifetimes gives information on the annihilation sites. PALS is used to distinguish between the different types of defects [20].

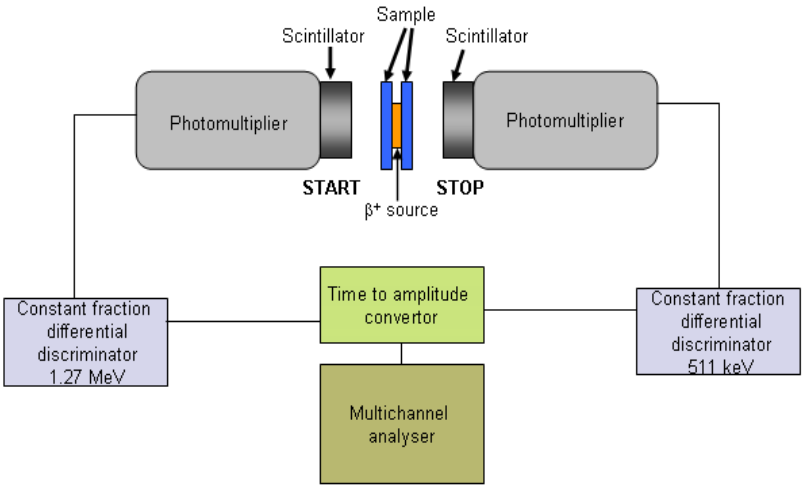

Figure 3.5 The experimental set-ups for the measurement of the positron annihilation lifetime.

3.2.3.2 Doppler-broadening of the annihilation radiation spectroscopy (DBAR)

The positron source is attached to tensile sample. A Ge detector with an energy resolution of 1.24 keV at 514 keV is used to record the γ – ray spectra. The shape of the Doppler broadened annihilation γ ray spectrum contains detailed information on the linear momentum distribution of the annihilating electrons. It was proposed to characterize the Doppler broadened annihilation line by introducing the so-called ***S***hape and ***W***ing parameter (***S, W***). The *S* parameter is defined as the area of the central low-momentum part of the spectrum, *C*, divided by the total area below the annihilation peak, (***A+B+C+D+E)*** after background subtraction.

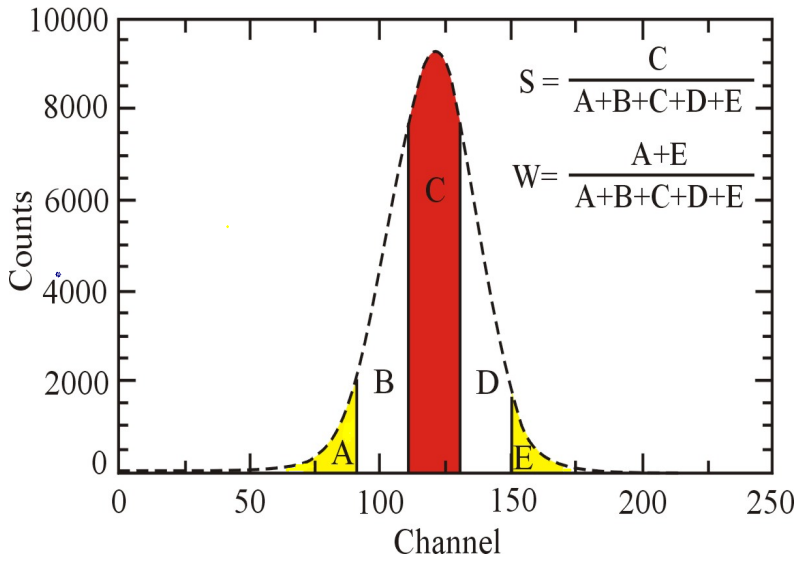

Figure 3.6 Schematic representation of the calculation of the *S* and *W* parameters. The *S* parameter is the area of the central low-momentum part of the spectrum, *C*, divided by the total area below the annihilation peak, *(A+B+C+D+E)* after background subtraction, while the *W* parameter is area of the two wings *(A+E)* divided by the total area below the annihilation peak, *(A+B+C+D+E)*.

The *W* parameter is defined as the area of the two wings for (the high momentum regions which is far from the center); *(A+E)* divided by the total area below the annihilation peak, *(A+B+C+D+E)*. The calculation of the S and W parameters is illustrated in Figure 3.6

$$S = C/(A+B+C+D+E), \quad W = (A+E)/(A+B+C+D+E) \tag{3.7}$$

The integer *C* expresses the number of counts in a symmetrically located central region of the annihilation line and *(A+B+C+D+E)* is the integral number of counts under the whole curve. The boundaries of the integral *C* are chosen so that *S'* equal to 0.5 in the well-annealed Fe sample. The physical relevance of the *S* parameter is based on the linear momentum difference between valence and

core electrons. The core electrons localized in the ion core have a much higher linear momentum than the valence electrons. Owing to the locally reduced density of core electrons in vacancy-like defects such as vacancies, vacancy clusters or lattice dilatations, positron traps exhibit a lower density of electrons with high linear momentum. Thus, the probability of positron annihilation with a low-linear momentum valence electron is increased compared to the situation in the perfect lattice. This causes an increased number of counts in ***C***, i.e., with small Doppler shifts of the annihilation energy. Consequently, the *S* parameter is larger in a specimen containing vacancy-like defects than in a defect-free material. Usually, the S parameter is measured for a series of samples as a function of the implantation energy, temperature or other extrinsic parameter in an attempt to correlate the line-shape parameter behavior to some physical characteristics such as variations in defect concentrations.

Trapping of positrons in vacancy type defects tends to increase the S parameter value. Positrons that trap at such defects have a lower probability of annihilating with high-linear momentum core electrons than they do while freely diffusing. These parameters have no direct physical meaning and cannot be compared in an absolute way because of the specific detector resolution and choice of the intervals for the integration. That is why; they are only used to be compared to reference materials parameters. In depth resolving measurements, it is common to normalize the parameters to the bulk values of the sample material, described as S_b and W_b.

S and *W* are sensitive to the concentration and type of the defect because they are a combination of bulk and defect broadening effects. The defect concentration can be calculated if the defect-specific parameters S_d and W_d are known. Another parameter *R* can be introduced which is defect-type dependent, but not concentration dependent [21]. *R* is defined as follows:

$$R = \left| \frac{S - S_b}{W - W_b} \right| = \left| \frac{S_d - S_b}{W_d - W_b} \right| \qquad (3.8)$$

S-versus-W plots give also information about the types of defects that exist. If there is only one type of defect, the S- W relation will be linear and if there are more than one type of defect, there will be more than one straight line.

3.2.3.3 Angular Correlation of Annihilation Radiation (ACAR)

The principle for the measurement of the angular correlation of annihilation radiation is illustrated in Figure 3.7. The linear momentum component of the annihilating electron perpendicular to the propagation direction of the γ -photons results in an angle deviation. This transversal component of the electron linear momentum could be measured by analyzing the deviation θ from exact anti co linearity. A simple position sensitive detection can be used in one dimension by a mechanical movement of a long scintillation detector with lead slits allowing for angular resolution [22].

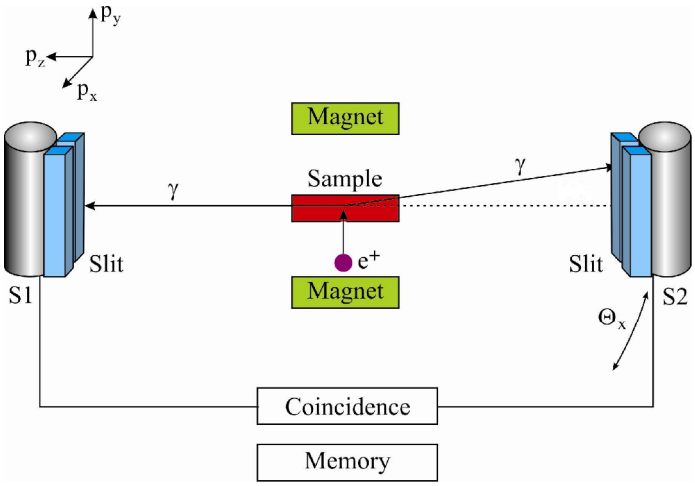

Figure 3.7 The experimental setup for the measurement of one-dimensional angular correlation of annihilation radiation with a long-slit geometry. Sodium iodide crystals are used as scintillation detectors (S_1 and S_2) in the y direction. The left arm with detector and the lead collimators is fixed, while, the right arm can be the angle Θ_x.

The sample-detector distance and the slit size determine the angular resolution. A resolution of 1 mrad corresponds to 250 eV for an energy detecting system, which is much better than a good Ge-detector (1.1 keV). Current angular correlation systems even have resolutions smaller then 1 mrad. Therefore, ACAR is mainly applied in the study of the electron structure of bulk material or defects. In order to minimize the reduction of the counting rate due to the distance of several mm between sample and source, a strong magnetic field of about 1 T is usually applied to guide the positrons to the sample.

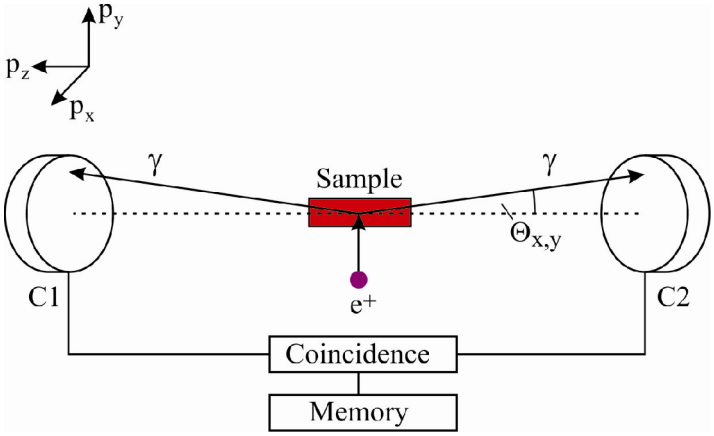

Figure 3.8 Schematic drawing of a 2D angular correlation setup.

The momentum distribution can also be recorded in two dimensions using a detector with two dimensional arrays [22]. The sample-to-detector distance amounts typically to several metres so that γ quanta from only a small solid angle are detected. The angular resolution can be adjusted in the range of 0.2 to 5 mrad [23]. The resolution of such a system is 0.2 mrad x 0.2 mrad. To collect a 2D-ACAR spectrum, several days will be needed, which is the main disadvantage of the 2D-ACAR method which is illustrated in Figure 3.8.

3.2.4 Positron Beams System (PBS)

The main advantage of the conventional sample–source sandwich arrangement is that the emitted positrons immediately penetrate the bulk sample. But in order to obtain a defined small penetration depth or to study the sample surface, mono-energetic positrons (slow positrons) that can be accelerated to defined energies

by simple linear electric field are necessary. Such setups are called slow-positron-beam techniques. They are also called variable energy positron annihilation spectroscopy (VEPAS).

Monitoring of defects as a function of depth (defect depth profiling) is possible by adjusting the positron energy in a range of a few eV to several tens of keV. The mono-energetic positrons are obtained by moderation. Only a small fraction of less than 1 % of incident positrons undergoes this moderation process. The rest of the positrons (unmoderated positrons) must be separated from the beam of mono-energetic positrons that is used for defect experiments after defined acceleration. The moderation and acceleration requires the spatial separation of the source and the sample, and thus a beam guidance system must be used.

In order to obtain the defect depth profile from the measured variation of annihilation parameters as a function of the incident positron energy, knowledge of the positron implantation profile is required. This will be treated in a separate part of this chapter where the depth profiling with slow positrons will be explained.

3.3 Depth profiling with slow positrons

3.3.1 Overview of slow positron beam interactions

The ability of positrons to be effectively used for depth profiling studies is connected with a detailed knowledge of the interaction of positrons with solids and solid surfaces. A survey of the possible various interactions that can occur when a beam of mono-energetic positrons collides with a solid is represented in Figure 3.9. Some of these incident positrons impinging on the surface will be scattered elastically and the rest of the beam penetrates the solid and rapidly slow down to near thermal energies by transferring their energy to the lattice of the material. A fraction of these positrons reach back to the surface before being thermalized. At the surface these positrons may either be emitted directly as epi-thermal positrons or form positronium at the surface and escape the material as

epi-thermal ('hot') positronium. A small fraction of the positrons may even annihilate inside the material without being fully thermalized.

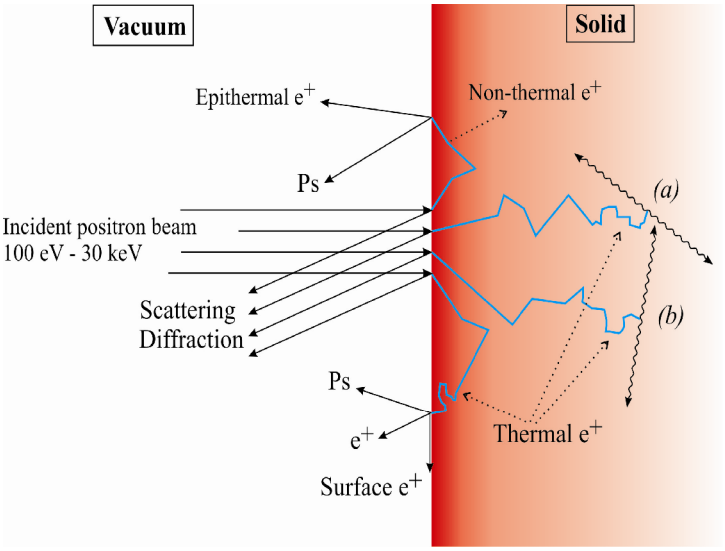

Figure 3.9 Schematic representation of slow positron beam interactions

The positrons which have become thermal inside the material and can be considered as the dominating part also have different fates. After the fast thermalization process (10 ps) the positron diffuses through the material. Now there are three main possibilities:

1- The thermalized positron may remain in a delocalized (Bloch) state and diffuse around until it annihilates with an electron in the material due to the overlap of its wave function with the electron wave function.
2- The positron may annihilate due to the trapping into a defect, its wave function becoming strongly localized and annihilate in its trapped state.
3- The free positrons may diffuse back to the surface, where it either traps in a two dimensional surface state or a near-surface defect, or is emitted as a free positrons, or is emitted while forming a free positronium atom.

Some of these processes will be explained in more detail in the next paragraphs.

3.3.1.1 Moderation

Moderators can be subdivided in two types of setup: transmission and reflection. In the transmission setup a thin moderator foil, with a thickness smaller than the positron diffusion length, is mounted in front of the primary positron beam, producing moderated positrons at the other side. In a reflection setup, the moderated positrons are produced at the same side of the primary beam.

Materials with negative positron work functions can act as moderator for energetic positrons with a broad energy distribution. In order to leave the material through a surface, a positron must gain energy Φ_+, the so called work function. This energy is defined as the minimum energy required for moving a positron from a point inside to one just outside the surface. The work function is the combination of the surface barrier D and the positron chemical potential μ_+.

$$\Phi_+ = D - \mu_+ \qquad (3.9)$$

The surface dipole barrier D is primarily caused by the tailing of the electron distribution in the vacuum. The positron chemical potential (μ_+) is the difference between the bottom of the lowest positron band and the average potential over the interstitial regions between the atoms. It is mainly the effect of D which is negative for positrons that causes the work function Φ_+ to be sometimes negative. This allows the emission of slow mono-energetic positrons into the vacuum.

The potential energy diagram of a thermalized positron near the surface is represented in Figure 3.10. The attractive potential well is a combination of image forces at large distances and interactions with the low-density electron gas near the surface. Positrons can annihilate in this surface state or get out of the potential well because of thermal desorption. At low temperatures, trapping in the surface states or in surface defects increases. In some cases positrons approaching the surface are reflected due to the potential step at the surface.

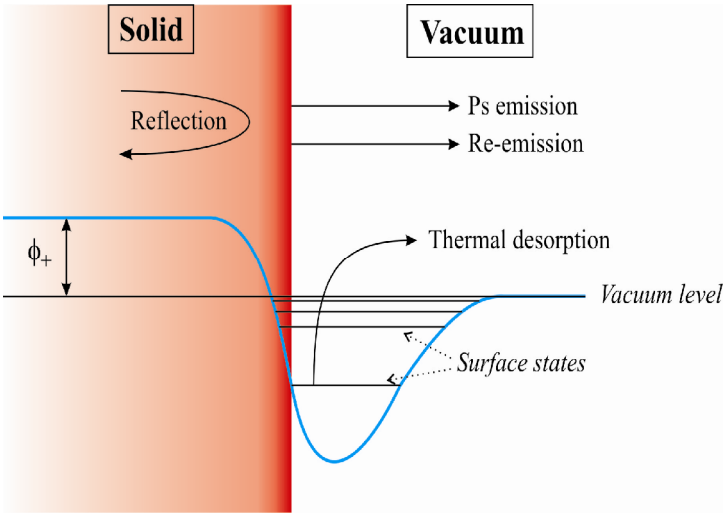

Figure 3.10 Different interaction mechanisms for positrons reaching the material surface. In this case the positron work function is negative.

The moderation is based on the fact that a negative positron work function Φ_+ exists for many solids. In most cases, transmission geometry with a thin moderator foil placed directly in front of the source capsule is used. The thickness of the foil is much smaller than the mean penetration depth and, therefore, only a small fraction of positrons thermalizes and starts to diffuse there. If the surface is reached during the diffusion, the positrons are spontaneously emitted from the moderator foil with a kinetic energy equal to the thermally broadened work function Φ_+.

Materials with high atomic numbers are favorable for moderation, because the ratio of the mean diffusion length to the thermalization distance is larger. A suitable material is a single-crystal tungsten foil in a (100) orientation with a thickness of a few μm or a (110) tungsten single crystal for application in backscattering geometry. Since the positrons may be trapped in defects during their diffusion to the surface, a foil containing only a small number of positron traps must be prepared by annealing. The work function of a (110)-oriented

tungsten single crystal was measured to be $\Phi_+ = -3.0$ eV and a moderation efficiency of 3×10^{-3} could be achieved [24]. The moderation efficiency is given as the ratio of the number of moderated slow positrons to the total number of incident positrons.

Recently solid state rare-gas moderators, obtained by deposition of neon, argon or krypton on a carrier foil (on the surface capsule) at low temperatures have been used. These moderators have the highest efficiency due to their long diffusion length. They have the efficiency of 10^{-2}.

3.3.1.2 Implantation

In case of using a conventional source without moderation, the positrons are implanted very deep into the sample. See the implantation profile in paragraph 3.2.2.

In case of using a mono-energetic slow positron beam, positrons can be implanted close to the surface and the implantation profile is completely different. The implantation profile *P (E, z)* as a function of depth z for monoenegetic positrons having an energy E is given as:

$$P(E,z) = \frac{mz^{m-1}}{z_0^m}\exp\left[-\left(\frac{z}{z_0}\right)^m\right] \qquad (3.10)$$

The penetration parameter z_0 is described by:

$$z_0 = \frac{\alpha E^n}{\rho\Gamma\left(\frac{m+1}{m}\right)} \qquad (3.11)$$

The implantation profile is called a Makhov profile, after Makhov's original electron implantation experiments [25]. Where *m*, *r*, and *A* are empirical parameters. ρ is the mass density of the sample and Γ the gamma function.

Widely used empirical values are: A = 4.0 μgcm^{-2} keV^{-r}, m = 2 and r = 1.6 (Vehanen et al. 1987).

The mean penetration depth is given as:

$$\bar{z} = AE^{r}/\rho \qquad (3.12)$$

3.3.1.3 Positron diffusion

After thermalization the positron starts to diffuse through the solid. Because the positron has a positive charge, it is repelled by the nuclei and attracted by the surrounding electrons. In a periodic lattice the ion cores produce a periodic potential with minima at the lattice positions, resulting in a Bloch-like positron wave function. The De Broglie wavelength λ_{th} at a temperature T has a value that is an order of magnitude larger than the typical lattice parameter and is given by [26]

$$\lambda_{th} = \frac{2\pi\bar{h}}{\sqrt{3m_p k_B T}} \approx 6.2\sqrt{\frac{300}{T}}(nm) \qquad (3.3)$$

with m_p the rest mass of the positron and k_B the Boltzmann constant

(1.38x10^{-23} J/K).

The position probability density increases in interstitial regions. In analogy to electrons, diffusion of positrons is described with a semi-classical three-dimensional random-walk theory [27]. Scattering mechanisms determine the positron mean free path $\langle l \rangle$

$$\langle I \rangle = \frac{3D_{+}}{\sqrt{\frac{3k_B T}{m_*}}} \qquad (3.14)$$

$\langle l \rangle$ is a function of temperature T, with D_+ the positron diffusion coefficient and m_* the effective positron mass. The positron diffusion coefficient is related to the mobility μ by the Einstein equation:

$$eD_{+} = k_B T\mu \qquad (3.15)$$

with e the elementary charge (1.60×10^{-19} C).

Phonon scattering is the main determining process for the positron diffusion. For semiconductor materials and a lot of metals scattering occurs by longitudinal acoustic phonons. This results in a temperature-dependent diffusion coefficient $D_+ \propto T^{1/2}$, as was shown for silicon [28].

The positron diffusion length L_+ is related to the positron diffusion coefficient and limited due to the finite lifetime of positrons. In defect-free bulk material this leads to:

$$L_+ = \sqrt{\tau_b D_+} = \sqrt{\tau_b \frac{\tau_r k_B T}{m_*}} \tag{3.16}$$

The relaxation time for the dominant scattering mechanism is τ_r and τ_b is the lifetime of the positrons in the defect-free bulk. The "effective" positron mass m_* is 1.3 to 1.7 times larger than the rest mass of the positrons, due to three contributions [29]. The most important is phonon scattering: the positron linear momentum distribution broadens due to phonon absorption by the low-energy positron. The other contributions are the effect of the electron density enhancement in the vicinity of the positive particle and the effect of the periodic lattice. Diffusion lengths are of the order of 100 nm, which is small compared to the implantation depth.

The Doppler-broadening VEP-beam experiments give depth-resolved and time-independent information. Thus, all processes to which thermal positrons are subjected, such as diffusion, drift, trapping at defects or free annihilation, can be combined in a single one-dimensional equation. This steady-state positron diffusion equation can be written as:

$$D_+ \frac{d^2}{dz^2} c(z) - \frac{d}{dz}\left[v_d(z) c(z)\right] - \lambda_{eff} c(z) + I(E,z) = 0 \tag{3.17}$$

Here, *c (z)* is the steady-state positron density as a function of depth *z, I (E, z)* the positron implantation rate and ν_d the positron drift velocity depending on the local electric field strength E (z):

$$\nu_d = \mu_+ E(z) \tag{3.18}$$

In the diffusion equation the positron trapping into defects is taken into account and this leads to an effective annihilation rate λ_{eff}:

$$\lambda_{eff} = \frac{1}{\tau_b} + k(z) \tag{3.19}$$

Next to the bulk annihilations, represented by τ_b , positrons are trapped into defects with a rate $\kappa(z)$, which is a function of specific positron trapping rate for defects , and the defect concentration $n_t(z)$:

$$\kappa(z) = \nu_t n_t(z) \tag{3.20}$$

In some materials different specific positron trapping rates can be associated with typical defect types like mono-vacancies and dislocations [30].

The effective diffusion length L_{eff} is influenced by electric fields and crystal defects and this leads to:

$$L_{eff} = \left[\sqrt{\frac{\lambda_{eff}}{D_+} + \left(\frac{eE}{2k_B T} \right)^2} - \frac{e|E|}{2k_B T} \right]^{-1} \tag{3.21}$$

Positron traps are taken into account by λ_{eff} and cause a decrease in effective diffusion length. The electric field strength E provides an increase of the effective diffusion length.

3.3.2 Data analysis of positron beam experiments

There are several measurement parameters that can be analyzed using the differential equation 3.16. Solving this diffusion equation leads to the determination of depth profiles. By varying the implantation energy of the positron beam, one can analyze a material in depth using positron annihilation spectroscopy. The most common method is depth selective DBAR. The results

are often presented as the Doppler line-shape parameter S in function of the implantation energy or sometimes the mean implantation depth.

3.3.2.1 Analysis of the depth resolved data

VEPFIT

VEPFIT [31] is a very important program for the analysis of depth resolved Doppler broadening data. The model is based on describing the sample by a set of layers with different characteristics such as S-parameter (or W-parameter), positron diffusion length, layer thickness or a build-in electric field. These properties can carry information about the material and the defect concentration in the respective layers. Also Gaussian defect profiles can be implemented.

3.4 Positron annihilation lifetime spectroscopy data

The calculated and measured positron lifetimes for different types of defects in pure iron and other iron based alloys are summarized in Table 3.2. This table contains data for the positron annihilation lifetime measured and calculated in Gent University and compared with other data done by others.

We have measured the value for defect free Fe, FeMnSiCrNi and FeSi. The values of the defect free lifetimes for those materials varied between 107-110 ps.

Table 3.2 The calculated and measured positron lifetimes for different types of defects in pure iron and other iron based alloys

Material	Positron lifetime (ps)	Reference	Measured in Gent (ps)
Fe-bulk	110	[32]	107
Fe-dislocations	165	[33]	150-165
Fe-mono-vacancy	175	[32]	
Fe-di-vacancy	197	[33]	
Fe-3 vacancy cluster	232	[33]	
Fe-4 vacancy cluster	262	[33]	
Fe-6 vacancy cluster	304	[33]	
FeSi (2,3 and 4 wt.% Si well annealed)			108±3
$Fe_{75}Si_{25}$	109	[34]	
FeMnSiCrNi(C)			107±3

3.5 Instrumental methods

3.5.1 Positron annihilation spectroscopy

1. The Doppler broadening (DB) of the 511 keV annihilation line is measured for the bulk material using a high purity germanium detector with a resolution of 1.2 keV at the 514 keV line of ^{85}Sr [35]. The results are analyzed in terms of the so-called S and W parameters.

The slow positron beam of Gent University, which is fully described in [35], is used to study the FeMnSiCrNi(C) and the FeSi samples. The energy of the magnetically guided positron beam is variable between 0.1 and 30 keV and the resolution of the high purity Ge detector is 1.2 keV at 514 keV.

2. Positron lifetime measurements were performed at room temperature using a fast-fast lifetime spectrometer. Each spectrum contained more than 10^6 counts and several spectra were accumulated for each measuring point in order to ensure the reproducibility of the data. The lifetime spectrum was analyzed with the LT program by Kansy [36] using a single Gaussian resolution function with a FWHM = 200 ps, while the source contribution was 14 % with a single lifetime of 384 ps.

As a positron source ^{22}NaCl of about 10 μCi was sealed between two kapton foils with a thickness of 7.5 μm. This source is surrounded by two identical samples in the so-called sandwich configuration [37]. The resolution of the setup is 200 ps, while the source contribution was 14 % with a single lifetime of 384ps.

3.5.2 Light optical Microscopy (LOM)

The FeMnSiCrNi(C) samples examined by the LOM were mechanichally polished and then electro-polished by means of a LectroPol-5 set up. The electrolyte used is a solution of 20% perchliric acid and 80% butylcellosolve. The electrotical polishing is important to eliminate the ε martensite formed on the surface as a result of the mechanical polishing of the samples. The effect of polishing was examined by the slow positron beam. The time of polishing and the pressure used in polishing the samples affect the surface. Afterwards, the specimens were color etched in an aqueous solution of 1.2% $K_2S_2O_5$ and 0.5% NH_4HF_2. Each phase could clearly be distinguished on the basis of their color and morphology [38]. The microstructure was investigated on a Zeiss Jenavert optical microscope.

3.5.3 XRD

X- Ray diffraction (XRD) is used in the study to identify the different phases in the FeMnSiCrNi(C) samples. A Siemens D5000 diffractometer with a Mo K_α (λ=0.7071nm) radiation and operating with an intensity of 50 Ma and a voltage of 45 V was used.

3.6 References

[1] R. Beringer, C. G. Montgomery. Phys. Rev.61, (1942) p.222.

[2] S. De Benedetti and H. J. Richings, Rev. Sci. Instr. 23 (1952) p.37.

[3] P. A. M. Dirac A theory of electrons and protons. Proc. Roy. Soc. Lond. A. 126 (1930) p.360.

[4] S. Mohorivicic. Moglichkeit neuer Elemente und ihre bedeutung fur die Astrophysik. Aston. Nachr., 253 (1934) p.93.

[5] A. Ruark Phys. Rev. 68 (1945) p.278.

[6] A. I. Akhiezer and V.B Berestetskii. Quantum Electrodynamics, Wiley, New York (1965).

[7] R. M. Nieminen, J. Oliva., Theory of positronium formation and positron emission at metal surfaces; Phys. Rev. B., 22 (1980) p.2226.

[8] O. E. Mogensen: Positron annihilation in chemistry. Springer-Verlag, Berlin (1995)

[9] A. Ore. Annihilation of positrons in gases. Naturitenskapelig Rekke, 9 (1949) p.1

[10] R. A. Ferrell, Phys. Rev. 110 (1958) p.1355.

[11] O. E Mogensen, J. Chem. Phys.60 (1974) p.998.

[12] V. M. Byakov and S. V. Stepanov, J. Radioanal. Nucl. Chem.,210, (1996) p.371.

[13] C. Dauwe, B. Van Waeyenberge, and N. Balcaen, Phys. Rev. B 68, (2003) p.132202.

[14] D. B. Cassidy and A.P. Mills Jr., Nature 449 (2007) p. 195.

[15] H. Huomo, R. Jones, J. Hurst, A. Vehanen, J. Throwe, S.G. Usmar and K. G. Lynn. Nucl. Instr. Meth. Phys. Res. A284, (1989) p.359.

[16] P. J Schultz, E. Tandberg, K. G. Lynn,. B. Nielsen, T. E. Jackman,, M. W. Denhoff, G. C. Aers, Phys. Rev. Lett. 61, (1988) p.187

[17] T. E. M. Staab, B. Somieski, and R. Krause-Rehberg, Nucl. Instrum. Methods Phys. Res. A381, (1996) p.141.

[18] W. Brandt, R. Paulin: Phys. Rev. B 15 (1977) p.2511.

[19] P. Hautojarvi, and A.Vehanen, A. Dupasquier, M.J. Manninen, P. E. Mijnarends, R. M. Nieminen, R.N. West, Positrons in Solid, Springer-Verlag, 1-23 (1979).

[20] P. Hautojärvi and C. Corbel, “Positron spectroscopy of solids” (lOP) (1995) p.491.

[21] S. Mantl, W. Triftshauser; Phys. Rev. B 17 (1978) p.1645.

[22] R. Krause-Rehberg, H. S. Leipner, Positron Annihilation in Semiconductors, Springer Verlag, Berlin (1999).

[23] S. Berko Positrons Solid-State Physics, Proc. International School of Physics «Enrico Fermi», Course LXXXIII, Varenna 1981, North-Holland, Amsterdam (1983) p. 64.

[24] A. Vehanen, K. G. Lynn, P. J. Schutz, M. Eldrup; Appl. Physics A 32, (1983) p.163.

[25] A. F. Makhov. J. Sov. Phys. Sol. State2, (1961) p.1934.

[26] P. J Schultz, C.L. Snead; Metallurgical Trans. A. 21A, (1990) p.1121.

[27] M. J. Puska, R. M. Nieminen, Rev. Mod. Phys. 66, (1994) p.841.

[28] E. Soininen, H. Huomo, P. A. Huttunen, J. Mãkinen, P. Hautojarvi, A. Vehanen; Phys. Rev. B 41, (1990) p.6227.

[29] P. J. Shultz, K. G. Lynn, Rev. Mod. Phys. 60, (1988) p.701

[30] R. M. Nieminen, M. J. Manninen; “Positrons in solids” (ed. P. Hautojarvi) Springer-Verlag, Berlin (1979).

[31] A. Van Veen, H. Schut, J. De Vries, I. Hakvroort and M.R. Jpma, Analysis of positron profiling data by means of VEPFIT, Am. Inst. Phys. Conf. Proc. 218, (1990) p.171.

[32] P. Hautojarvi, L. Pollanen, A. Vehanen, J. Yli-Kauppila, J. Nucl. Mater.114, (1983) p.250

[33] A. Vehanen, P. Hautojarvi, J. Johansson, J. Yli-Kauppila, P. Moser, Phys. Rev.B 25, (1982) p.762

[34] E.A. Kummerle, K. Badura, B. Sepiol, H. Mehrer, and H. E. Schaefer, Phys. Rev. B 52, (1995) p.6947.

[35] J. De Baerdemaeker, J. Colaux, G. Terwagne, C. Dauwe, J. Rad. Phys. Chem. 68, (2003) p.605.

[36] J. Kansy, Nucl. Instr.and Meth., 374, (1996) p.235.

[37] D. Segers, S. Van Petegem, J. F. Loffler, H. Van Swygenhven, W. Wagner, C. Dauwe. J. Nano-Structured Materials, 12, (1999) p.1059.

[38] Qing Gu,"Martensitic Transformation and Shape Memory effect in FeMnSi based Shape Memory Alloys", 1994, Doctoral dissertation, Katholieke Universiteit Leuven, Belgium.

Chapter 4

Effect of annealing of deformed Iron

In this chapter the isochronal annealing effect on deformed iron samples is studied using the positron annihilation lifetime (PAL) and the Doppler broadening of the annihilation radiation (DBAR) techniques to figure out the effect of the sample compositions on the annealing temperature. In the first section the positron annihilation lifetimes of the pure and the commercial Fe (less pure iron), which were deformed and annealed isochronically were investigated. In the second section, the data for the bulk S parameter for the less pure Fe is presented against the annealing temperature. Undeformed Fe with purity of (99.99%) was used as a reference material to compare it with the commercial Fe used.

4.1 Introduction

The positron annihilation lifetime spectroscopy (PALS) can quantify the size of open volume defects, as well as the defect concentration, and is based on the precise measurement of the lifetime of a positron in a solid. The concentration is deduced from the fraction of positrons that annihilate from a trapped state. The defect size is directly related to the value of the position lifetime; the larger the defect, the lower the local electron density and consequently the longer the positron lifetime will be [1].

Values of the lifetime of positrons trapped in dislocations are close or slightly below the vacancy lifetime [2, 3]. For this reason, one can say that the positron lifetime may be related to vacancies trapped in the stress field around a dislocation line or in vacancies on a dislocation line which would be equivalent to a pair of monoatomic jogs [4]. Hidalgo et al. [5] measured the positron

lifetime in deformed iron to be 150 ps. They suggested that positrons annihilate at associated defects (vacancies or jogs) rather than at the dislocation line. Park et al. [6] have studied the effectiveness of trapping by edge and screw dislocations, and the ability to determine the number of dislocations of each type per unit area.

Calculation of positron lifetimes in jogs and vacancies on an edge dislocation line in Fe was done by Yasushi Kamimura et al. [7]. They concluded that the positron annihilation lifetime in the edge-dislocation is 117 ps, which is almost the same value for the positron lifetime in the jog. The positron lifetime in the associated vacancy in dislocation is 140 ps.

DBAR is based on the measurement of the linear momentum of the annihilating electron - positron pair. The photons created during the electron - positron annihilation are detected by a germanium detector. The shape of the resulting photo-peak reflects the momentum distribution of the original electron - positron pair. This distribution is determined by the momentum distribution of the electrons seen by the positron. This is influenced by the size and the nature of the defects. Measurements of the Doppler broadening of positron - electron annihilation radiation are generally characterized by the S (Shape) parameter, defined as the ratio between the content of the central part of the annihilation spectra and the content of the total spectra. This parameter reflects the positron annihilation with valence electrons (low momentum). In general, a high value of S indicates positron annihilation in open volume defects. A second useful parameter for the analysis of DBAR is the W (Wing) parameter, which reflects the positron annihilation with high momentum electrons (core electrons). It is defined as the ratio of counts in two side windows and the total number of counts in the annihilation line.

4.1.1 Deformation induced defects

The plastic deformation of metals and alloys produces changes in the density and distribution of defects. In plastic deformed metals and alloys, the positrons are

captured by dislocations and vacancies. In polycrystalline samples, the deformation becomes complex due to the various interactions between dislocations and grain boundaries [2- 4]. It is known that deformation of metals such as rolling induces many defects [8]. Plastic deformation of metals occurs by the generation and movement of dislocations, which stores a small amount of energy in the form of the elastically distorted region along each dislocation line. Dislocations accumulating during deformation gather together first as tangled groups, then as tangled networks defining 'cells' with slight orientation differences [9- 11].

4.1.2 Isochronal annealing effect

The microstructural changes due to annealing of deformed metals are commonly described in terms of recovery and recrystallization. Upon annealing, the microstructural rearrangements depending on the amount of deformation, where in case of metals deformed to small strains, the dislocations rearrange themselves into boundaries and eventually into a fully developed sub-grain structure. In metals deformed to large strains the softening reaction prior to the onset of recrystallization appears to be controlled by sub-grain growth.

Less pure iron is much more resistant to recrystallization. The interstitial elements in a very low concentration have a profound effect on recovery processes. In particular, interstitial elements are associated with retardation of recovery [12- 13]. Snead et al. [14] and MacKenzie [15] have investigated the recovery of deformed iron using the positron annihilation technique. Both works were on Fe containing a noticeable amount of carbon. They concluded that trapping would be due to vacancies produced during plastic deformation and only minor contribution was attributed to dislocations. Hautojarvi et al. [16] have studied deformed iron of 99.998 % purity and commercial Fe of 99.86 % purity. They concluded that the traps of positrons in both types of deformed iron samples are dislocations. The results are shown in Figure 4.1

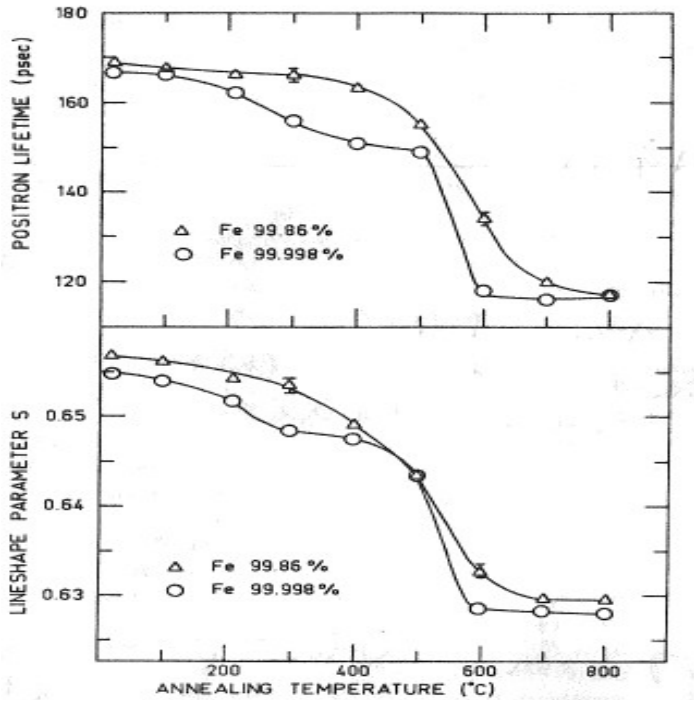

Figure 4.1 the recovery of the positron lifetime and annihilation the line-shape parameter in the two deformed iron samples with different purity as a function of Isochronal (1h) annealing temperature [this Figure is a copy from reference 16].

4.2 Experimental

In this work, the effect of annealing of less pure iron samples (with purity of 99.7%) is studied. The samples were cold- rolled at room temperature to a thickness reduction of 75%. A high pure Fe sample (with purity of 99.998%) was measured as a defect free reference sample.

The chemical composition of the less pure iron samples was determined with a Spectro LAVWA18A spectrometer of Spectro Analytical Instruments. The main impurities were Al (0.056 wt. %), Nb (0.03 wt. %), Si (0.008 wt. %), (Cr, Mo and Ni) all with 0.005 wt. % and C (0.002 wt. %). The Doppler broadening (DB)

of the 511 keV annihilation line was measured and the results were analyzed in terms of the so-called S and W parameters. Positron lifetime measurements were performed at room temperature using a fast-fast lifetime spectrometer. Each spectrum contained more than 10^6 counts and several spectra were accumulated for each measuring point in order to ensure the reproducibility of the data.

After deformation the less pure samples were annealed at 100°C (one hour) in boiling distilled water, and at 200-1000°C in a vacuum furnace in steps of 100°C. The samples were cooled in furnace. The DBAR and the positron lifetime measurements were preformed at room temperature after each annealing step for the pure iron samples.

4.3 Results and discussion

4.3.1 Positron annihilation lifetime spectroscopy (PALS)

The positron annihilation lifetime measured for the pure undeformed Fe sample was 107 ± 3 ps, and used as a reference material. Deformed less pure iron samples were annealed isochronally in the temperature range (23-1000°C). Figure 4.2 shows the temperature dependence of the positron annihilation mean lifetime τ_{mean} (which is calculated using equation 4.1) of the highly deformed less pure iron samples during the annealing. The samples were full of defects due to the high degree of deformation (cold rolled to thickness reduction of 75%). The positron annihilation mean lifetime in the temperature range from 20°C – 400°C was around 150 ps. It was slightly decreasing with the increase of the annealing temperature. This effect is due to the start of recovery

In the temperature range from 400°C to 700°C defects anneal out and the material is partially recrystallized. The mean lifetime decreases significantly and reaches a value of around 107 ps after annealing at 700°C, leading to the conclusion that the material is fully recrystallized. Hautojarvi et al. [16] reported on a positron annihilation study of pure deformed Fe (99.998 %) and compared it with less pure deformed Fe (99.86 %) (see Figure 4.1). It was shown that the

temperature range for the recrystallization of deformed very pure Fe is 300-600°C. The start of recrystallization at 300°C is a result of the rearrangement process of the dislocations. Comparing the two recrystallization ranges for our less pure iron samples and the pure iron samples of Hautojaravi, one can conclude that in the less pure iron the annealing out of defects starts at a higher temperature. This might be related to the higher impurity content of the samples. A possible explanation could be the pinning of dislocations by interstitial atoms such as carbon [16].

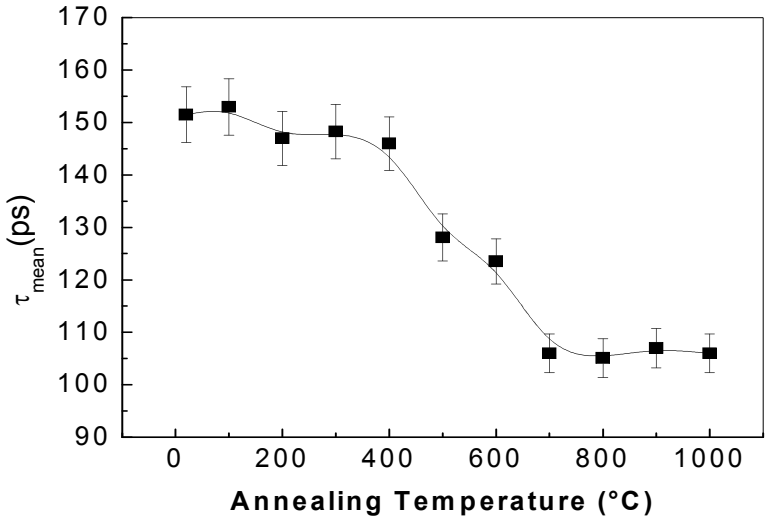

Figure 4.2 The relation between the annealing temperature and the positron annihilation mean lifetime for the less pure Fe samples (cold-rolled at room temperature to a thickness reduction of 75%).

The defect concentration and trapping rates were quantitatively calculated using the two state trapping model. The measured values for the positron annihilation lifetimes (τ_1, τ_2) and their intensities (I_1, I_2) were used to calculate the mean positron annihilation lifetime using the following relation:

$$\tau_{mean} = (\tau_1 I_1 + \tau_2 I_2) \quad (4.1)$$

The positron trapping rate for defects κ, can be calculated as:

$$\kappa = \mu_d C_d = \frac{I_2}{I_1} (\lambda_b - \lambda_d) \quad (4.2)$$

$$\tau_b = [(I_1/\tau_1) + (I_2/\tau_2)]^{-1} \quad (4.3)$$

Where μ_d is the trapping coefficient for defects (dislocations), C_d is the dislocation concentration, τ_b and τ_d are the positron annihilation lifetime in bulk and in dislocations respectively. The concentration of dislocations is calculated from equation 4.2 using the trapping model with a trapping efficiency for dislocations in iron, $\mu_d = 6\times10^{-5}$ m^2s^{-1} [6]. It was tried to decompose all the lifetime data into two components. Only for the spectra measured at 500°C and 600°C the trapping model could be applied to the results. The bulk lifetime was calculated for both and it was found to be approximately 109 ps. Table 4.1 shows the values of the positron annihilation lifetime parameters and the concentration of defects in cold rolled less pure Fe samples annealed at 500°C and 600°C. The density of dislocations decreases with the increase of annealing temperature. At 700°C almost no trapping sites exist and hence there is no data for the density of dislocations starting from 700°C. It is known that after 900°C there will be a phase transformation α/γ (see Figure 2.1). We wanted to see change in the positron annihilation parameters due to this phase transition. The data for the τ_{mean} after the annealing at 800°C shows a tiny change but can not be considered significant.

Table 4.1 The positron annihilation lifetime parameters and the concentration of defects in cold rolled Less pure Fe samples annealed at 500°C and 600°C

T(°C)	τ_1 (ps)	τ_2(ps)	I_2	τ_b (ps)	Defect Concentration x 10^{14} (m^{-2})
500	62	155.3	0.713	109	1.15
600	63.9	146.9	0.724	109	1.0447

4.3.2 S Parameter (bulk)

The dependence of the *S* and *W* parameters on the isochronal annealing temperature for deformed less pure Fe is shown in Figure 4.3 (a, b). In the temperature range (23- 400°C) the S parameter slightly decreases while the W parameter slightly increases. Starting from 400°C, a significant decrease of the S parameter accompanied with a significant increase of the W parameter is observed and both become constant above 700°C. The behavior of the S parameter presented in Figure 4.3 (a) is similar to one observed for the τ_{mean} in Figure 4.2. Figure 4.3 (b) shows the S- W relation for all the isochronal annealing temperatures from 100°C up to 1000°C for the less pure iron samples. The relation shows one straight line. This means that only one type of defect (dislocations as identified by the lifetime), exists in the deformed iron through the isochronal annealing temperature range.

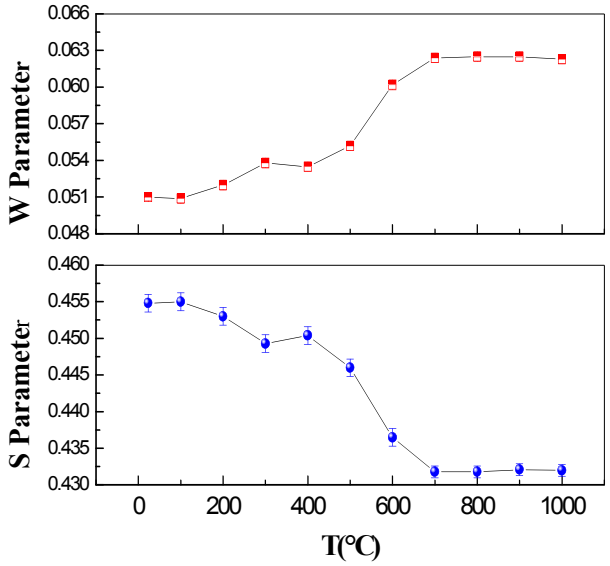

a)

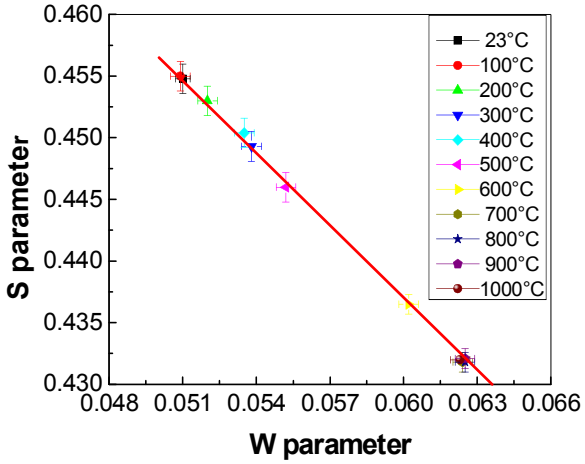

b)

Figure 4.3 a) The annihilation line shape parameters (S, W) as a function of the isochronal annealing temperature of the deformed less pure iron (annealing time 1 h), and **b)** the S– W relation.

4.4 Conclusions

The isochronal annealing curve for the positron mean lifetime reveals that the traps for positrons in the deformed iron are mainly dislocations. With increasing the annealing temperature, the Doppler broadening parameter *S* and the positron annihilation lifetime τ_{mean} have a slight decrease before the recovery temperature region. The S- W relation shows only one straight line, which means that only one type of defect, exists in the deformed iron through the whole isochronal annealing temperature range. This is consistent with the positron lifetime data.

4.5 References

[1] P. Hautojarvi, J. Heinio, M. Mannien, and R. Nieminen, Phil.Mag.35, (1977) p. 973

[2] C. Dauwe, M. Dorikens, L. Dorikens-Vanpraet, and D. Segers, Appl. Phys. 5, (1974) p.117

[3] B. T. A. McKee, S. Saimoto, A. T. Stewart, and M. J. Stott, Can. J. Phys. 52, (1974) p.759.

[4] T. Wider, S. Hansen, U. Holzwarth, and K. Maier, Phys. Rev. B 57,(1998) 5126

[5] C. Hidalgo, G. González Doncel, S. Linderoth and J. S. Juan, Phys. Rev.B 45, (1992) p.7017.

[6] Y. K. Park, J. T. Waber, M. Meshii, Jr., C. L. Snead and C. G. Park, Phys. Rev. B 34, (1986) p.823.

[7] Y. Kamimura, T. Tsutsumi and E. Kuramoto, Phys. Rev. B, 52-2, (1995) p.879.

[8] M. Militzer, W. P. Sun and J. J. Jonas, Acta Metall. Mater.42, (1994) p.97.

[9] P. Hautojärvi, A. Tamminen and P. Janho, Phys. Rev. Lett.24, (1970) p.459.

[10] C. Hidalgo, S. Linderoth and N. de Diego, Phys. Rev. B36, (1987) p.6740.

[11] C. Hidalgo, S.Linderoth and N.de Diego, Phil.Mag.A64, (1986) p.L61.

[12] M. Takahashi, A. Okamoto, Trans. ISIJ, 19, (1979) p.391.

[13] W. B. Hutchinson, Int. Met. Rev. 29, (1984) p.25.

[14] C. L. Snead, Jr., A. N. Goland, J. H. Kusmiss, H. C. Huang, R. Meade: Phys. Rev. B 3 (1971) p.275.

[15] I. K. MacKenzie: Phys. Stat. Sol. (a) 12, K (1972) p. 87.

[16] P. Hautojarvi, A. Vehanen, and V. S. Mikhalenkov, Appl. Phys. 11 191, (1976) p. 191.

Chapter 5
A study of defects in deformed FeSi alloys using positron annihilation techniques

Steels with high silicon content are used in electrical applications due to their low magnetostriction, high electrical resistivity and reduced energy losses, but unfortunately they exhibit poor formability.

In this chapter a study of defects in FeSi was performed using the positron annihilation spectroscopy (PAS). The defects were induced by deforming the alloys at high and low (room) temperature. The effect of Si content on the positron annihilation lifetime of the deformed samples was also studied. The slow positron beam of Gent University was used to investigate defects in different deformed FeSi alloys. It was found that the concentrations of defects for the alloys deformed at high temperatures are different from the ones of the alloys deformed at room temperature.

5.1 Introduction

Alloying iron with silicon improves its magnetic performance by reducing the effect of magnetostriction, noise and energy losses while the electrical resistivity increases, although all those properties are also influenced by the grain size and crystallographic texture. Despite of the magnetic improvement of electrical steels their workability is extremely reduced by the appearance of ordered structures, namely B2 and D03, once the Si content is higher than 4.5 wt.%. The addition of silicon has also a strong influence on the iron α-γ allotropic transformation, where steels with Si content higher than 1.8 wt.% have a bcc crystallographic phase up to their liquidus temperature. The magnetic losses can be reduced by controlling the final microstructures and crystallographic textures. The energy stored in the material during the room temperature deformation is used during

the annealing treatment to obtain new recrystallized grains [1-3]. The positron annihilation technique is known to be a highly sensitive probe for open volume defects [4]. The defect structure after deformation of metallic samples can also be investigated with the positron annihilation technique [5]. PALS can quantify the size of open volume defects as well as the defect concentration and is based on the precise measurement of the lifetime spectrum for positrons in a solid. The concentration of defects can be deduced from the fraction of positrons that annihilate from a trapped state. The defect size is directly related to the position lifetime; the larger the defect, the lower the local electron density is and consequently the longer the positron lifetime will be [6].

Thermally formed defects have also been observed by applying infrared spectroscopy [7] or electrical experiments [8] in samples that have been rapidly quenched after thermal or laser annealing. These experiments, however, do not report vacancy concentrations at thermal equilibrium. Positron annihilation spectroscopy has been one of the major techniques used to study the formation of thermal vacancies in metals [9].

5.2 Experimental work

The chemical composition of the investigated alloys was determined with a Spectro LAVWA18A spectrometer of Spectro Analytical Instruments. This composition is shown in Table 5.1. The production of the alloys is described in detail by Rodriguez in [10]. The deformation was carried out by plane strain compression tests using the Material Testing System (MTS), see Figure 5.1.

Table 5.1 Chemical composition (wt. %) for the FeSi alloys

Element wt. %	C	Si	Al	Mn	P	S	Ti	N
Steel A	0.002	1.88	0.075	0.048	0.016	0.009	0.002	0.003
Steel B	0.004	3.02	0.098	0.046	0.015	0.009	0.003	0.002
Steel C	0.003	4.06	0.096	0.066	0.016	0.009	0.003	0.007

Figure 5.1 MTS compression machine

This MTS machine has two moving actuators, called hammer and anvil. The first one with a maximum force capacity of 500 kN and maximum crosshead speed of 4 m/s was used for the high temperature deformations, while the anvil with 2500 kN and 3 m/s, respectively, was used for the room temperature tests.

The microstructures of the alloys were investigated by the electron backscatter diffraction (EBSD) technique [10, 11]. The crystallographic information was obtained from polished samples using a scanning electron microscope (SEM). The samples were prepared following standard metallographic procedures. The last polishing was with colloidal silica (OPU) of 0.035 μm particle size [10, 11]. As the electron beam of the SEM strikes the surface perpendicular to the transversal direction (TD) of a tilted specimen, the electrons are elastically scattered beneath the surface. The diffracted electrons form Kikuchi patterns on a

fluorescent screen, allowing the identification of the crystal orientation. As a polycrystalline sample is scanned by the electron beam, information on the crystalline orientation at each point is collected [12]. The resulting scans reveal the grain morphology and crystallographic orientations of the sample. The samples scanned using the EBSD technique were analyzed with orientation imaging microscopy (OIM) software.

From the deformed and as-received material, samples with an area of 1 cm^2 perpendicular to the normal direction of deformation (ND) were prepared for positron annihilation measurements, using a similar metallographic procedure as for the EBSD samples to avoid the distortion of the crystalline lattice while polishing.

The DBAR measurements were performed using the Ghent Slow positron facility, which is fully described in [13]. The spectra were analysed using line-shape parameters, explained in Chapter 3. Positron lifetime measurements were performed at room temperature using a fast-fast lifetime spectrometer.

5.3 Results and discussion

5.3.1 Mechanical properties

5.3.1.1 High temperature deformation

The mechanical behavior of the materials compressed to 75 % at 1000°C with a strain rate of $5s^{-1}$ is characterized by an increase in the stress values as the Si concentration increases. The initial microstructure consists of average equiaxed grain size of 215, 225 and 200 μm for Steel A, B and C, respectively. Increasing the Si concentration leads to a well developed sub-grain structures and elongated grain in the rolling direction. [10].

5.3.1.2 Room temperature deformation

The same initial materials were deformed at room temperature with strain rate of 15 s^{-1} to 10, 35 and 75 % levels of thickness reduction. When deforming to a thickness reduction of 5 % the flow stress is above 700 MPa, see Figure 5.2 (a),

then extensively mechanical twins (Σ3 *Coincident Site Lattice* [CSL] boundary) are observed which are produced by a rotation of 60° along <111> axis respect to the parent grain. Σ is defined as the reciprocal density of coincident sites at the boundary between two adjoining grains. Σ3 means that one out of three atoms overlap in a new lattice. When the flow stress is below 700 MPa, then the plastic deformation is accommodated by mechanical slip. At deformations to a thickness reduction of 35 %, bended twins and shear bands (deviated 20 to 35° from the rolling direction) within pancake grains elongated along the rolling direction are commonly observed in the EBSD scans; see Figure 5.2 (b).

Finally, in samples deformed to 75% thickness reduction more shear bands and fragmentized twins inside banded shape grains are present. In general, the room temperature deformation behavior of the studied alloys is similar to the one reported for 2.7 wt. % Si [11]. The drop in the image quality parameter obtained by EBSD, as the deformation progresses, indicates an increase in the dislocation density and the amount of the shear band increases as the Si content increases.

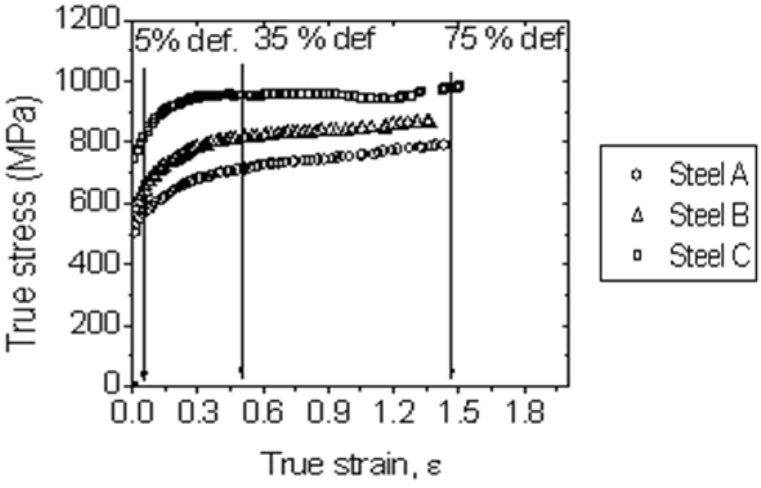

a)

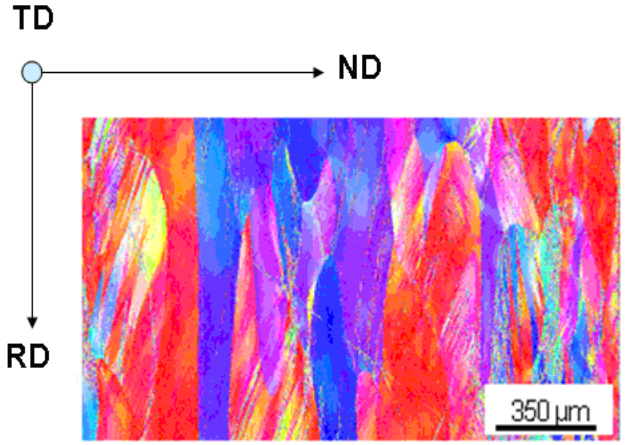

b) Steel B

Figure 5.2 (a) Stress-strain curves of the Fe-Si alloys deformed at room temperature and (b) EBSD scan of FeSi sample with 3 wt.% Si deformed 35 % (steel B).

5.3.2 Positron techniques:

5.3.2.1 High temperature deformation

5.3.2.1.1 Slow positron beam Doppler Broadening analysis.

The Doppler broadening of the annihilation radiation (DBAR) measurement was performed using the Ghent Slow positron beam, which is fully described in [13]. The measurements were done at room temperature. The three alloys were measured before and after a deformation at 1000°C to a thickness reduction of 75 % and water quenched. The depth profiling was achieved by varying the implantation energy of the slow positrons from 0.1 to 30 keV corresponding to mean implantation depths up to 1μm. The results, presented in Figure 5.3, show the S parameter as a function of incident energy of the implanted positrons and the evolution of the line-shape parameters (W, S) at 30 keV as a function of the Si content. The windows for the line-shape parameters were set in order to have a bulk (S, W) for defect free iron of (0.44, 0.125). From the shape of the curve of the S parameter with increasing implantation energy, it is possible to observe that the line-shape parameter in the bulk of deformed samples changes drastically. The evolution of bulk line-shape parameters (S, W) lays nearly on one line indicating that one fraction of the positrons annihilate in the defect free state while the other fraction in one type of defect. For each sample with the same Si content (2%, 3% or 4%) upon deformation, the S parameter increases. The S parameter decreases with increasing the Si content for the undeformed as well as for the deformed samples.

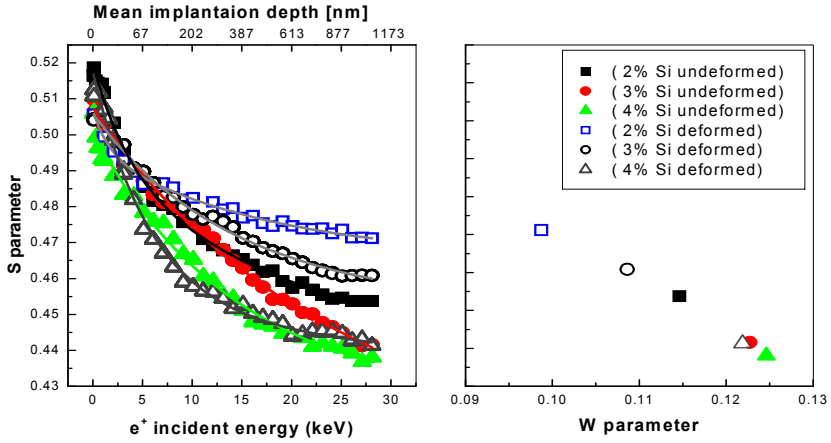

Figure 5.3 Representation of **(a)** the S parameter as a function of incident energy of the implanted positrons and **(b)** the evolution of the line-shape parameters (W, S) at 30keV as a function of the Si content and deformation.

5.3.2.1.2 Positron annihilation lifetime spectroscopy (PALS)

The positron annihilation lifetime value for the three undeformed FeSi alloys is 108 ± 3 ps. This value is not far from the one of the pure iron, which is 107± 3 ps. For the deformed alloys 75% thickness reduction at high temperature (1000°C) and water quenched, there are two components in the positron lifetime spectrum. Figure 5.4 shows the relation between the positron annihilation lifetime and the Si content. The value of the second lifetime component (τ_2), which is related to the annihilation in defects decreases by increasing the Si content, while its intensity (I_2) has a maximum value for the alloys with 3 wt.% Si. Also, the mean positron lifetime shows a maximum value for the alloys with 3 wt.% Si. The value of the second lifetime component is around 190 ps. This value indicates the existence of mono-vacancies. The other component, which is less than 100 ps, is the result of the annihilation of free positrons. For the Fe2%Si, the defect lifetime is about 210ps which larger than the lifetime of a mono-vacancy. This lifetime is a superposition of two lifetime components: one

originating from a vacancy cluster and a second one from mono-vacancies or dislocations.

Comparing between the data of Figure 5.3 and Figure 5.4, it is clear that the positron annihilation lifetime in defects (τ_2) decreases with increasing the Si content in the alloy, which is the same behaviour as the S parameter in Figure 5.3. The mean value of the positron annihilation lifetime has a maximum value for the alloys with 3 wt.% Si. Calculating the bulk lifetime (equation 4.3) for the three samples, shows that the Fe3%Si has a bulk value around 120ps while a value of 112ps is found for the Fe2%Si and the Fe4%Si. As it was shown before that the bulk lifetime value is 108 ps. This can give a conclusion that the maximum defect concentration (Figure5.3) for the Fe3%Si is a fitting artefact.

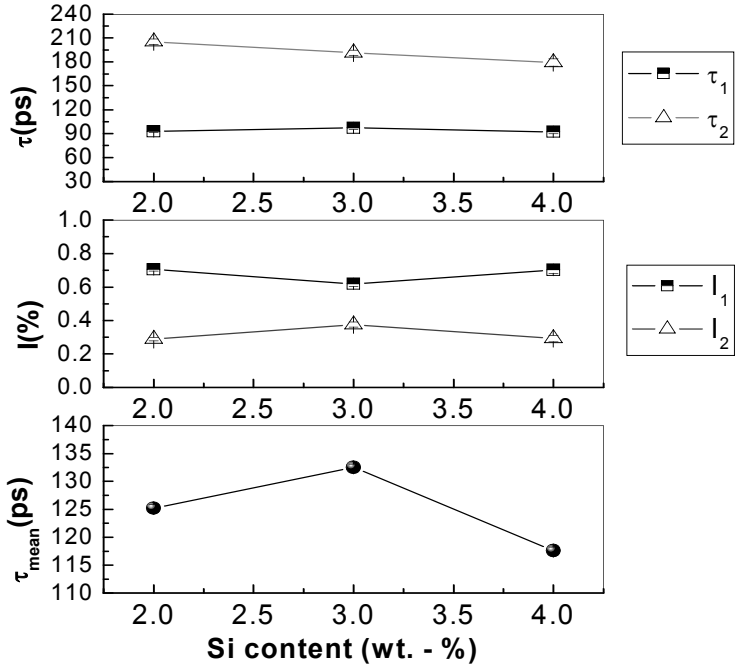

Figure 5.4 Comparison of Positron annihilation lifetime data for the different contents of Si 75% deformed at high temperature (1000°C) and water quenched.

Using the trapping model with a trapping coefficient for a single vacancy in pure Fe, $\mu_v = 1.1\times10^{15}\ s^{-1}$ [14, 15], a defect concentration could be calculated.

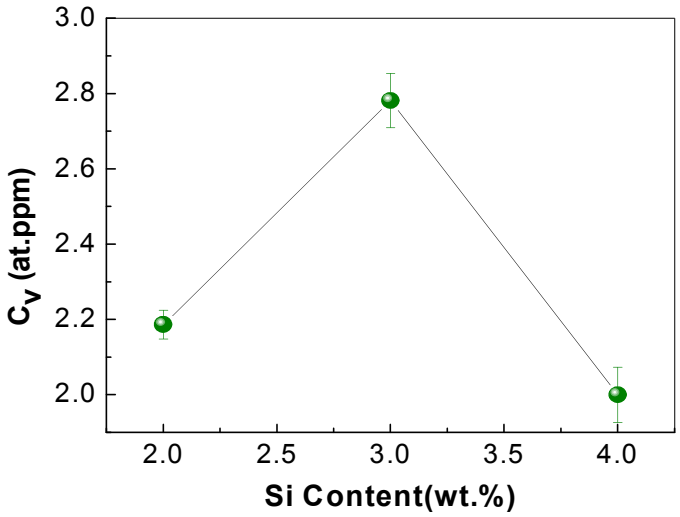

Figure 5.5 Representation of the variation of the vacancy concentration, $C_{v,}$ with Si content for a 75% deformed samples at high temperature (1000°C) and water quenched.

Figure 5.5 shows the relation between the vacancy concentration C_v with the Si content. It was found that at 3 wt.% Si there is a maximum value for the vacancy concentration. The delay in quenching the samples was approximately 2 s, which was time enough to trigger the static restoration process as recovery and recrystallization in different extent. It is hard to have a clear conclusion from only 3 points. For this reason more samples with different Si content are needed to be examined.

5.3.2.2 Room temperature deformation

5.3.2.2.1 Positron annihilation lifetime spectroscopy (PALS)

The samples in the same initial state used for the high temperature deformations were deformed at room temperature (75% thickness reduction). All positrons were trapped in defects as shown in Figure 5.6. The spectra were fitted using two positron lifetime components. The first one is around 150 ps, which is attributed to the annihilation of positrons in dislocations. The other component is higher

than 240 ps and is related to the annihilation of positrons in vacancy clusters [14]. The intensity of positron annihilation in dislocations higher than 85 %, see Figure 5.6 b, indicates that the deformation temperature affects the concentration and the type of defects formed in the alloys through the deformation process.

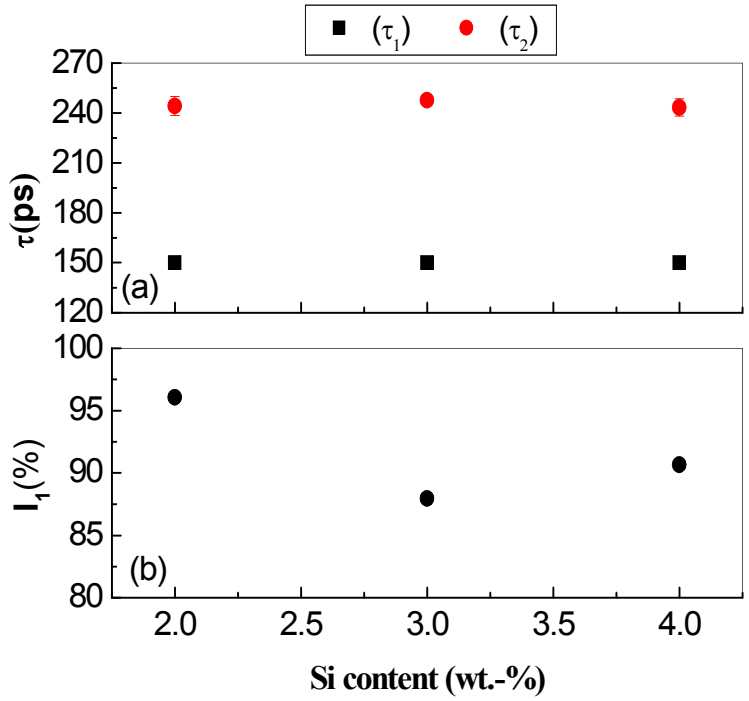

Figure 5.6 Representation of **(a)** the positron annihilation lifetime and **(b)** intensity for different Si samples 75% thickness reduction at room temperature.

5.4 Conclusions

The data of the positron annihilation techniques have shown that the deformation temperature affects the concentration and the type of defects formed in the alloys through the deformation process and it is possible to withdraw the following conclusions:

1. Mono-vacancies are found to be the main type of defect formed during deformation at high temperatures. In case of room temperature deformation both dislocations and vacancy clusters are formed in the FeSi alloys.

2. For the high temperature deformed samples, the positron annihilation lifetime in defects (τ_2) and the S parameter decrease with increasing Si content in the alloy.

3. For the room temperature deformed samples, there is a saturation trapping for positrons in defects and the two lifetime components present of 150 ps and 250 ps are related to the positron annihilation in dislocations and indicator for the existence of vacancy clusters, respectively). The concentration of vacancy clusters increase with increasing the Si content.

5.5 References

[1] A. F. Filho, C. Bolfarini, Y. Xu, C.S. Kiminami, Scripta mater.42, (2000) p.213.

[2] G. Lyudkovsdy, P.K. Rastogi, M. Bals, J. Met.1, (1986) p.18.

[3] D. Ruiz, T. Ros-Yanez, R. E. Vandenverghe and Y. Houbaert, Steel Research Int.76, (2005) p.21.

[4] P. Hautojarvi and A. Vehanen: Positrons in Solids, Ed. P. Hautojärvi, 1979, p.1.

[5] R. N. West: Positrons in Solids, Ed. P. Hautojärvi (Springer-Verlag, Berlin, Heidelberg and New York, (1979) Chapter 3.

[6] P. Hautojarvi, J.Heinio, M.Mannien, and R.Nieminen, Phil.Mag.35, (1977) p.973.

[7] N. Fukata, A. Kasuya, M. Suezawa, Jpn. J. Appl. Phys. 40. L854 (2001).

[8] A. Chantre, M. Kechouane, D. Bois. Physica., (Amsterdam) 116 B., 547 (1983).

[9] X. Y. Zhang et al., Phys. Rev. Lett. 92, (2004) p. 155502.

[10] P. R. Calvillo and Y. Houbaert, J. Mater. Sci. Forum.553, (2007) p.15.

[11] P. R. Calvillo, R. Petrov, Y. Houbaert and L. Kestens, J. Mater. Sci. Forum.550, (2007) p.539.

[12] V. Randle and O. Engler, Introduction to Texture Analysis-Macrotexture, Microtexture and Orientation Mapping, Taylor & Francis Ltd, London (2003).

[13] J. De Baerdemaeker, J. Colaux, G. Terwagne and C. Dauwe, J. Radiat. Phys. Chem.68, (2003) p.605.

[14] A. Vehanen, P. Hautojarvi, J. Johansson, J. Yli-Kauppila, P. Moser, Phys. Rev. B 25, (1982) p.762.

[15] Y. K. Park, J. T. Waber, M. Meshii, C. L. Snead, Jr., and C. G. Park Phys. Rev. B 34, (1986) p.823.

Chapter 6
Influence of carbon on the microstructure of a FeMnSiCrNi alloy

In this chapter the influence of the addition of carbon to the FeMnSiCrNi base material is investigated at room temperature. Steel samples were deformed during a tensile experiment up to a strain of 17 %. Light optical microscopy (OM) and XRD gave information about the different microstructural phases that exist in the deformed and the undeformed alloys. The evolution of the defect structure is followed by positron annihilation techniques such as Doppler broadening of the annihilation radiation spectroscopy (DBAR) and the positron annihilation lifetime spectroscopy (PALS). During deformation a martensitic ε–phase is induced. The size of the martensite plates increases with increasing deformation.

6.1 Introduction

The large hysteresis and a poor shape recovery in the FeMn binary system was addressed by making specific alloying additions of Si, C, Co, Ni, and Cr. In order to reach a complete shape memory effect, three conditions must be fulfilled. First, the deformation must result in the stress-induced ε martensite formation only. Second, the yield stress of the γ matrix should be as high as possible to avoid an initial deformation by slip. Finally, the shape strain of stress-induced martensite should be completely reversible, which means that the martensite interface must remain mobile at all times. The forward and reverse transformations occur by the movement of planar martensite interfaces, which contain the transformation dislocations. The required martensite morphology for ferrous SMA is of the thin plate type.

Because the shape memory alloys possess low stacking fault energy, the nucleation of the martensite may occur by means of the stacking fault mechanism [1]. The transformation results in thin ε martensite plates, which have specific crystallographic orientations with respect to each other. This is due to the fact that the martensitic γ –> ε transformation is obtained by the glide of isolated Shockley partial dislocations on every second $\{111\}_\gamma$ plane. There is no macroscopic deformation of the single crystal when the γ –> ε transformation is induced thermally. The deformation results in the dominance of ε martensite variants, which are suitably oriented with respect to the applied stresses, and a decrease of the volume fraction of the other ε variants in each original γ grain. The ε martensite forms dense regions of transformed regions, which still contain the parent γ phase. At the intersection of two variants of ε martensite, α' martensite was often observed [2]. It is very likely that the formation of α' martensite is the main cause for relatively low recovery of the ferrous SMAs. The α' regions impede the reverse motion of the Shockley partial dislocations.

In the present study, the influence of deformation and carbon addition on FeMnSiCrNi alloys is studied by a combination of optical microscopy (OM), X-ray diffraction (XRD) and Positron Annihilation Spectroscopy (PAS) techniques. OM and XRD can give information on the different phases present in the material. PAS techniques were used to study the defect behavior in the samples and to see if any effect of the phase transformation during deformation could be detected.

During the last few years, the positron annihilation technique has been widely used to study defects and phase transition in SMAs. Most of the work had done on the Ni-Ti and Cu-based alloys [3- 5]. Very few publications had been published about the FeMn based alloys [6, 7]. The defect structure after plastic deformation of metallic samples can also be investigated with the positron annihilation technique [8]. S. Hautakangas et al. [9] studied the tensile deformation of Al alloys to detect the nano-cracks in the tensile deformed materials using the positron annihilation technique. They concluded that the increased plastic load increases the S parameter and the positron annihilation

mean lifetime while, the elastic deformation of the sample does not have a recordable effect on the positron annihilation data. Yasuhiro Kawaguchip et al. [10] studied the fatigue evaluation of Type 316 Stainless Steel. They have found that positron annihilation line-shape parameter and the positron annihilation lifetime measurement can detect fatigue damage at an early stage of fatigue. F. Selim et al. [11] used the positron annihilation technique to probe the defects at high depths in thick materials up to several centimeters. Stress measurements were performed using accelerator-based γ-ray induced positron annihilation spectroscopy technique.

Some measurements of positron annihilation have been made for martensitic transformations in metals and alloys [12- 15]. Dislocations produced during the transformation must be considered when martensitic transformation is studied by positron annihilation. D. Segers, J. Van Humbeeck and I. Hurtado studied different types of shape memory alloys [6, 16- 17].

It is expected that PAS can help in understanding more about the stress- induced martensitic transformation in FeMn based alloys. Two basic techniques are used: positron annihilation lifetime spectroscopy (PALS) and Doppler broadening of the annihilation radiation spectroscopy (DBAR).

6.2 Experimental

Two different FeMnSiCrNi alloys were prepared for this study. Their chemical composition is given in Table 6.1. They were cast in an air furnace, air cooled, reheated to 1200°C and hot rolled on a laboratory mill from 20 mm to 2 mm and air cooled. In order to austenitize the samples; they were heated to 1100°C for 15 minutes and water quenched to room temperature.

Table 6.1 The chemical composition of FeMnSiCrNi-(C) in wt. %

Element	Fe	Mn	Si	Cr	Ni	C
FeMnSiCrNi	67.34	12.6	6	9.27	4.74	0.05
FeMnSiCrNiC	66.84	12.56	6.09	9.44	4.89	0.18

Positron lifetime measurements were performed at room temperature using a fast-fast lifetime spectrometer. The tensile tests were carried out on LRX–PLUS (LLOYD Instruments) tensile test machine with maximum force of 5 kN. The shape and dimensions of the specimens are shown in Figure 6.1.

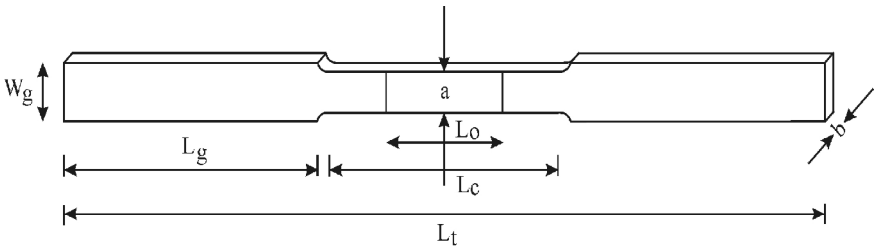

Specimen type	a	Lt	Wg	Lg	Lc	Lo	b
FeMn	7	150	10	50	45	23	1

Dimensions in mm

Figure 6.1 LRX–PLUS tensile machine and the shape and dimensions of the sample

Tensile test was performed to make elongation of the sample. The elongation rate was 0.1 mm/min. The machine is controlled by a LabVIEW program written by S. VAN Petegem. The strain is determined using the motor position. During the deformation of the sample (in-situ measurement), the Doppler broadening (DB) of the 511 keV annihilation line is measured using a high purity germanium detector with a resolution of 1.2 keV at the 514 keV line of ^{85}Sr. The results are analyzed in terms of the so-called S- and W-parameter. The positron annihilation lifetime the light optical microscopy and the XRD are measured for the samples before and after the tensile deformation.

6.3 Results and discussion

6.3.1 XRD and OM

Figure 6.2 shows the microstructure of the FeMnSiCrNi(C) alloys before, and after deformation. The microstructural analysis for the undeformed samples revealed the presence of large austenite grains (γ phase), residual ferrite grains and ε phase. The amount of residual ferrite grains between the austenite is less in the alloy without carbon.

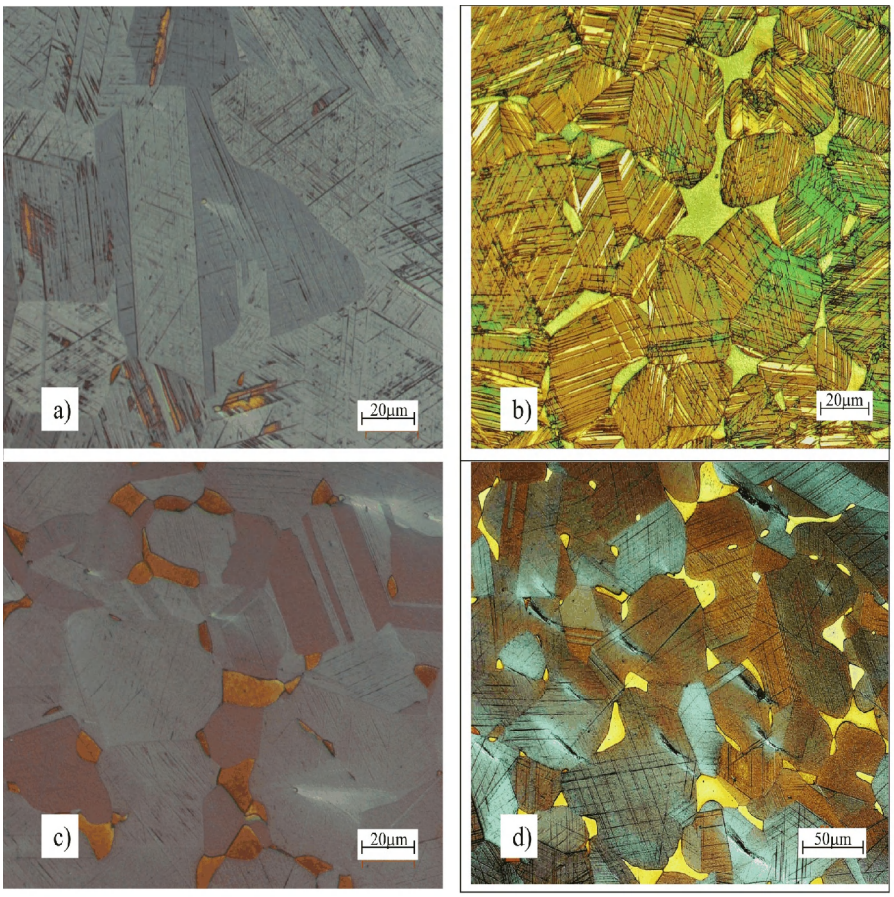

Figure 6.2 Light optical microstructures (OM) for the alloys:
(a) undeformed FeMnSiCrNi, (b) deformed FeMnSiCrNi,
(c) undeformed FeMnSiCrNiC and (d) deformed FeMnSiCrNiC

This is also measured with XRD (Figure 6.3). The ε martensite is clearly visible in the alloy without carbon and is less present in the carbon alloyed one. As can be seen from Figure 6.2, it appears as thin parallel lines with dark contrast inside the austenite grains. This small quantity of ε martensite before the deformation process is probably induced during grinding or polishing or can be induced thermally. The OM images show that the alloy without carbon has more ε martensite than the alloys with carbon before the deformation (see Figure 6.2 a

and c). The XRD shows something different, where the intensity of the (100)ε for the alloy with carbon is higher than the one for the alloy without carbon. This may support the idea that the ε marentsite seen in the low carbon is related to polishing. By deformation, more ε martensite is transformed from the austenite. There is an increase in the intensity of the (002)ε peak. In the OM, the ε phase appears as broader white lines in the alloy without carbon (Figure 6.2-b) and clearly thinner black lines in the alloy with carbon (Figure 6.2-d). From the XRD result we can also conclude that the alloy without carbon contains more ε martensite phase.

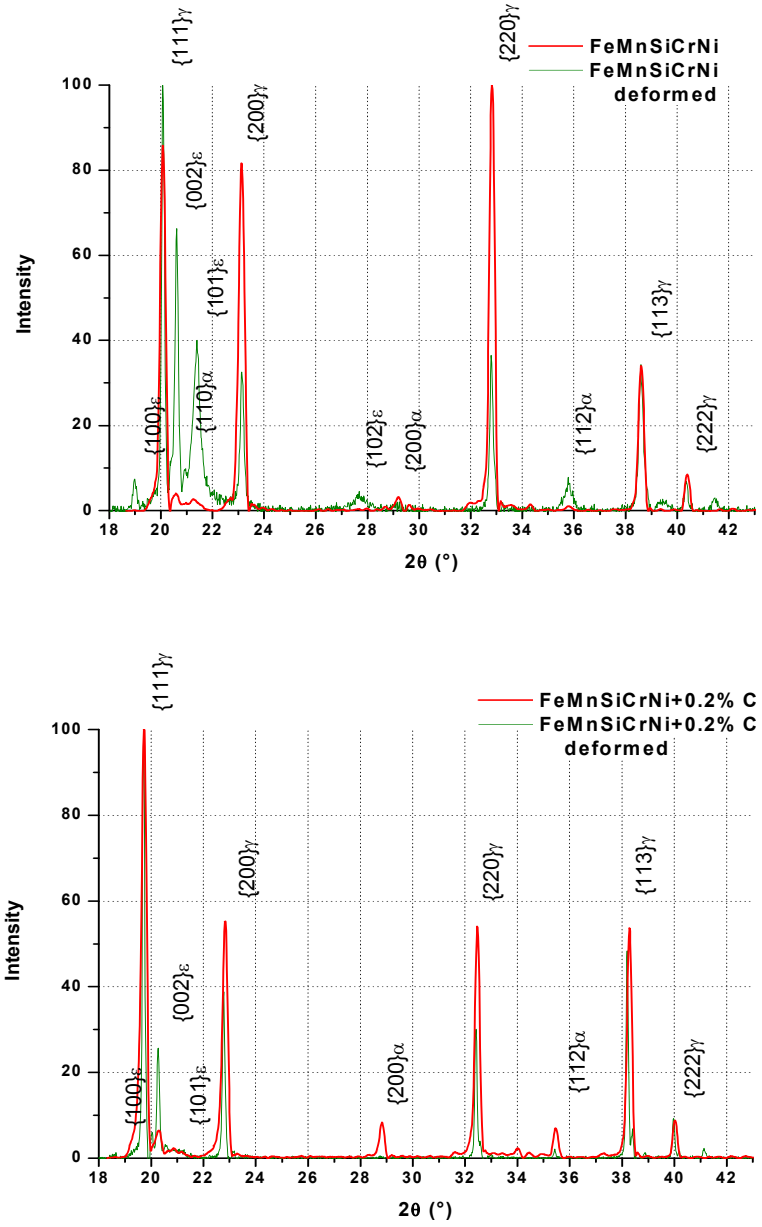

Figure 6.3 XRD for the alloys (top) undeformed and deformed FeMnSiCrNi (bottom) undeformed and deformed FeMnSiCrNiC

Comparing the deformed and the non-deformed samples through the OM pictures, one can see that the stress induced $\gamma \rightarrow \varepsilon$ transformation increases with deformation. The high resolution electron microscopy (HRTEM) clarified that the stress induced $\gamma \rightarrow \varepsilon$ transformation proceeds by the growth and broadening of the existing ε martensite plates rather than the formation of new plates [18, 19].

6.3.2 Positron annihilation

6.3.2. a Positron annihilation lifetime

Positron annihilation lifetime data are presented in Table 6.2. For the undeformed samples of FeMnSiCrNi-(C), the lifetime for positrons was 107 ps which is the same as for defect free Fe. In the widely used two-state trapping model [20] it is assumed that positrons annihilate either in the bulk portion or get trapped in defects before annihilation. In the latter case, they survive longer in the material, which results in a longer lifetime. This variation of the lifetime values is related to the defect type (dislocation, mono-vacancy, cluster of vacancy, micro-void). In pure Fe, the lifetime value for positrons trapped in dislocations is around 160 ps and for positrons trapped in mono-vacancies, it is around 180ps [21- 24]. For the deformed samples, the positron annihilation lifetime spectra have two lifetime components. The shortest lifetime components τ_1 for the two samples are 61 ps and 67 ps, and are due to the annihilation of non-trapped positrons. The second lifetime component for the two samples is 151 ps and 150 ps, which are related to the positron annihilation in dislocations.

The concentrations of dislocations in both deformed samples (see Table 6.2) are calculated using the same equations and parameters used by Park [25].

Table 6.2 The positron annihilation lifetime and its intensity for in FeMnSiCrNi(C) samples before and after the tensile deformation.

Sample	τ_1 (ps)	I_1(%)	τ_2 (ps)	I_2(%)	Concentration of dislocations ($10^{14}m^{-2}$)
FeMnSiCrNi	107	100	-	-	
FeMnSiCrNi (15% deformed)	61	21	151	79	1.287
FeMnSiCrNiC	107	100	-	-	
FeMnSiCrNiC (15% deformed)	67	24	150	76	1.046

6.3.2. b Doppler broadening (DB) and stress–strain relation

There are different stages of deformation of the shape memory alloys, which have different deformation mechanisms. The first stage happens in the range of smaller strains, the self-accommodation mechanism of martensite plates, not the dislocation slip mechanism, is responsible for the deformation of the shape memory alloys. The orientation of martensite plates is adjusted or reoriented in accordance with the direction of the applied stress, which results in macroscopic deformation, but does not result in an increase of micro defects. Once the strain increases beyond several percent (7%), another deformation mechanism will take place. Dislocation slip produces many defects, capable to trap the positrons. The S parameter can be written as

$$S = \sum_i P_i S_i + \sum_i P_{d_i} S_{d_i} \qquad (6.1)$$

Where P_i is the probability of the annihilation of positrons in phase i and S_i is the respective line shape parameter. S_{d_i} counts for the part of positrons

annihilated due to the defects of phase *i* with its respective probability P_{d_i} [6]. In Figure 6.4, as the true strain is smaller than 7%, the change in *S* parameter is very small to be recognized and for deformations higher than 7% the *S* parameters increases remarkably. An increase of the defect density leads to an increase of the *S*-parameter in both samples, which can be recognized through the comparison of the data of the deformed and the undeformed samples. For the common metals and alloys the positron parameters increase markedly at the early stage of increasing strain, and rapidly became saturate when the samples are subjected to plastic deformation [26- 28]. After certain tensile strain, there will not be extra increase in the defect concentration, which could be the raison for the saturation of the S parameter (which is sensitive to the defects as explained before). S. Hautakangas et al. [29] concluded that the positrons are sensitive only to plastic deformation. i.e. generation of dislocations and other open volume defects, while the detection of the elastic deformation is obscured not only by a small increase in dislocation density at low strain values (< 2.3%), but also by experimental scattering and stability of set up (in- situ measurements).

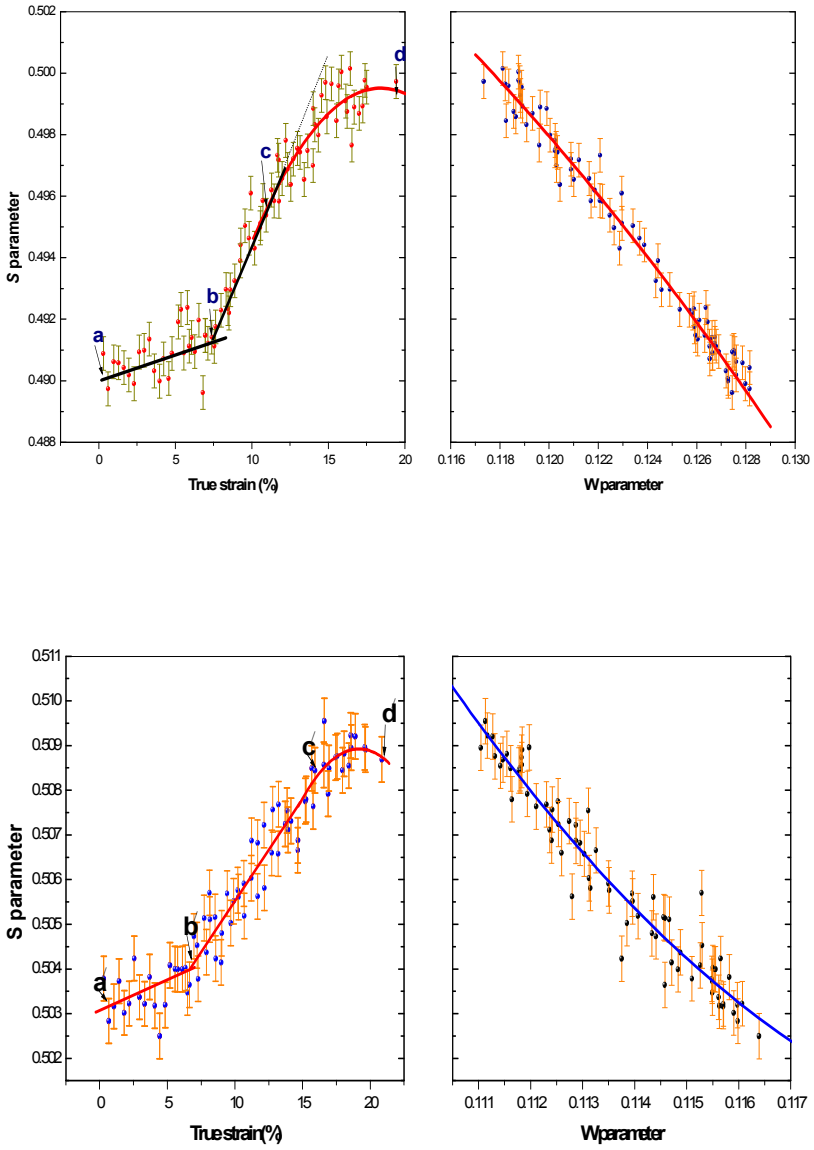

Figure 6.4 Plot of S and W parameters as function of the tensile strain for a (up) FeMnSiCrNi and a (below) FeMnSiCrNiC alloy.

Effect of carbon on the S parameter

In both samples (low carbon, high C sample) the pattern of the *S* parameter versus the true strain gave the *S*-line shape curve (Figure 6.4). At the first stage increasing the true strain up to 7% (a → b) and ($a^{/}$ → $b^{/}$) respectively leads to a slight increase in the value of the S parameter. *In situ* positron annihilation measurement, it is seems that is difficult to perform in the case of the FeMnSiCrNi the very early stages of deformation with low dislocation density. That is could be related to the non-homogenous low density dislocations. The next stage is starting from 7% up to 11% (b→ c) in case of the low C sample and from 7% to 16% ($b^{/}$→ $c^{/}$) for the high C sample. The value of the *S* parameter increases greatly with increasing strain and starts to have a kind of saturation when the low C sample is subjected to a strain higher than 11% (c→ d).

In the case of the high C sample the start of saturation is not recognized in the same way as for the low carbon sample, but it could be starting at a strain higher than 16% ($c^{/}$→ $d^{/}$). This is also observed in CuZnAl shape memory alloys [5]. The behavior of the *S* parameter in the case of the high carbon sample differs from that of the low carbon sample. The *S* parameter increases with increasing strain but the change in the *S* parameter is not that high as the one of the low carbon sample. This means that, the carbon content added to the alloy has an effect in the change of the microstructure and the concentration of defects created in the alloys.

During deformation the transformation $\gamma \rightarrow \varepsilon$ proceeds and α' martensite is formed at the intersections of the ε plates, which causes strain hardening. As shown by the XRD measurement, the low carbon alloy forms much more ε martensite during deformation, which results in a higher strain hardening compared to the high C alloy. Van Caenegem. N [30] said that the uniform elongation is larger for low C alloy. This might be correlated with the fact that due to the formation of the ε phase or twinning, the microstructure is progressively subdivided in much smaller sized units in the C- added alloy. Consequently, the effective grain size is reduced. In such steels with a smaller

grain size, more stress is needed for the movement and multiplication of dislocations. They are impeded by the grain boundaries, which lead to a lower strain hardening and a smaller uniform elongation. This can be recognized in the behavior of the *S* parameter in both samples. The *S* parameter increases with increasing deformation and in the case of low carbon steel, it is clear that the change in the *S* parameter is more than the one of high C sample.

From the *S-W* curve, the relation is not giving the very fine straight line especially in the low carbon sample. This can be ascribed to the existence of two types of effects or mechanisms. The first could be dislocations, which is correlated with lifetime results. The second might be related to the ($\gamma \rightarrow \varepsilon$) phase transition . This phase transition is very clear from the OM micrographs and the XRD, which is described above.

6.4 Conclusions

From the results of the positron annihilation, the Doppler broadening parameter *S* increases as a result of the trapping of positrons in defects. In the early stages of deformation, no significant increase of the S parameters for both alloys is observed. The increase of *S* is caused by an increasing number of lattice defects (dislocations). The starting of saturation of the *S* parameter corresponds to the equilibrium defect density. Phase transition might be detected from the *S-W* relation. The carbon content in the alloys has a significant effect in the value of the *S* parameter, which means the concentration of defects.

6.5 References

[1] H. Inagaki, Z fur Metallkd, 83, (1992) p.90.

[2] G. J. Arruda, V. T. L. Buono, M. S. Andrade., J. Mat. Sci., and Eng. 272- 275, (1999) p. 528.

[3] I. Hurtado , D. Segers , L. Dorikens Vanpraet , C. Dauwe , J. Van Humbeeck , J. Physique IV 5 Issue: C8 Part 2 (1995) p.949.

[4] I. Hurtado, D. Segers, J. Van Humbeeck, L. Dorikens-Vanpraet and C. Dauwe J. Scripta Metallurgica Materialia 33- 5, (1995) p.741.

[5] W. Jing-cheng, S. Zi-chang, Z. Hao, Scripta Metall.et Mater.24 (1990) p.1511.

[6] J. Van Humbeeck, G. Ghosh, L. Delaey, D. Segers, M. Dorikens, L. Dorikens Vanpraet, "Positron annihilation in the proceeding of the ICPA8 Conference" (1989) p.395

[7] T. Liu, R. D. Xia, G. W. Liu, Z. T. Zhao, R. Z. Ma, W. H. Wang and Y. H. Guo, J. Materials Science Letters 17, (1998) p.887

[8] K. Petersen, Proc. of "Enrico Fermi" Int. School of Physics, Edited by W. Brandt, (1983) p.298.

[9] S. Hautakangas, H. Schut, S. van der Zwaag, P. E. J. Rivera Diaz del Castillo, and N. H. van Dijk, phys. stat. sol. (c) 4, No. 10, (2007) p.3469.

[10] Yasuhiro Kawaguchi, Yasuharu Shiraij. Nuc. Sci. and Tec. 39- 10, (2002) p. 1033.

[11] F. A. Selim, D. P. Wells, J. F. Harmon, J. Williams. J. Appl. Phys. 97, (2005) p.113540

[12] J. Katsuyama, H. Araki, M. Mizuno, Y. Shirai Science and Technology of Advanced Materials 5, (2004) p.41

[13] T. d Troev, K. Hinode, S. Tanigawa and M. Doyama Appl. Phys.13, (1977) p.105.

[14] S. Tanigawa, K. Hinode, T. Yamauchi, M. Doyama, New Aspects of maternsitic transformation, Tokyo, Japan Inst. Metals, (1976) 123-8.

[15] P. Hautojarvi, T. Judin, A. Vehanen, J. Yli-Kauppia, V. S Mikhalenkov, 1979 Proc. 5th Int. Conference on Positron Annihilation.

[16] I. Hurtado, D. Segers, J. Van Humbeeck, L. Dorikens-Vanpraet and C. Dauwe, Scripta Metallurgica et Materiali, 33 (5), (1995) p.741.

[17] D. Segers, J. Van Humbeeck, L. Delaey, M. Dorikens and L. Dorikens, Positron Annihilation Proceedings of the Seventh International Conference (world scientific, Singapore, 1985) p.880.

[18] Huijun Li, Druce Dunne, Noel Kennon, materials Science and Engineering A173- 275, (1999) p.517

[19] B. Bergersen and M. J. Stott, Solid State Communic., 7, (1969) p.1203

[20] R. N. West; in “positrons in Solids, series” Topics in Current Physics (12) ed. by P. Hautojarvi, Springer, Berlin 89, (1979)

[21] T. E. M. Staab, R. Krause-Rehberg, and B. Kieback, Materials Science 34, (1999) p.3833.

[22] M. J. Puska, P. Lanki, R. M. Nieminen, J. Phys., Condens. Matter, (1989) p.6081.

[23] Y. Kamimura, T. Tsutsumi, E. Kuramoto, Phys. Rev. B 52, (1995) p.879.

[24] K. M. Mostafa, J. De Baerdemaeker, Pablo R. Calvillo, N. Van Caenegem Y. Houbaert, and D. Segers, J. Acta Physica Polonica A 113-5, (2008) p.1471.

[25] Y. K. Park, J. T. Waber, M. Meshii, C. L. Snead, Jr., and C. G. Park, Phys. Rev. B 34, (1986) p.823.

[26] I. K. Mackenzie, A. Eady, R. R. Gingerich, Phys. Lett.A 33, (1970) p.279.

[27] J. Baram and M. Wayman, Metall. Trans. A23, (1992) p.263.

[28] K. M. Mostafa, N. Van Caenegem, J. De Baerdemaeker, D. Segers, Y. Houbaert, Physica status solidi (c) 4-10, (2007) p.3554.

[29] S. Hautakangas, H. Schut, S. van der Zwaag, P. E. J. Rivera Diaz del Castillo, and N. H. van Dijk, phys. stat. sol. (c) 4, No. 10, (2007) p.3469

[30] N. Van Caenegem , PhD thesis, Universiteit Gent, Belgium, 2007

Chapter 7
Investigation of defects and phase transitions in deformed FeMnSiCrNiC

In this chapter, the martensitic transformation and defects induced by the tensile deformation of a FeMnSiCrNiC alloy were investigated. Samples deformed from 2 to 20% were investigated using positron annihilation spectroscopy, optical microscopy (OM) and X-ray diffraction (XRD). Both Doppler broadening of the annihilation radiation (DBAR) and positron annihilation lifetime spectroscopy (PALS) measurements were performed. The DBAR experiments, carried out using a slow positron beam, indicate a sudden increase in the defect concentration in between 4 and 6% deformation. This is confirmed by the lifetime measurements. In between 6% and 8% deformation the line-shape parameter significantly changes which coincides with the drastic increase of the concentration of the martensite phase as confirmed by XRD. Positron annihilation spectroscopy is indirect probes the γ/ε martensitic phase transformation by probing correlated dislocations.

7.1 Introduction

In the present study, the influence of the tensile deformation on FeMnSiCrNiC alloys is studied by a combination of optical microscopy (OM), X- ray diffraction (XRD) and Positron Annihilation Spectroscopy (PAS) techniques. OM and XRD are used to investigate the different phases formed with deformation. X-ray diffraction [1] is widely used in investigating the microstructure of materials, but it is restricted to small penetration depths (about 10 μm maximum).

In order to better understand the relation between the defects introduced in the sample by deformation and the evolution of the presence of "strain induced" phases, DBAR and positron annihilation lifetime spectroscopy (PALS) measurements are compared with OM and XRD measurements.
Dislocation lines or any change in the spacing of the lattice planes due to deformation act as open volume defects. They form an attractive potential that trap positrons at these sites [2].

7.2 Experimental work

The chemical composition of FeMnSiCrNiC is given in Table 7.1.

Table 7.1 Chemical composition of the FeMnSiCrNiC samples

Element	Fe	Mn	Si	Cr	Ni	C
Wt. %	66.84	12.56	6.09	9.44	4.89	0.18

The samples were deformed by tensile loading (2%, 4%, 6%, 8%, 10% and 20%) at room temperature. These deformed specimens were cut, mechanically polished and then electrolytically polished in a solution of 20% perchloric acid and 80% butylcellosolve. For the OM the specimens were color etched (see chapter 3). The microstructure was investigated on a Zeiss Janavert optical microscope.

Positron lifetime measurements were performed at room temperature using a fast-fast lifetime spectrometer. The DBAR measurements were performed using the Ghent Slow positron facility, which is fully described in [3]. The spectra were analyzed using the well known line-shape parameters.

7.3 Experimental results

7.3.1 Light optical microscopy (OM) and XRD

The color etching method is very important to verify the presence of the different phases that exist in this alloy especially the α′-martensite. When the volume fraction of this phase is very low, the X-ray diffraction can not identify it.

The microstructural analysis of the samples by OM reveals the presence of large γ– austenite grains, residual ferrite grains and ε phase. An example is shown in Figure 7.1. The ε martensite appears as thin parallel lines with dark contrast inside the γ-austenite grains. Stress-induced ε- martensite appears as thin martensite plates randomly distributed through the sample.

The images for 2 and 4 % deformation are indistinguishable. Starting from 6% deformation the number of ε martensite plates are increasing with a pronounced increase for the 10 % deformation, where thick white bands of martensite become clear. It was possible with this etchant to observe the different orientations of ε- martensite plates inside the austenite grains. Also, at the high deformation orders, the α'- phase is formed through the intersections of the ε martensite plates. The presence of α′- martensite increases with increasing deformation [4, 5]. It's possible to make an estimation for the ε martensite phase by the OM micrographs and to compare with the X-ray data shown in Figure 7.2.

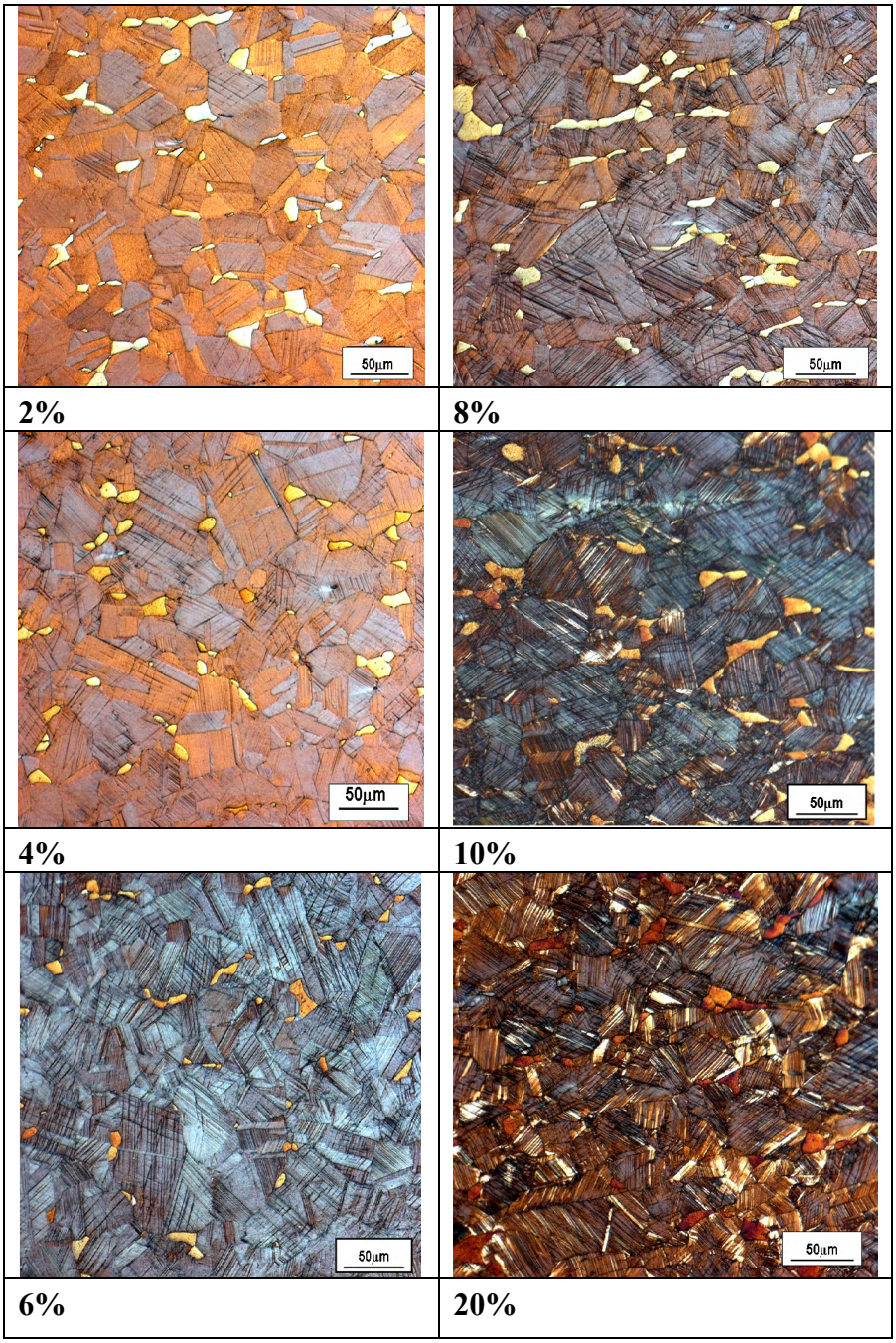

Figure 7.1 OM images of FeMnSiCrNiC for different deformations

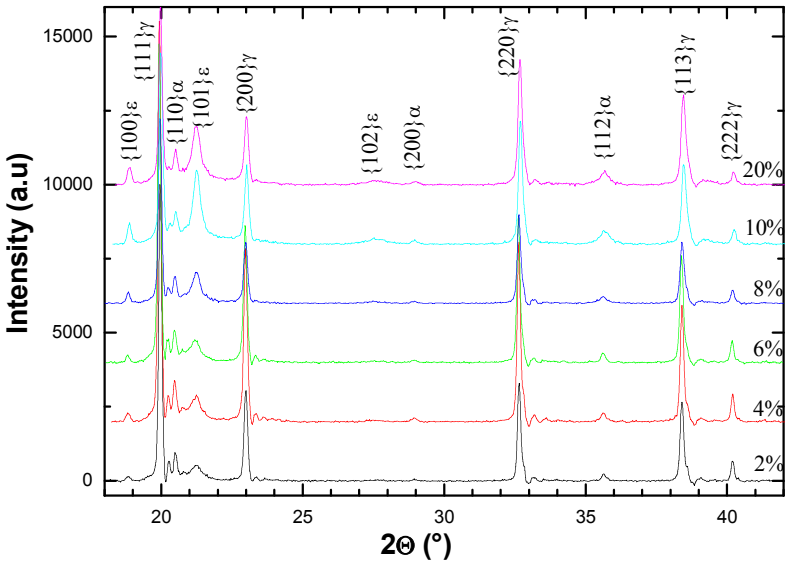

Figure 7.2 XRD spectra of FeMnSiCrNiC for different deformations

Figure 7.2 confirms that there is an increase in the intensity of the ε martensite with increasing deformation up to 10% deformation. After 10% there is no significant increase in the ε martensite, which can be attributed to the increase of the α' phase formed in the intersections of the ε martensite plates [6, 7]. The α' martensite has a blocking effect on the reversion of ε martensite and in addition reverts directly to the austenite, $\alpha \rightarrow \gamma$. This causes a decrease in the SME. Tomota and Yamaguchi [8] showed that a volume fraction of α' martensite below about 4% deformation does not interfere with the extent of the SME.

7.3.2 Slow positron beam Doppler Broadening analysis

The S parameter can be written as

$$S = \sum_i P_i S_i + \sum_i P_{d_i} S_{d_i} \qquad (7.1)$$

Where P_i is the probability of the annihilation of positrons in phase i and S_i is the respective line shape parameter. S_{d_i} counts for the part of positrons annihilated due to the defects of phase i with its respective probability P_{d_i} [9]. The phases present are γ, ε and α'.

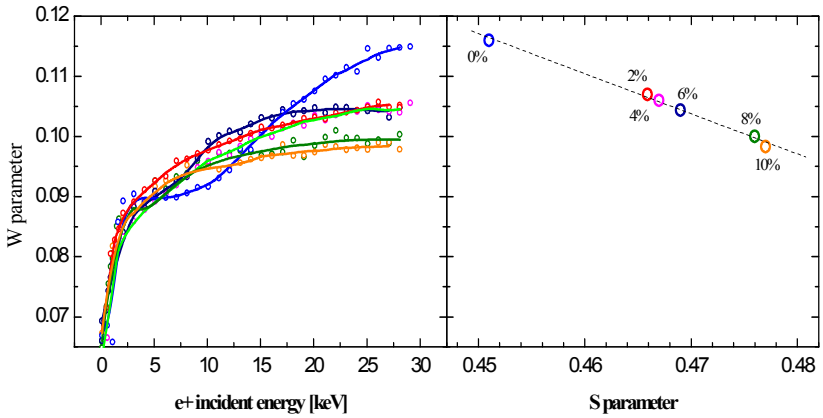

Figure 7.3 The W parameter as a function of incident energy of the implanted positron and the evolution of the bulk line-shape parameters (W, *S*) as a function of deformation

From the data of Figure 7.3, the presence of a subsurface layer in the 0% and 6% samples, probably due to the sample preparation, is visible. The line-shape parameter for the different subsurface layers is comparable but their thicknesses are different. Because the thicknesses of these subsurface layers are not accurately known, a thorough VEPFIT analysis is not feasible and hence only a qualitative indication of the diffusion length is possible. From the shape of the evolution of the W parameter with increasing implantation energy it is clear that the diffusion length starts to decrease for a deformation of 6%. Starting from 6% the evolution of the W parameter with the high energies goes far from the surface towards the bulk faster than the lower deformed samples. This means that the concentration of defects increases with increasing deformation which is correlated with the lifetime data. For a deformation of 8% the line-shape

parameter in the bulk of the sample changes drastically. The evolution of the bulk line-shape parameters (*S,W*) lays on one line indicating that one fraction of the positrons annihilate in the defect free state while the other fraction in one type of defect. The fraction annihilating in the defect increases with higher deformation.

7.3.3 Positron annihilation lifetime measurements

Using the insight gained from the DBAR measurements the lifetime spectra were analyzed by a two component analysis. The results presented in Figure 7.4 indicate a trapping mechanism [10] with a defect lifetime τ_d 153 ± 3ps associated to a dislocation like defect. The defect lifetime intensity increases at 6% deformation, which coincides with the DBAR results. For deformations higher than 10 percent the intensity seems to saturate indicating the concentration of positron detectable defects does not change anymore. Using the trapping model with a trapping efficiency for dislocations in iron, $\mu = 6\times10^{-5}$ m^2s^{-1} [11] a defect concentration could be calculated.

The bulk lifetime can be calculated using equation 4.3 and the values of the lifetime and its intensity which are presented in Figure 7.4. These values are varied randomly between 109ps and 119ps. This implies the trend seen in Figure 7.5 is probably reliable.

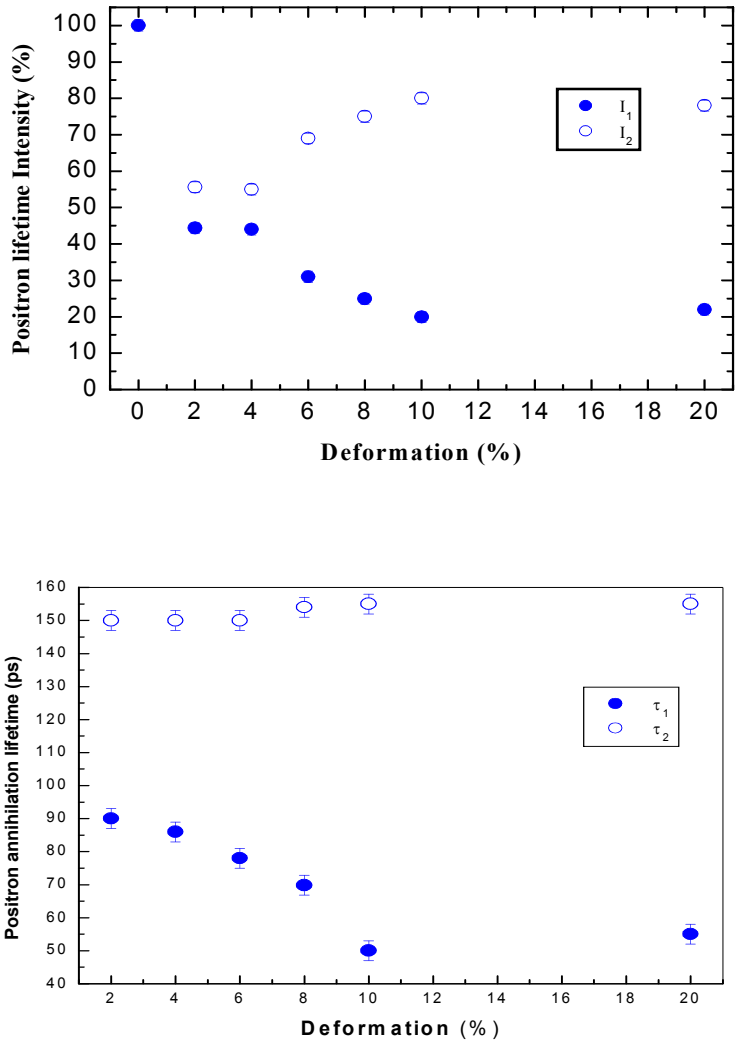

Figure 7.4 Results of the PALS analysis in function of deformation

The evolution of the defect concentration is presented in Figure 7.5.

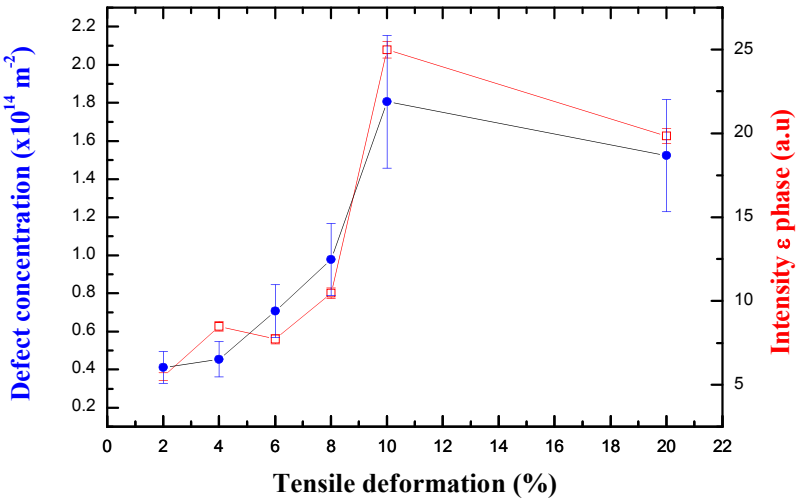

Figure 7.5 Comparison of the defect concentration of the dislocation like defect and the intensity of the ε phase derived from the ε {100} XRD peak.

7.4 Discussions

The evolution of the positron detectable defects were compared with the martensitic γ/ε transformation in the samples by deriving the intensity of the ε {100} phase from the XRD measurements. The result is also presented in Figure 7.5. It is clear from the comparison that there is a very strong correlation between the dislocation like defects and the martensite phase. This is in agreement with [12] where it was concluded from high resolution electron microscopy (HRTEM) that the martensitic transformation is achieved by propagation of a correlated distribution of glide dislocations. Also they said that the thickness of the ε martensite increase with increasing deformation and the ε -phase densification is

achieved by nucleation of new thin plates rather than by thickening of those already formed.

There are few previous publications show the calculation of the dislocations density in iron based alloys using different techniques, such as TEM or the XRD. J. Pesicka et al. [13] studied the dislocation density in the two tempered martensite ferritic steels during heat treatment and creep using TEM and XRD. They said that TEM can help to measure lower dislocation densities; in contrast, the XRD method becomes less reliable when line broadening is not very pronounced (lower dislocation densities). They concluded that long term tempering and creep of these materials is characterized by a decrease of dislocation density; but dislocation densities are still high as compared to other metals. Normal tempering results in a decrease of dislocation density by almost a factor of ten. The mean value dislocation density was in between around 10^{14}. J. Bouquerel et al. [14] reported the density of dislocation in bainitic ferrite to be $10^{13}m^{-2}$.

7.5 Conclusions

Combining DBAR and PALS analysis, the defect structure of deformed FeMnSiCrNiC samples were investigated. Above 4 % deformation the intensity of dislocation-like defects starts to increase, saturating at 10%. The evolution of the positron detectable defects correlates with the presence of the ε martensite phase. Positrons indirectly probe the γ/ε phase transition in FeMn SMA by probing the correlated dislocations.
From all the experimental results shown above, one can says that positron annihilation spectroscopy seems to be a sensitive technique that can be used to detect, classify and calculate the defect concentration.

7.6 References

[1] I. C. Noyan and R. B. Cohen, Residual Stress Measurements by Diffraction and Interpretation, Springer-Verlag, New York 1987.

[2] F. A. Selim, D.P. Wells, J. F. Harmon, J. Kwofie, A. K. Roy, T. White and T. Roney, Advances in X-ray Analysis, 46, (2003) p.106.

[3] J. De Baerdemaeker, J. Colaux, G. Terwagne, C. Dauwe, J. Rad. Phys. Chem. 68, (2003) p.605.

[4] W. Y. Jang, Q. Gu, J. V. Humbeeck, L. Delaey, Mat. Charact. -35, (1995) p.67.

[5] J. Otubo, P.R. Mei, S. Koshimizu, A.H. Shinohara, C.K. Suzuki, Mat. Sci. Eng. A273, (1999) p.533.

[6] K. Ogawa, S. Kajiwara, Mater. Trans. JIM 34, (1993) p.1169.

[7] Y. K. Lee, S. H. Baik, J.C. Kim, C. S. Choi, J. Alloys and Compounds 355, (2003) p.10

[8] Y. Tomota and K. Yamaguchi, J. Phys. France IV 5, (1995) C8–421.

[9] J. Van Humbeeck, G. Ghosh, L. Delaey, D. Segers, M. Dorikens, L. Dorikens Vanpraet, "Positron annihilation in the proceeding of the ICPA8 Conference" (1989) p.395.

[10] M. Bertolaccini, A. Dupasquier, Phys. Rev. B. 1, (1970) p.2896.

[11] Y. K. Park, J. T. Waber, M. Meshii, C. L. Snead, Jr., and C. G. Park, Phys. Rev. B 34, (1986) p. 823.

[12] J. L. Putaux and J. P Chevalier, J. Acta Mater, 44- 4, (1996) p.1701.

[13] J. Pesicka, R. Kuzel, A. Dronhofer and G. Eggeler Acta Materialia 51 (2003) p.4847.

[14] J. Bouquerel, K. Verbeken, and B. C. De Cooman. J. Acta Materialia 54, (2006) p.1443.

Chapter 8

Study of the effect of annealing on defects in FeMnSiCrNiC alloys by slow positron beam measurements

In this chapter the effect of isochronal annealing on a deformed FeMnSiCrNiC alloy is studied using a Variable-energy (0– 30 keV) positron beam experiment. Doppler broadening profiles of the positron annihilation as a function of the incident positron energy were shown to be quite sensitive to defects introduced by deformation. The variations of the nature and the concentration of defects are studied as a function of the isochronal annealing temperature. These results are correlated with the data obtained with the positron annihilation lifetime spectroscopy (PALS). The positron annihilation results are compared with XRD and optical microscopy (OM).

8.1 Introduction

The Shape Memory Alloys (SMAs) are metallic materials, which have the ability to return to some previously defined shape when subjected to the appropriate thermal procedure. These materials can be plastically deformed at some relatively low temperature, and upon exposure to some higher temperature they will return to their shape prior to the deformation. The shape memory effect (SME) for FeMnSi based alloys arises from the reverse transformation of stress-induced ε martensite (HCP structure) into γ austenite (FCC structure) upon heating [1] by the movement of Shockley partial dislocations. There has been a considerable amount of research conducted on the FeMnSi system, and this research has led to a maximum measured recoverable strain of ~5% [2], but this value is significantly lower than the recoverable strains possible in NiTi of 8% [3]. A good shape recovery depends strongly on the alloy composition and on the thermo-mechanical treatment of the alloy. The width of martensite plate should be extremely small and must be uniformly distributed [4– 6].

There are efforts to increase the use of these materials, especially the “heat-to-shrink” pipe couplings [7]. The fitting technique by using FeMnSi based shape memory alloys is a brand-new method to connect engineering pipes. It exhibits much merit than conventional welding and can be widely applied in various engineering fields.

Positron annihilation spectroscopy (PAS) is a useful technique to study defects in materials [8, 9]. From this point of view, it can be used for the calculations of the density of defects (vacancies and dislocations) and the detection of defect recovery after the annealing of deformed SMAs. The phase transition temperatures for the SMAs can be detected using the PAS. A number of positron annihilation studies have dealt with the interaction of positrons with dislocations in metals and alloys [10, 11]. S. Hautakangas et al. [11] concluded that the positrons are sensitive only to plastic deformation i.e. generation of dislocations and other open volume defects, while the detection of the elastic deformation is obscured not only by a small increase in dislocation density at low strain values (< 2.3%), but also by experimental scattering and stability of set up (in-situ measurements).

8.2 Experimental work

The chemical composition of the FeMnSiCrNiC alloy is given in Table 7.1(the previous chapter).

After deformation by tensile loading (2% up to 20%), the specimens were cut, mechanically polished and then electrolytically polished in a solution of 20% perchloric acid and 80% butylcellosolve. The samples were employed to perform the positron annihilation measurements at room temperature, and then were isochronally annealed for 15 minutes from 100 °C to 500 °C. After each annealing the samples are measured by the different techniques (positron annihilation life time, the slow positron beam, OM and the XRD). It is used to start the XRD and the positron annihilation measurements before the OM. This is because the samples prepared for the OM should be color etched.

8.3 Results and discussion

8.3.1 Positron annihilation lifetime

In this work we investigate the effect of annealing on the deformation-induced defects and on phase transition using the positron annihilation techniques. Different deformed FeMnSiCrNiC samples (2 up to 20% tensile deformation) were annealed isochronally (15 minutes) at 100°C in boiling water and from 200°C up to 500°C in steps of 100°C in an evacuated furnace. The positron-lifetime spectra were analyzed using two components. The lifetime for the trapped positrons has a value around 150 ps. This value is shorter than that for positrons trapped in vacancies, which is 180 ps [12]. This value is attributed to positron annihilation from dislocations [13].

The temperature dependence of the mean value of the positron annihilation lifetime τ_{mean} for the 2% deformed sample is shown in Figure 8.1. A decrease of τ_{mean} with increasing annealing temperature is observed. This is attributed to the decrease of the defect concentration with increasing temperature. Only one positron lifetime (τ_1) component can be extracted after annealing at 500°C for the 2 % deformation. This value is 107 ps, which is the same value for the sample before deformation. This means that the 2% deformation sample has almost no defects or ε phase at 500 °C. The positron annihilation lifetime and its intensity data at the different annealing temperatures can be used to calculate the density of dislocations for every annealing temperature.

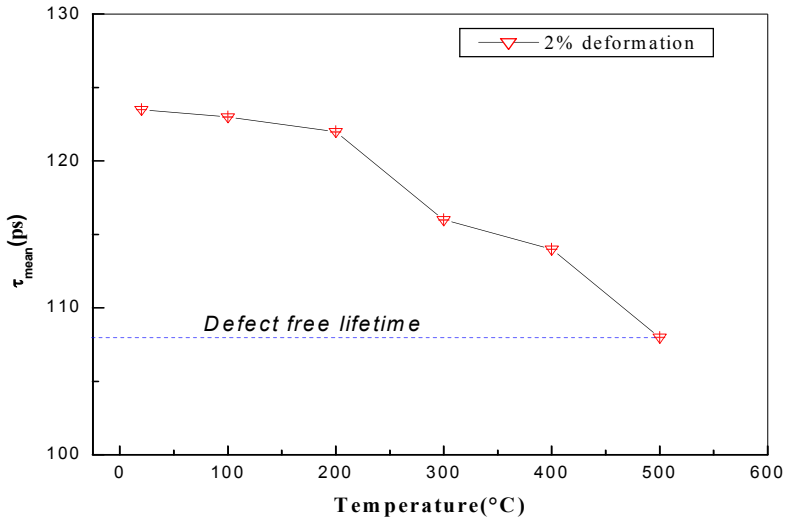

Figure 8.1 Temperature dependence of the mean value of the positron annihilation lifetime of the 2% deformed sample(the samples were annealed in a boiling distilled water for 15 minute and then start from 200°C up to 500°C in steps of 100°C in high vacuum furnace.

In chapter 7 it was shown that there is an increase of the concentration density with increasing the degree of deformation (see Figure 7.5). Figure 8.2 shows the positron annihilation mean lifetime (τ_{mean}) and the defect concentration of different deformation FeMnSiCrNi-C samples annealed at 500°C. Also the positron annihilation lifetime τ_1 and its intensity are shown also in this figure. Starting from the 6% deformation a long component of lifetime τ_2 is found to be around 150ps which is related to existence of the dislocations. Figure 8.2 shows that annealing of the samples at 500°C leads to a significant decrease of the defect concentration (see Figure 7.5 for comparison). For the low deformed samples (2, 4%) annealed at 500°C, most of the positrons annihilate in the defect free lattice, giving a lifetime near to 107 ps. This means that, the samples deformed for 2 and 4%, are almost free of defects after the annealing at 500°C. For the samples deformed for more than 4%, the τ_{mean} is higher than 107 ps. This means that these samples still have defects after annealing at 500°C.

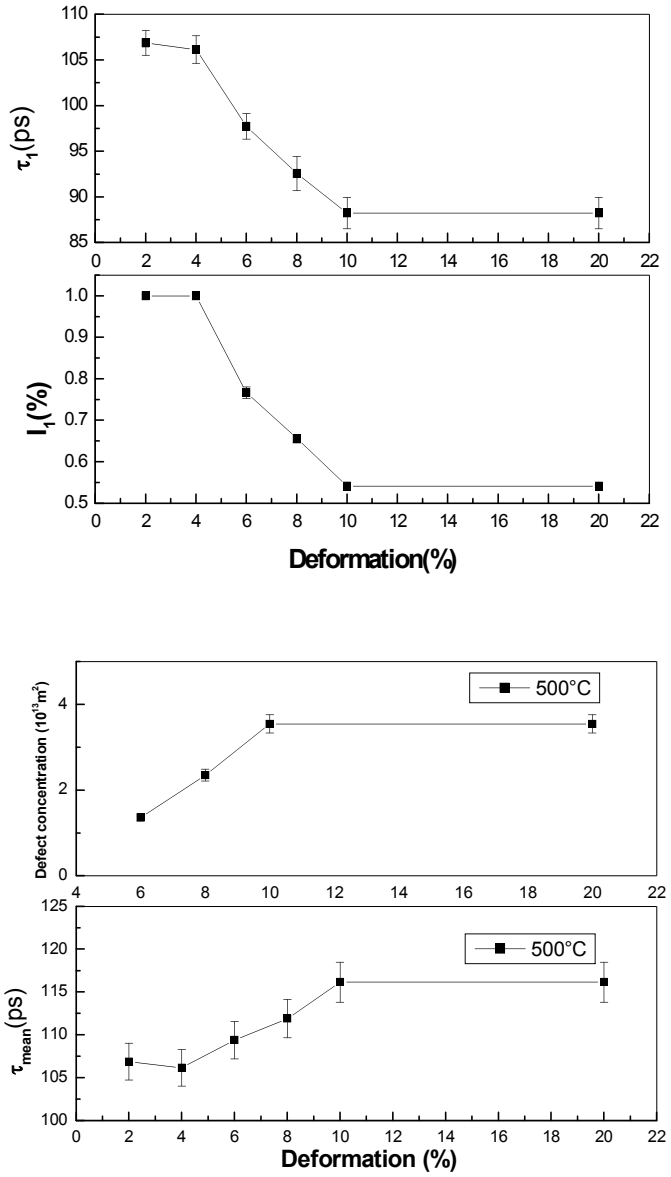

Figure 8.2 The positron annihilation lifetime parameters and the defect concentration of different deformation FeMnSiCrNi-C samples annealed at 500°C.

8.3.2 Slow positron beam Doppler Broadening analysis

Figure 8.3a shows the evolution of the S parameter as a function of the incident energy of the implanted positrons for the undeformed, the 2% and 20% deformed samples, before and after annealing at 500°C. It seems that there is no subsurface layer for most of the samples. From the shape of the evolution of the S parameter with increasing implantation energy, it is concluded that the diffusion length is slightly shorter for the samples deformed for 20% than for the samples deformed for 2%. This could support the idea that the 20% sample still has defects. The S parameter value at high positron implantation energy (28 keV) slightly increases with increasing deformation. The effect of annealing can be clearly observed. A defect free sample (its positron lifetime is 107 ps) is measured in the beam to be used as a reference sample. At the annealing temperature of 500°C, the value of the S parameter at high positron implantation energy (28 keV) decreases after the annealing. It seems that after annealing at 500°C the sample deformed to 2% is almost defect free compared to the 20% deformation sample. The value of the S parameter for the sample deformed to 20% at the high positron implantation energy (28 keV) is much higher than the defect free sample (reference sample), which means that the sample still has defects.

Figure 8.3b shows the evolution of the line shape parameters (S, W). This indicates that one fraction of the positrons annihilate in the defect free state (low S, high W) while the other fraction in defects (high S, low W). The annihilating fraction in defects increases with increasing of deformation and decreases at the high temperature annealing (500°C).

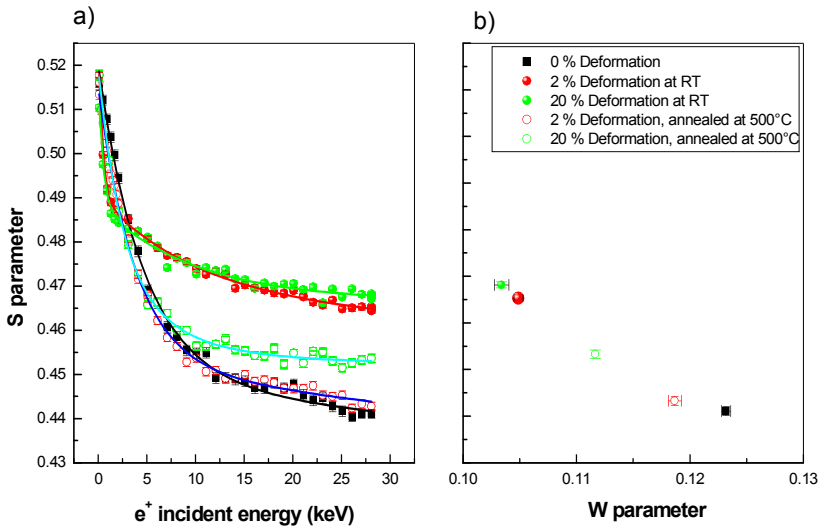

Figure 8.3 a) The S parameter as a function of the incident energy of the implanted positrons for the 2%, 20% deformation before and after annealing at 500°C. A defect free sample is measured as a reference sample and **b)** the evolution of the line-shape parameters (W, S) for low and high deformed material before and after annealing at 500°C.

8.3.3 OM and XRD

To determine the type of defects, optical microscopy and XRD were performed on the 2% and 20% deformed samples, before and after annealing at 500°C. Figure 8.4 (a - c) shows the microstructure of the undeformed sample (Figure 8.4a) and two deformed FeMnSiCrNiC samples (Figure 8.4b for the 2% and Figure 8.4c for the 20% deformation) after annealing at 500°C for 15 minutes.

Deformation of 2% and 20% results in the stress-induced transformation of austenite to ε martensite. The ε martensite appears as thin parallel lines with dark contrast inside the austenite grains. Increasing stress induces the appearance of large ε domains. During annealing at high temperatures, the reverse ε martensite

to austenite phase transformation occurs. The 2% deformed sample has almost no ε phase after annealing at 500°C (Figure 8.4b). If the deformation is small (not more than 4%), the reverse movement of the Shockley partials is not impeded because only primary ε variants move through the parent austenite under the influence of stress. The microstructure of the 20% deformed samples still contains ε martensite (Figure 8.4c). When the strain is large, several ε variants will be activated and the intersection of ε plates will impede the back movement of the partials. In addition, the plastic deformation of the austenite will be initiated at higher strains, such as 20%. The presence of dislocations in the parent phase prevents the free motion of the interface. This influence of the amount of pre-strain was also described before in [14- 16].

The XRD results (Figure 8.5) confirm what is seen in the optical microstructure. The intensity of the (002)ε, (100)ε peaks is higher for the 20% deformed samples compared to the one of the 2% deformation. The 2% deformed sample has almost no ε phase after the annealing at 500°C. The 20% deformed sample still has ε martensite phase.

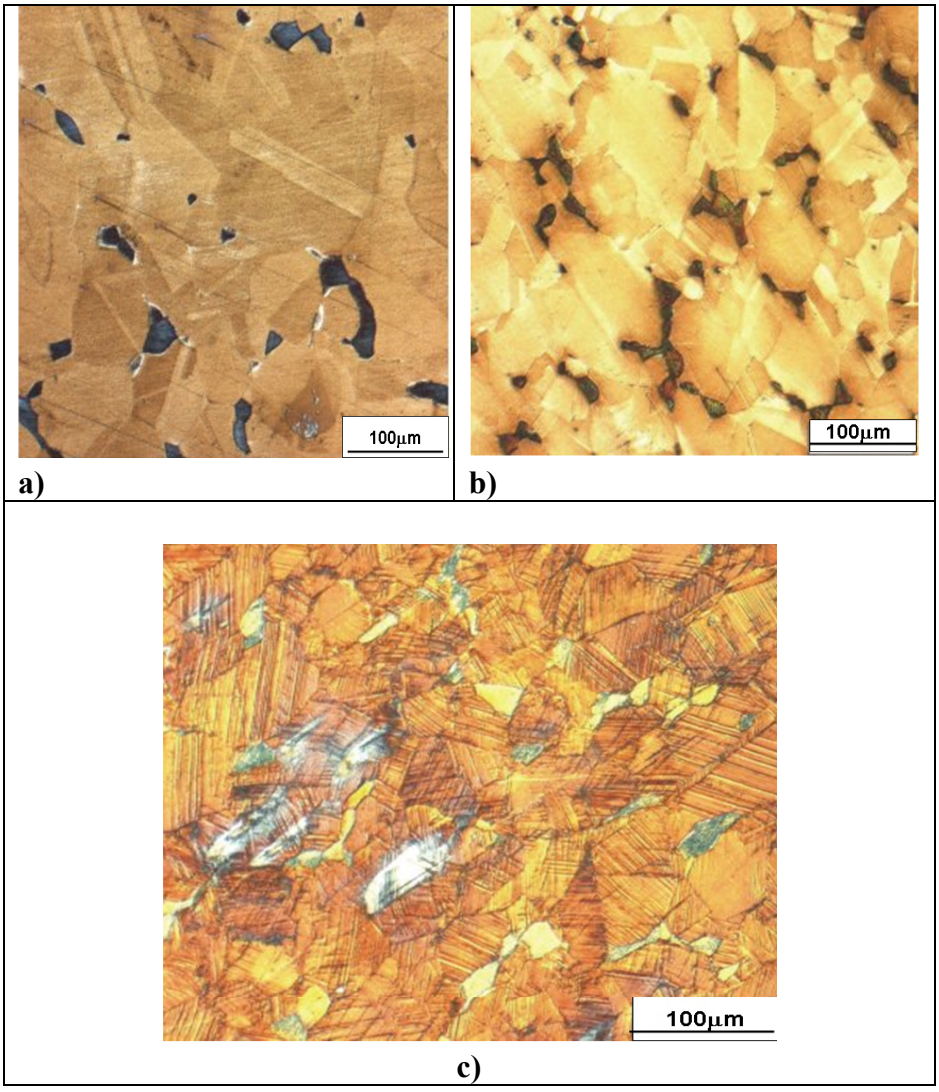

Figure 8.4 OM images of FeMnSiCrNiC **a)** 0 % deformation, **b)** 2 % and **c)** 20% deformation annealed at 500°C

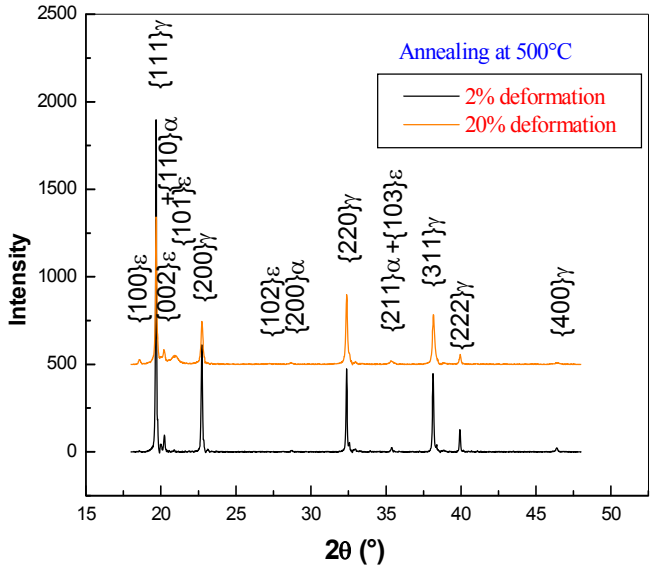

Figure 8.5 XRD spectra for 2 % and 20% deformation annealed at 500°C.

Figure 8.6 (a, b) shows the XRD data for the 4% and 10% FeMnSiCrNi-C deformed samples at room temperature, and after the isochronal annealing at 500°C. The intensity of the (002)ε, (100)ε peaks is higher for the 10% deformation compared to the one of the 4% deformation. The 4% deformed sample has almost no ε phase at 500°C (Figure 8.6 b) while the 10% deformation sample still have a significant amount of the ε martensite phase.

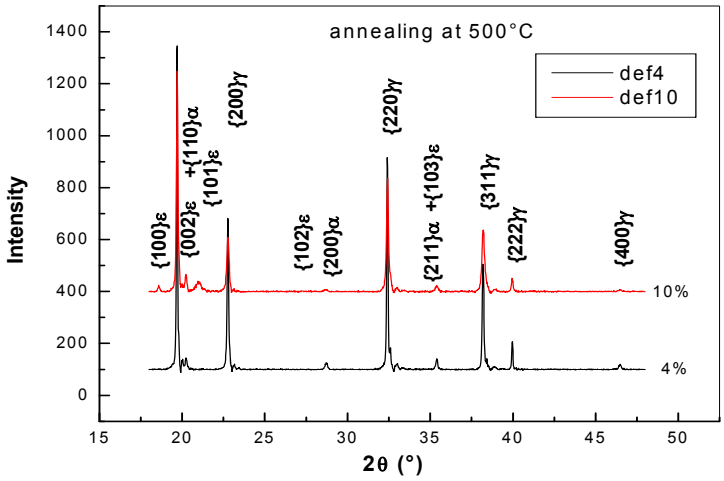

a)

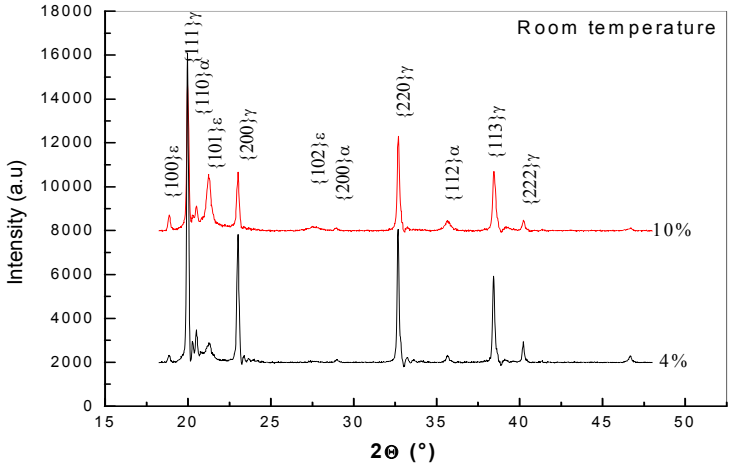

b)

Figure 8.6 (a, b) XRD spectra for 4 % and 10% deformation **a)** annealed at 500°C, **b)** at room temperature.

8.4 Conclusions

The FeMnSiCrNiC SMA, subjected to plastic deformation by tensile loading at different levels was studied by OM, XRD and positron annihilation techniques. The effect of the isochronal annealing was studied. The OM, and XRD measurements show that the reversion of the ε martensite to the γ phase is low for the 10 and 20% deformation after annealing at 500°C, although the number of large ε phase domains clearly decreases. This morphology is a result of the incomplete reversion of large ε domains. The 2% and the 4% deformed samples have almost no ε phase after annealing at 500°C. The positron annihilation mean lifetime τ_{mean} and the Doppler broadening line-shape parameters show a decrease of the defect concentration with increasing annealing temperature. In case of the 20% deformed sample, the value of the S parameter is higher than the one for the defect free sample. This means that the 20% deformed samples still have defects. The τ_{mean} and the S parameter for the 2% deformation after annealing at 500°C have almost the same value as the 0% deformation sample.

8.5 References

[1] A. Sato, E. Chishima, K. Soma, T. Mori, Acta Metall.30, (1982) p.1177.

[2] D.P. Dunne, H. Li, J. Phys. IV 5, (1995) C8415.

[3] K. Otsuka, C.M. Wayman (Eds.), Shape Memory Materials, Cambridge University Press, (1998).

[4] S. Kajiwara, Mater Sci Eng A 67, (1999) p. 273.

[5] Ogawa K, Kajiwara S. Mater Trans JIM 34 (1993) p. 1169.

[6] Kajiwara S, Ogawa K. Mater Sci Forum 2000, 327–328:211.

[7] H. Tanahashi, T. Maruyama and H. Kubo, Trans. Mater. Soc. Jpn., 18B, (1994) p.1149.

[8] Positrons in solids, edited by P. Hautojarvi (Springer- Verlag, Berlin, 1979).

[9] Positron solid State Physics, edited by W. Brandt and A. Dupasquier (North-Holland, Amsterdam, 1983).

[10] Y. K. Park, J. T. Waber, M. Meshii, Jr., C. L. Snead and C. G. Park, Phys. Rev. B 34, (1986) p.823.

[11] S. Hautakangas, H. Schut, S. van der Zwaag, P. E. J. Rivera Diaz del Castillo, and N. H. van Dijk, phys. stat. sol. (c) 4, No. 10, (2007) p.3469.

[12] G. Kuamoto, Y. Asano, M. Takanaka, and K. Kitajimi, J. Phys. Soc. Jpn., 53, (1983) p.1098.

[13] C. Hidalgo, S. Linderoth and N. de Diego, Phil.Mag. A64, (1986) p. L61

[14] T. Shiming, Y. Shiwei, Scr. Metall. Mater. 27, (1992) p. 229.

[15] H. Inahaki, Z. Metallkd. 83, (1992) p.90.

[16] N. Van Caenegem, L. Duprez, K. Verbeken, B.C. De Cooman, Y. Houbaert and D. Segers, ISIJ Int., 47-5, (2007) p.723.

Chapter 9

General conclusions

9.1 Introduction

This chapter gives an overview of the very important conclusions included in each chapter of this thesis, and also a proposal of the future work concerning the field of iron based alloys and positron annihilation spectroscopy will be discussed.

9.2 General conclusions

The positron annihilation techniques can be used to classify the types of defects and also it can be used to calculate the defect concentration. For the high deformed iron (chapter 4), the isochronal curve for the positron mean lifetime reveals that the traps for positrons are dislocations. With increasing the annealing temperature, the Doppler broadening parameter *S* has a slight decrease before the recovery temperature region. The S-W relation shows only one straight line, which means that only one type of defect, exists in the deformed iron through the whole isochronal annealing temperature range, which is consistent with the positron lifetime data.

A study of defects induced in FeSi which is deformed at high temperature and low (room) temperature was done by positron annihilation spectroscopy (PAS) (chapter 5). The effect of the Si content is also studied. The data of the positron annihilation techniques shows that the deformation temperature affects the concentration and the type of defects formed in the alloys through the deformation process. Mono-vacancies are the main defects formed when the

alloys are deformed at high temperatures. In case of the alloys deformed at room temperature, dislocations and vacancy clusters are formed.

In chapter 6 the influence of the addition of C to the FeMnSiCrN base material is investigated at room temperature. Steel samples were deformed during a tensile experiment up to a strain of 17 %. Light optical microscopy (OM) and XRD gave information about the different microstructural phases that exists in the deformed and the undeformed alloys. From the results of the positron annihilation, the Doppler broadening parameter *S* increases as a result of the trapping of positrons in defects. In the early stages of deformation, no significant increase of the S parameters for both alloys is observed. The increase of *S* is caused by an increasing number of lattice defects (dislocations). The starting of saturation of the *S* parameter corresponds to the equilibrium defect density. Phase transition might be detected from the *S*-*W* relation. The carbon content in the alloys has a significant effect in the value of the *S* parameter, which means a change in the concentration of defects.

The martensitic transformation and defects induced by the deformation of a FeMnSiCrNiC alloy were investigated (chapter 7). Samples deformed from 2 to 20% were investigated using positron annihilation spectroscopy, optical microscopy (OM) and X-ray diffraction (XRD). It has been found that above 4% deformation the concentration of dislocation like defects starts to increase, and saturation after 10% tensile deformation was found. The evolution of the positron detectable defect (the defect concentration and its size) correlates with the presence of the ε martensite phase. Positrons indirectly probe the γ/ε phase transition in FeMn SMA by probing the correlated dislocations.

In chapter 8, the effect of isochronal annealing on a deformed FeMnSiCrNiC alloy is studied using a Variable-energy (0–30 keV) positron beam. Doppler broadening profiles of the positron annihilation as a function of incident positron energy were shown to be quite sensitive to defects introduced by deformation. The variation of the nature and concentration of defects is studied as a function of isochronal annealing temperature. The OM and XRD measurements show that

the reversion of the ε martensite to the γ phase is low for the 20% deformed sample annealed at 500°C, although the number of large ε phase domains clearly decreases. This morphology is a result of the incomplete reversion of large ε domains. The 2% deformed sample has almost no ε phase after annealing at 500°C. The positron annihilation mean lifetime τ_{mean} and the Doppler broadening line-shape parameters show a decrease of the defect concentration when increasing the annealing temperature in both samples. The τ_{mean} and the S parameter for the 2% deformation after annealing at 500°C have almost the same value as the 0% deformed sample. This can be an indication that the 2% deformed sample is almost recovered at 500°C.

From all the conclusions discussed, it is clear that the positron annihilation spectroscopy is a sensitive technique can be used to detect and classify the kind of defects. Also it is a unique technique to calculate the defect concentration. This is very important to the industry, where the positron annihilation is also sensitive to the nano-cracks. The slow positron beam can visualize the differences between the surface and the bulk material. This is very important for the FeSi to be sure of the EBSD results. Also can give an answer for the question about the ε–martensite can be seen by the optical microscopy, if it is only on the surface or it is related to the bulk.

9.3 Suggestions for future work

9.3.1 FeMnSiCrNi shape memory alloys

The quantification of the ε– martensite phase induced by deformation in these alloys still needs more work to have a complete and clear image about this phase. It is clear from the comparison of the data shown in chapter 7, that there is a correlation between the dislocation like defects calculated from the positron annihilation lifetime parameters and the ε-martensite phase identified by the XRD. What should be done is doing more measurements for a set of deformed samples and trying to make the correlation between the XRD, high resolution TEM and the positron annihilation results.

It should be taken into account that the stress-induced ε–martensite exists in different variants. For this reason the high resolution EBSD could be also a good method to do more research on that. The effect of the surface treatments on the first micron of the sample should be given more attention. The slow positron beam can help to have information about the effect of the different surface treatments. It was clear that the defect concentration in FeMnSiCrNiC samples decreases with increasing temperature. A further annealing for the high deformed samples up to 1000°C needed to have an idea about those highly deformed samples. The positron annihilation spectroscopy could be used to determine the phase transition temperature. Also the electrical resistivity (four-point probe method) is a simple experiment can do that.

9.3.2 FeSi electrical steel

The positron annihilation data in chapter 5 shows that the Si content affects the positron annihilation parameters, but the number of samples used in this study was not enough to have clear idea about the microstructure change. More different Si content samples should be examined by PAS and correlate the results with a high resolution TEM measurements.

Appendix

Trapping Models

1 Simple trapping model

1.1 General Case

The simple trapping model (STM) [1] is based on the following assumptions:

- At time $t = 0$ all positrons are free
- The positron trapping rate κ is proportional to the defect concentration:

  $$\kappa = \mu_D c_D \qquad (1)$$

  where μ_D is the defect specific trapping coefficient.
- The positron may escape from a trap. The de-trapping rate is denoted by δ.

Supposing N different defects, we can make the following set of differential equations:

$$\begin{cases} \dfrac{dn_B}{dt} = -(\lambda_B + \sum_{j=1}^{N} \kappa_j)\, n_B + \sum_{j=1}^{N} \delta_j n_{Dj} \\ \dfrac{dn_{Dj}}{dt} = \kappa_j n_B - (\lambda_{Dj} + \delta_j)\, n_{Dj} \end{cases} \qquad (2)$$

where $n_B(t)$ and $n_{Dj}(t)$ are the probabilities that the positron is in the free state and defect state, and λ_B and λ_{Dj} are the annihilation rates from the free and trapping state. The boundary conditions are:

$$n_B(0) = 1,\ n_{Dj}(0) = 0 \qquad (3)$$

The probability for a positron to be alive at time t is given by:

$$n(t) = n_B(t) + \sum_{j=1}^{N} n_{Dj}(t) = \sum_{i=1}^{N+1} I_i \exp(-\lambda_i t) \qquad (4)$$

where the decay constants λ_i and I_i are found by solving eq. 2. The lifetime spectrum is the probability for annihilation at time t:

$$-\frac{dn(t)}{dt} = \sum_{i=1}^{N+1} I_i \lambda_i \exp(-\lambda_i t) \qquad (5)$$

From equation 5 one can calculate the average positron lifetime:

$$\tau_{av} = \int_0^{\infty} (-\frac{dn(t)}{dt})\, t\, dt = \int_0^{\infty} n(t)\, dt = \sum_{i=1}^{N+1} I_i \tau_i \quad (6)$$

In the case of no de-trapping ($\delta_j=0$) the general solution can be written as:

$$\lambda_1 = \lambda_B + \sum_{j=1}^{N} \kappa_j \quad (7)$$

$$\lambda_{i+1} = \lambda_{Di} \quad (8)$$

$$n(t) = [1 - \sum_{j=1}^{N} \frac{\kappa_j}{\lambda_B - \lambda_{Dj} + \Sigma\kappa}] e^{-(\lambda_B + \Sigma\kappa)t} + \sum_{j=1}^{N} \frac{\kappa_j}{\lambda_B - \lambda_{Dj} + \Sigma\kappa} e^{-\lambda_{Dj} t} \quad (9)$$

The annihilation rate from the free state is given by:

$$\lambda_B = \sum_{i=1}^{N+1} I_i \lambda_i \quad (10)$$

The fraction of positrons annihilating form the free and trapped state is given by:

$$\eta_B = \int_0^{\infty} \lambda_B n_B(t) dt \quad (11)$$

And

$$\eta_{Dj} = \int_0^{\infty} \lambda_{Dj} n_{Dj}(t) dt \quad (12)$$

This gives in the case of no de-trapping:

$$\eta_B = \frac{\lambda_B}{\lambda_B + \Sigma\kappa} \quad (13)$$

$$\eta_{Dj} = \frac{\kappa_j}{\lambda_B + \Sigma\kappa} \quad (14)$$

1.2 One type of defect

In this case we get two annihilation rates:

$$\lambda_1 = \lambda_B + \kappa \quad (15)$$

$$\lambda_2 = \lambda_D \quad (16)$$

The following relations can be calculated

$$\lambda_B = I_1 \lambda_1 + I_2 \lambda_2 \quad (17)$$

$$\tau_{av} = \frac{1 + \kappa\tau_D}{1 + \kappa\tau_B} \tau_B \quad (18)$$

$$\lambda_1 = \frac{1}{I_1}(\lambda_B - I_2\lambda_D) \quad (19)$$

$$\kappa = \frac{I_2}{I_1}(\lambda_B - \lambda_D) \quad (20)$$

The validity of the trapping model can be tested by comparing $I_1 \lambda_1 + I_2 \lambda_2$ with the free annihilation rate according to equation 17.

1.3 Two types of defects

A quantitative analysis of annihilation characteristics in terms of positron trapping rates and defects concentration is made using the so-called two state trapping model [2, 3].

The following annihilation rates are found:

$$\lambda_1 = \lambda_B + \kappa_1 + \kappa_2, \qquad I_1 = 1 - I_2 - I_3 \quad (21)$$

$\lambda_2 = \lambda_{D1}$,

$$I_2 = \frac{\kappa_1}{\lambda_B - \lambda_{D1} + \kappa_1 + \kappa_2} \quad (22)$$

$\lambda_3 = \lambda_{D2}$,

$$I_3 = \frac{\kappa_2}{\lambda_B - \lambda_{D2} + \kappa_1 + \kappa_2} \quad (23)$$

A few cases can be distinguished:

Case1. If $\kappa_{1,2} >> \lambda_B - \lambda_{D1,2,}$ positron trapping is in saturation. All positrons annihilate in defects and the sensitivity to defects concentrations is lost. From the experiment we get only two lifetime components $\tau_{1,exp}$ and $\tau_{2,exp}$ with

$$\frac{1}{\tau_{1,\exp}} = \lambda_{D1} \quad (24)$$

$$\frac{1}{\tau_{2,\exp}} = \lambda_{D2} \quad (25)$$

$$\frac{I_{1,\exp}}{I_{2,\exp}} = \frac{\kappa_1}{\kappa_2} \tag{26}$$

Case2. Suppose that the two shortest components cannot be separated. In this case one also gets only two components with:

$$\tau_{1,\,exp} = \frac{I_1}{I_1 + I_2}\,\tau_1 + \frac{I_2}{I_1 + I_2}\,\tau_2 \tag{27}$$

$$\frac{1}{\tau_{2,\exp}} = \lambda_3, \qquad I_{2,\,exp} = I_3 \tag{28}$$

From this we can calculate the trapping rates:

$$\kappa_1 = \frac{\tau_{1,\exp}\,(\lambda_B - I_{2,\exp}\,\lambda_{D\,2}) - I_{1,\exp}}{\tau_{D\,1} - \tau_{1,\exp}} \tag{29}$$

$$\kappa_2 = \frac{I_{2,\exp}}{I_{1,\exp}}\,(\lambda_B - \lambda_{D2} + \kappa_1) \tag{30}$$

Case3. The two longest components λ_{D1} and λ_{D2} are mixed up (e.g. in semiconductors one can have a vacancy existing in two different charge states having two lifetimes differ only by 5-10%. We get:

$$\frac{1}{\tau_{1,\exp}} = \lambda_1 = \lambda_B + \kappa_1 + \kappa_2 \tag{31}$$

$$\tau_{2,\,\exp} = \frac{I_2}{I_2 + I_3}\,\tau_{D1} + \frac{I_3}{I_2 + I_3}\,\tau_{D2} \tag{32}$$

If $\lambda_B - \lambda_{D1,\,2} << \kappa_1 + \kappa_2$ then

$$\tau_{2,\,exp} = \frac{\kappa_1}{\kappa_1 + \kappa_2}\,\tau_{D1} + \frac{\kappa_2}{\kappa_1 + \kappa_2}\,\tau_{D2} \tag{33}$$

The total trapping rate

$$\kappa_1 + \kappa_2 = \frac{\tau_{av} - \tau_B}{\tau_{2,\exp} - \tau_{av}}\,\frac{1}{\tau_B} \tag{34}$$

can be calculated as if there was only one type of defect with $\tau_\Delta = \tau_{2,\,exp}$.

2 Diffusion trapping model

The space and time dependent positron diffusion equation is given by:

$$\frac{\partial n(r,t)}{\partial t} = D_+ \nabla^2 n(r, t) - \lambda_n(r, t) \qquad (35)$$

with n the position probability, D_+ the diffusion constant and λ the positron annihilation rate. This equation has no general solution and depends on the specific geometry of the problem. We will mention here only a few cases, relevant for this thesis.

In the case of spatially large defects such as voids, the positron trapping coefficient may become so large that the positron diffusion to defects starts to limit the total trapping rate. The switching from transition-limited to diffusion limited trapping was first studied by McMullen [4, 5]. The case of trapping at voids has been studied by Niemimen et al. [6].

A similar approach for positron trapping at grain boundaries in metals was developed by Dupasquier et al. [7, 8]. The model is based on the following assumptions:
a) the material is formed by identical spherical domains with a radius R,
b) positron trapping occurs only at the surface of the domains with a thickness $\delta << R$,
c) the thermal trapping rate κ at the surface is much larger than the local annihilation rate of free positrons,
d) de-trapping is negligible and
e) all trapped positrons annihilate with the same rate λ_{trap}.
It is also assumed that the positron motion is governed by diffusion with a characteristic diffusion length L_+ related to the positron diffusion constant D_+ by:

$$L_+ = \sqrt{\frac{D_+}{\lambda_{bulk}}} \qquad (36)$$

Using these assumptions the solution of the space and time dependent diffusion equation leads to a lifetime spectrum with an infinite number of components and is given by the equation:

$$f(t) = \sum_{n=1}^{\infty} I_n \lambda_n e^{-\lambda_n t} + I_B \lambda_B e^{-\lambda_{trap} t} \tag{37}$$

Where λ_n to be calculated from

$$\lambda_n = \lambda_{bulk} \left(1 + \frac{\beta_n^2 L_+^2}{R^2}\right) \tag{38}$$

With β_n the n^{th} solution of the eigenvalue equation:

$$\beta_n \cot \beta_n + \alpha - 1 = 0 \tag{39}$$

and α is a regime parameter defined by:

$$\alpha = \frac{\delta_{trap}}{L_+} \frac{R}{L_+} \tag{40}$$

with δ_{trap} the effective trapping thickness

$$\delta_{trap} = \frac{\kappa_s \delta}{\lambda_{bulk}} \tag{41}$$

The intensities are:

$$I_n = \frac{\left(\frac{L_+}{R}\right)^2}{1 + \left(\frac{\beta_n L_+}{R}\right)^2} \times \left(\frac{\lambda_{bulk}}{\lambda_n - \lambda_{bulk}} - \frac{\lambda_{trap}}{\lambda_n - \lambda_{trap}}\right) \times \frac{6\alpha^2}{\beta_n^2 + \alpha(\alpha - 1)} \tag{42}$$

References

[1] W, Brandt, in proc. International conference on Positron Annihilation (A. T. Stewart and L. O. Rolling, Eds.), Academic press, New York, 80 (1967).

[2] R. N. West; in "positrons in Solids, series" Topics in Current Physics (12) ed. by P. Hautojarvi, Springer, Berlin 89 (1979).

[3] B. Bergersen, M. J. Stott. Solid State Communic.7, (1969) p.1203.

[4] S. X. McFadden, A. P. Zhilyaev, R. S. Mishra, and A. K. Mukherjee, Observation of low-temperature super-plasticity in electro-deposited ultra-fine grained nickel. Mat. Lett., 45, (2000) p.345

[5] R. K. Islamgaliev, R.Z. Valiev, R. S. Mishra, A. K. Mukherjee. "Enhanced super-plastic properties in bulk metastable nanostructured alloys", Mat. Sci. Eng.A, 304-306, (2001) p.206.

[6] R. M. Nieminen, J. Laakonen. Positron trapping rate into vacancy clusters. Appl. Phys., 20, (1979) p.181.

[7] A. Dupasquier, R. Romero, A. Somoza. Phys. Rev. B, 48, (1993) p.9235.

[8] A. Dupasquier and A. Somoza "Positron diffusion and trapping in fine-grained materials". Mat. Sci. For., (1995) p.175

Publications

1. Study of defects and phase transformation in a Fe-Mn-Si-Cr-Ni alloy by positron annihilation method, K. M. Mostafa, N. Van Caenegem, J. De Baerdemaeker, D. Segers, Y. Houbaert, Physica status solidi (c) 4-10, (2007) p. 3554.

2. Positron annihilation studies in plastically deformed Fe-Mn-Si-Cr-Ni-C, J. De Baerdemaeker, K. M. Mostafa, N. Van Caenegem, D. Segers, Y. Houbaert, Physica status solidi (c) 4-10, (2007) p.3518.

3. Study of the effect of annealing on defects in Fe-Mn-Si-Cr-Ni-C alloy by slow positron beam, K. M. Mostafa, J. De Baerdemaeker, N. Van Caenegem, D. Segers, and Y. Houbaert, J. Applied surface Science, Applied Surface Science 255 (2008) p.145

4. A study of defects in deformed FeSi alloys by using of positron annihilation techniques. K. M. Mostafa, J. De Baerdemaeker, Pablo R. Calvillo, Y. Houbaert, D. Segers, J. Applied Surface Science 255, (2008) p.149

5. A study of defects in iron based alloys by positron annihilation techniques. K. M. Mostafa, J. De Baerdemaeker, P. R. Calvillo, N.Van Caenegem, Y. Houbaert, and D. Segers. J. Acta Physica Polonica A 113- 5 (2008) p.1471.

6. Influence of carbon on the microstructure of a Fe-Mn-Si-Cr-Ni alloy, K. M. Mostafa, J. De Baerdemaeker, N. Van Caenegem Y. Houbaert, and D. Segers. *Journal of Materials Engineering and Performance* (accepted)

7. Effect of annealing on deformed Iron, K. M. Mostafa, J. De Baerdemaeker, C. A. Palacio, E. De grave, D. Segers, and Y. Houbaert (ready to be *submitted*)

8. Positron implantation and transmission experiments on free-standing nanometric polymer films, C. A. Palacio, J. De Baerdemaeker, D. Segers, K. M.

Mostafa, D. Van Thourhout and C. Dauwe. J. *Materials Science Forum.607* (2009) p.105.

9. Parameterization of the median penetration depth of implanted positrons in free-standing polymer films, C. A. Palacio, J. De Baerdemaeker, M. H. Weber, D. Segers, K. G. Lynn, K. M. Mostafa and C. Dauwe. *(Ready to be submitted*)

10. Probing the molecular level of polyimide-based solvent resistant nanofiltration membranes with positron annihilation spectroscopy. Angels Cano-Odena, Pieter Vandezande, Katrien Hendrix, Rolph Zaman, Khaled Mostafa, Werner Egger, Peter Sperr, Jérémie De Baerdemaeker, Ivo Vankelecom, *The Journal of Physical Chemistry* (under review)